



Jade Nassif

Multi-objective Multi-point Aerodynamic Optimisation of a  
Hypersonic Waverider

SCHOOL OF AEROSPACE, TRANSPORT AND  
MANUFACTURING  
Aerospace Computational Engineering

MSc  
Academic Year: 2023 - 2024

Academic Supervisor: Dr Tamás István Józsa  
External Supervisor at Destinus: Dr Jimmy-John Hoste  
27/08/2024



SCHOOL OF AEROSPACE, TRANSPORT AND  
MANUFACTURING  
Aerospace Computational Engineering

MSc

Academic Year: 2023 - 2024

Jade Nassif

Multi-objective Multi-point Aerodynamic Optimisation of a  
Hypersonic Waverider

Academic Supervisor: Dr Tamás István Józsa  
External Supervisor at Destinus: Dr Jimmy-John Hoste  
27/08/2024

This thesis is submitted in partial fulfilment of the requirements  
for the degree of MSc

© Cranfield University 2024. All rights reserved. No part of this  
publication may be reproduced without the written permission of  
the copyright owner.

## **Academic Integrity Declaration**

The author declares that:

- the thesis submitted has been written by them alone.
- the thesis submitted has not been previously submitted to this university or any other.
- all content, including primary and/or secondary data, is true to the best of their knowledge.
- all quotations and references have been duly acknowledged according to the requirements of academic research.

The author understands that to knowingly submit work in violation of the above statement will be considered by examiners as academic misconduct.

# Abstract

Hypersonic flight, defined by speeds above Mach 5, has the potential to revolutionize the commercial aviation sector. Waveriders, which make use of an attached shockwave to produce lift, are a promising type of hypersonic vehicle. However, waverider design presents significant challenges, including severe aerodynamic heating, wide-speed performance loss, wave drag, and stability issues. Moreover, these problems have rarely been tackled together within a well-defined optimisation framework. Here, an existing optimisation methodology is extended to include additional aspects of waverider design. A design space is established using osculating cone theory, with optimisation performed via a surrogate model, a genetic algorithm, and inviscid CFD simulations for performance estimation. A design space analysis showed that the design Mach number is the most influential factor on lift, drag, and lift-to-drag ratio, while  $X_2$ , controlling shockwave curvature, is the main factor for internal volume. Single-objective test cases showed that maximizing volume and drag are equivalent objectives ; and minimizing volume, drag, and lift are also equivalent. Unexpectedly, maximizing lift revealed a unique optimum, despite its increasing relationship with volume. Furthermore, the test cases confirmed the accuracy and reliability of the surrogate model. Multi-objective cases involving volume and drag reached a Pareto Front with two linear sections: one favoring flat shockwave designs at  $M_{\text{design}} = 5$ , and another with maximum volume designs (maximum curvature, flat upper surface) as the design Mach number increases. A similar trend was observed in lift-drag optimisation, but with different solutions in the second section. These cases revealed that introducing the design Mach number reduces the diversity of optimal shapes, which is its major drawback. Finally, a post-optimisation longitudinal analysis showed that volume is a driving parameter in determining longitudinal characteristics of waveriders. Specifically, higher-volume waveriders are less affected by changes in angle of attack in terms of performance loss and changes in centre of pressure ; but this is at the expense of smaller stability margins. Placing the CG at the center of mass results in all waverider configurations being longitudinally statically unstable. The approach used here lays the foundation for a more global waverider shape optimisation framework while also suggesting future improvements. For instance, accounting for viscous effects in the optimisation process is key in enhancing the reliability of the optima reached.

## Acknowledgements

Calling this an individual work would be misleading, to say the least. Just like anyone, I am the product of my own environment. I have many people to thank for my successes in life and, for what I hope you will find is, an interesting and high quality thesis.

I would like to start by thanking my parents - without whom I would not be where I am today. You have always encouraged me to pursue my aspirations and supported me every step of the way. As I conclude this chapter of my life, I understand, more than ever, the immense sacrifices you have made in raising me and my sisters. I extend a similar feeling of gratitude to my sisters, I love you all very very much and am forever grateful to you.

Moreover, I would like to thank Hania, my partner and the love of my life. You have been by my side through my highs and lows, successes and failures. We have been through so much together already, and I'm very excited to see what the future has in store for us. You mean the world to me and I learn more and more from you every day. I love you very very much.

From a more academic point of view, I would like to acknowledge the support of Dr Tamás Józsa. Your invaluable advice and guidance have allowed me to push this thesis as far as possible in these three very short months. In a similar light, I would like to extend my gratitude to Dr Jimmy-John Hoste at Destinus. Your useful suggestions and deep knowledge of the literature have influenced much of my approach and findings. I hope to leave you both with a lot of interesting future work to be investigated in the years to come!

Finally, I would like to conclude by thanking Swapnil, Luca, Amey and Aakalpa - my friends and colleagues here at the university. You have made my experience at Cranfield an exciting one and I very much enjoyed working with you on project Airboyz. More generally, it has been a pleasure to get to know you all and discuss our shared interests. I look forward to graduating with you all in June of next year.

## Artificial Intelligence

This thesis was produced with the help of ChatGPT 4o. In particular, the tool was used to enhance the readability of the text and provide occasional help with debugging code.

# Contents

<b>Contents</b>	<b>6</b>
<b>List of Figures</b>	<b>8</b>
<b>List of Tables</b>	<b>9</b>
<b>1 Introduction</b>	<b>12</b>
1.1 Motivation . . . . .	12
1.2 Industrial Collaboration . . . . .	13
1.3 Literature Review . . . . .	13
1.3.1 Waveriders in the Literature vs Real Life . . . . .	13
1.3.2 Waverider Inverse Design Methods . . . . .	14
1.3.2.1 Two-dimensional Flow Fields . . . . .	15
1.3.2.2 Three-dimensional Flow Fields . . . . .	15
1.3.3 Problems of the Hypersonic Regime . . . . .	17
1.3.3.1 Heating . . . . .	17
1.3.3.2 Wide-speed Problem . . . . .	17
1.3.3.3 Stability & Control . . . . .	18
1.3.4 Performance Estimation via CFD . . . . .	19
1.3.5 Aerodynamic Shape Optimisation . . . . .	19
1.3.6 Knowledge Gap . . . . .	20
1.4 Aim and Objectives . . . . .	21
<b>2 Methodology</b>	<b>22</b>
2.1 Overall Approach . . . . .	22
2.2 Waverider Terminology . . . . .	22
2.3 Waverider Parametrisation . . . . .	23
2.3.1 Base Plane Parametrisation . . . . .	23
2.3.2 Osculating Cone Theory . . . . .	24
2.3.3 Waverider Generator . . . . .	26
2.3.4 Design Space Inputs . . . . .	27
2.3.4.1 Design Mach Number & Shockwave Considerations . . . . .	28
2.3.5 Design Space Dynamics . . . . .	30
2.3.6 Design Space Outputs . . . . .	31
2.4 Performance Estimation - Inviscid Flow . . . . .	32
2.4.1 Domain and Mesh . . . . .	32
2.4.2 Adaptive Mesh Refinement . . . . .	36
2.4.3 Numerical Solver Configuration . . . . .	38
2.4.3.1 Real Gas . . . . .	38
2.4.3.2 Coupled Implicit Solver . . . . .	38
2.4.3.3 Spatial Discretisation . . . . .	38
2.4.3.4 Initialisation . . . . .	39
2.4.4 Convergence . . . . .	39
2.4.5 Flow Conditions . . . . .	39
2.4.6 Grid Convergence Study . . . . .	40
2.4.7 Schlieren Imaging . . . . .	41

2.4.8	High Performance Computing . . . . .	41
2.5	Surrogate Modelling . . . . .	41
2.5.1	Sampling . . . . .	41
2.5.2	Kriging Surrogate Model . . . . .	43
2.6	Shape Optimisation . . . . .	46
2.6.1	Genetic Algorithm . . . . .	46
2.6.1.1	Overall Setup . . . . .	46
2.6.1.2	Constraint Evaluation . . . . .	47
2.6.2	Test Cases . . . . .	48
2.6.3	Multi-objective Optimisation Cases . . . . .	48
2.6.3.1	Case 1 . . . . .	49
2.6.3.2	Case 2 . . . . .	49
2.6.3.3	Case 3 . . . . .	49
2.6.3.4	Case 4 . . . . .	50
2.6.3.5	Case 5 . . . . .	50
<b>3</b>	<b>Results &amp; Discussions</b>	<b>51</b>
3.1	CFD Verification . . . . .	51
3.2	Design Space Analysis . . . . .	54
3.2.1	Main Trends . . . . .	54
3.2.2	Feature Importances . . . . .	56
3.3	Shape Optimisation . . . . .	59
3.3.1	Test Cases . . . . .	59
3.3.2	Multi-objective Cases . . . . .	63
3.3.2.1	Results from Cases 1 & 4 . . . . .	63
3.3.2.2	Results from Case 2 . . . . .	67
3.3.2.3	Results from Case 3 . . . . .	68
3.3.2.4	Results from Case 5 . . . . .	70
3.4	Longitudinal Analysis . . . . .	73
<b>4</b>	<b>Conclusions</b>	<b>79</b>
<b>5</b>	<b>Future Work</b>	<b>81</b>
<b>Appendix A : Pareto Fronts</b>		<b>82</b>
<b>Appendix B : Sample Points</b>		<b>84</b>
<b>Appendix C : Waverider Generator Example</b>		<b>87</b>
<b>Appendix D : CURES Approval Letter</b>		<b>88</b>
<b>References</b>		<b>89</b>

# List of Figures

1	Küchemann's [1] $L/D$ barrier . . . . .	12
2	Boeing X-51 Waverider (a) and HTV-2 (b) during flight . . . . .	14
3	Graphical representation of the wedge derived waverider (a) and the cone derived waverider (b) . . . . .	15
4	Graphical representation of the osculating cone method . . . . .	16
5	Waverider terminology and coordinate system in this study . . . . .	22
6	Parametrisation of the Base Plane . . . . .	23
7	Representation of a waverider with an osculating plane . . . . .	25
8	Inputs/Output of Waverider Generator [85] . . . . .	26
9	Example of 9 configurations obtained through Waverider Generator . . . . .	27
10	Shock angle at symmetry plane against $M_{\text{design}}$ . . . . .	28
11	Effect of $M_{\text{design}}$ on the lower surface of the waverider . . . . .	29
12	Geometric constraint curve . . . . .	30
13	Inviscid domain $\Omega \in \mathbb{R}^3$ used in this study . . . . .	33
14	Views of a typical mesh without AMR . . . . .	35
15	Views of the mesh after three sets of AMR . . . . .	37
16	Slices of the design space showing the sample points . . . . .	43
17	Cross-validation of the surrogate models on the testing data . . . . .	45
18	Pressure coefficient contours in on and off design conditions for two waveriders . . . . .	52
19	CFD Shockwave shape compared to analytical shockwave shape in design conditions via Schlieren imaging . . . . .	53
20	Main trends identified from the outputs of the design space . . . . .	55
21	Feature Importances . . . . .	58
22	Outputs plotted against their most important feature . . . . .	59
23	The three optimal waveriders reached in the test cases . . . . .	62
24	Representative Pareto Front for Case 1 . . . . .	63
25	Variation of $M_{\text{design}}$ (a), $(L/D)_{M5}$ (b) and $v_{\text{eff}}$ (c) across the Case 1 Pareto Front . . . . .	64
26	Variation of $X_1$ and $X_2$ across the Case 1 Pareto Front . . . . .	65
27	Pareto Front from Son <i>et al.</i> [16] . . . . .	66
28	Representative Pareto Front for Case 4 . . . . .	67
29	Full Pareto Front for Case 2 (a) and $D_{M5}$ against $v_{\text{eff}}$ across the sample points (b) . . . . .	68
30	Representative Pareto Front for Case 3 . . . . .	69
31	Viscous drag estimates along the Case 3 Pareto Front . . . . .	70
32	Representative Pareto Front for Case 5 . . . . .	71
33	Variation of $M_{\text{design}}$ (a) and $X_1$ - $X_2$ (b) across the Case 5 Pareto Front . . . . .	72
34	Pressure coefficient contours are three angles of attack on a waverider in M5 flow . . . . .	74
35	$x_{CP}$ (a), $C_M$ (b), Lift (c) and Drag (d) against angle of attack . . . . .	77
36	Full Pareto Front for Case 1 . . . . .	82
37	Full Pareto Front for Case 3 . . . . .	82
38	Full Pareto Front for Case 4 . . . . .	83
39	Full Pareto Front for Case 5 . . . . .	83
40	CURES Approval Letter . . . . .	88

## List of Tables

1	Nomenclature of mathematical symbols . . . . .	10
2	List of Abbreviations . . . . .	11
3	Values of the design variables in Figure 9 . . . . .	27
4	Outputs of the design space . . . . .	31
5	Boundary conditions applied . . . . .	33
6	Mesh settings . . . . .	34
7	Flow conditions . . . . .	40
8	Grid convergence study at the M5 flow condition . . . . .	40
9	Grid convergence study at the M8 flow condition . . . . .	40
10	Reference values . . . . .	46
11	Main parameters of the GA setup for both Test and Multi-objective cases . . . . .	47
12	Test cases considered . . . . .	48
13	Description of the Multi-objective Cases . . . . .	49
14	Waveriders used for verification purposes . . . . .	51
15	Maximum and minimum values of volume for three design mach numbers . . . . .	57
16	Results of the test cases . . . . .	60
17	Wetted surface area of three waveriders with varying $M_{\text{design}}$ . . . . .	66
18	Lift and $L/D$ characteristics of the nine waveriders at the three angles considered . . . . .	75

# Nomenclature

## Symbols

Table 1: Nomenclature of mathematical symbols

Quantity	Description	Units
$L$	Lift force	N
$D$	Drag force	N
$L/D$	Lift to drag ratio	[ $-$ ]
$M_\infty$	Freestream Mach number	[ $-$ ]
$p$	Static pressure	Pa
$p_\infty$	Freestream static pressure	Pa
$T$	Static temperature	K
$T_\infty$	Freestream static temperature	K
$\rho$	Air density	$\text{kg} \cdot \text{m}^{-3}$
$\rho_\infty$	Freestream air density	$\text{kg} \cdot \text{m}^{-3}$
$\mathbf{u} = [u, v, w]$	Velocity vector	$\text{m} \cdot \text{s}^{-1}$
$U_\infty$	Freestream velocity	$\text{m} \cdot \text{s}^{-1}$
$\mathbf{n} = [n_x, n_y, n_z]$	Unit vector normal to a boundary	[ $-$ ]
$\nabla$	Differential operator	$\text{m}^{-1}$
$\alpha$	Angle of attack	deg
$\beta$	Shock angle	deg
$\theta$	Deflection angle	deg
$M_{\text{design}}$	Design Mach number	[ $-$ ]
$\Delta\beta$	Change in shock angle at symmetry plane	deg
$h$	Shockwave height at base plane	m
$w$	Half-width of the waverider	m
$l$	Length of the waverider	m
X1,X2,X3,X4	Geometric design parameters	[ $-$ ]
$v_{\text{eff}}$	Volumetric efficiency	[ $-$ ]
$V$	Internal volume of the waverider	$\text{m}^3$
$S_{\text{wet}}$	Wetted surface area (not including back)	$\text{m}^2$
$x_{\text{CP}}$	Center of pressure position in the $x$ direction	m
$C_p$	Pressure coefficient	[ $-$ ]
$C_M$	Pitching moment coefficient	[ $-$ ]
$n_{\text{ref}}$	Number of adaptive mesh refinements	[ $-$ ]

## Abbreviations

Table 2: List of Abbreviations

Abbreviation	Description
M5	M5 Flow condition (Mach 5, 25 km altitude)
M8	M8 Flow condition (Mach 8, 30 km altitude)
LEC	Leading Edge Curve
USC	Upper Surface Curve
SC	Shockwave Curve
LSC	Lower Surface Curve
CFD	Computational Fluid Dynamics
HPC	High-Performance Computing
MDO	Multi-Disciplinary Optimization
GA	Genetic Algorithm
HGV	Hypersonic Glide Vehicle
AMR	Adaptive Mesh Refinement
RANS	Reynolds-Averaged Navier-Stokes
SST	Shear Stress Transport
OP	Osculating Plane
TPS	Thermal Protection System
HTV-2	Hypersonic Technology Vehicle 2
X-51	Boeing X-51 Waverider
NASA	National Aeronautics and Space Administration
CAD	Computer-Aided Design

# 1 Introduction

Hypersonic flight, defined by velocities above Mach 5, comes with a plethora of problems [1]. From sustaining propulsion to handling the extreme temperatures of the regime, considerable efforts are needed to master hypersonic flight. However, it also has the potential to revolutionise commercial aviation by dramatically reducing travel times. Moreover, the ongoing research into clean aviation further justifies efforts to make hypersonic commercial aircraft a reality in the sector, and possibly replace transonic aircraft [2, 3, 4].

## 1.1 Motivation

The aviation industry represents 12% of all CO<sub>2</sub> emissions originating from transportation [5, p. 2]. This highlights the important carbon footprint of the sector, and the need for manufacturers to develop more environmentally friendly aircraft. As a consequence, modern aircraft are designed around minimising fuel consumption and operate in the transonic regime - as supersonic and hypersonic flight are deemed unsustainable and result in a multitude of other challenges. However, the ongoing research into hydrogen fuel is promising [6] and, if successfully integrated in commercial aircraft, would result in clean aviation. This would make hypersonic aircraft the logical next step in air transportation.

Nevertheless, even in hypersonic flight, minimising fuel consumption remains an important objective as it minimises cost and promotes sustainability. In terms of forces acting on the aircraft, this translates into minimising drag - which is the “aerodynamic force that opposes an aircraft’s motion through the air” [7]. At subsonic speeds, viscous effects contribute to most of the drag while pressure effects are often considered negligible [8]. However, the switch from subsonic to supersonic flow leads to a new form of pressure drag, known as wave drag [9]. Wave drag arises from the generation of shockwaves, which are inherent to the supersonic domain.

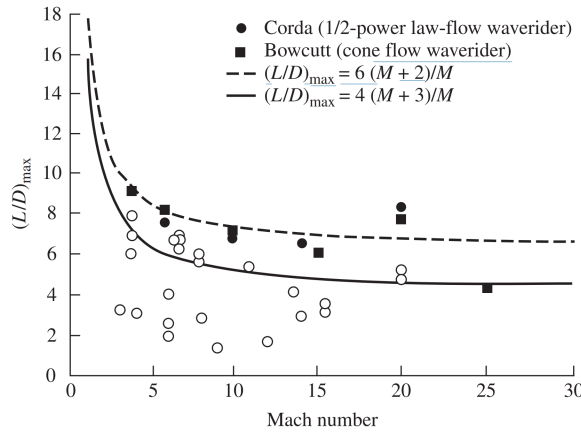


Figure 1: Kückemann’s [1]  $L/D$  barrier (taken from [10])

The concept of a waverider, first proposed by Nonweiler in 1959 [11], has emerged as a promising type of vehicle for hypersonic flight as it is capable of breaking the lift-to-drag ratio ( $L/D$ ) barrier previously established by Kückemann [12], as shown in Figure 1 above. Moreover, studies have shown that, for a same lift coefficient, waverider geometries have a higher  $L/D$  than “traditional” configurations ([13], [14, p. 111-146, 183–257, 375–

395, 415–445]). A higher lift to drag ratio in cruise condition results in a higher range, as predicted by the Breguet Range Equation. It is therefore a crucial parameter in measuring the performance of an aircraft.

The defining feature of a waverider is a shockwave attached along its leading edge [15]. This causes the high pressure flow below the lower surface, known as the compression surface, to generate compression lift. On the other hand, the upper surface is referred to as the freestream surface due to the flow around it remaining unaffected. For this reason, the design must also minimise “spillage” of the flow from the compression surface to the freestream surface, as this would result in a “waste” of lift.

Due to these characteristics, waveriders are commonly constructed for a specific flow field [15, p. 1]. In other words, the waverider geometry is determined using the flow field of a specific Mach number and shockwave shape, which guarantees that the resulting geometry has an attached shockwave and minimal flow spillage to the upper surface at this Mach number. Despite its popularity in waverider design [16, p. 2], this inverse design approach introduced by Nonweiler [11] has several limitations. For example, since the waverider is crafted for a design Mach number, there is no guarantee is that its performance or defining characteristics (see previous paragraph) are maintained in off-design conditions. Moreover, the desired performance is itself not guaranteed at the design conditions as there is no way to evaluate it as part of the methodology [16]. As a consequence, design constraints such as internal volume or  $L/D$  cannot be applied at any point in the approach, preventing shape optimisation from being conducted [16]. Thus, advancing the waverider shape optimisation methodology is crucial in obtaining geometries which match design requirements and therefore promote sustainable aviation.

## 1.2 Industrial Collaboration

This project was carried out in cooperation with Destinus, a start-up with the aim of revolutionising air transportation. More specifically, Destinus wishes to build the first hypersonic commercial airplane by 2030. Their hypersonic airplane concept is, at its core, a waverider.

As such, this project and its outcomes are relevant to their efforts in advancing waveriders into commercial aviation.

## 1.3 Literature Review

### 1.3.1 Waveriders in the Literature vs Real Life

By definition, a waverider is a hypersonic vehicle which makes use of its own shockwave to produce lift [15]. However, one can distinguish between two types of waveriders.

Indeed, a waverider can refer to a Hypersonic Glide Vehicle (HGV). These are unpowered vehicles which are typically launched via a rocket and then proceed to glide at hypersonic velocities until they reach their target [17]. Examples of such HGVs include the HTV-2 [18] and Avangard [19]. In such cases, a waverider denotes a complete hypersonic vehicle.

On the other hand, a waverider can also refer to the forebody of a complete hypersonic vehicle. In such cases, the vehicle is powered by an engine (e.g a scramjet) located behind the waverider forebody [17],[20, p. 2]. This allows hypersonic flight to be sustained in

a cruising condition for longer periods of time. The waverider is therefore designed for a specific shockwave shape where the engine inlet would be located. Examples of air-breathing powered waveriders include the NASA X-43 [21] and the Boeing X-51 Waverider [19].

Depictions of the HTV-2 and X-51 are shown in Figure 2.

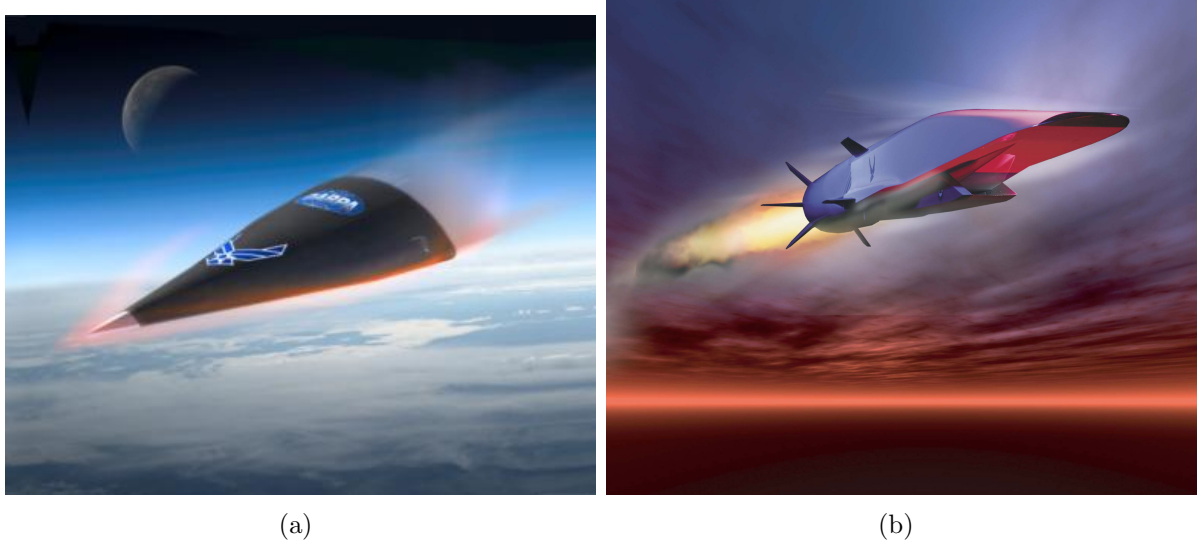


Figure 2: Artists' depiction of the Boeing X-51 Waverider (a) and HTV-2 (b) during flight. Taken from [22] and [23].

In this thesis, some concepts may be more pertinent to HGVs, while others may hold more importance for the design of a waverider forebody. For instance, considering the influence of operating conditions on shockwave shape aligns more closely with the integration of an engine inlet. On the other hand, investigating longitudinal stability is more in line with the design of HGVs, which are complete vehicles in and of themselves.

### 1.3.2 Waverider Inverse Design Methods

Since 1959, when Nonweiler presented his pioneering waverider idea [11], a large number of design methodologies have emerged for the generation of waverider geometries. Regardless of the method employed, the overall process remains the same [24].

First, a basic flow field representing the flow around the waverider is chosen and solved. Given compressible effects dominate at supersonic and hypersonic speeds (refer to Section 1.1), the basic flow fields used to shape waveriders are typically steady and inviscid [24, p. 1]. This step establishes the shape of the shockwave and the properties of the flow such as the Mach number or shock angle.

The next step involves generating the leading edge and freestream surface [16, p. 2]. Since the shockwave needs to remain attached along the leading edge, the leading edge is generated by finding where the freestream flow intersects with the shockwave. The upper surface is then generated as the “surface generated by moving the leading-edge shape parallel to the freestream direction” [16, p. 2], thereby ensuring its freestream property. Finally, a streamline tracing technique is implemented to construct the compression surface. The streamlines are traced at discrete points along the leading edge and lofted

together to produce the compression surface [25, p. 5].

### 1.3.2.1 Two-dimensional Flow Fields

The first category of basic flow fields is characterised by its two-dimensionality (2D). The initial waverider concept proposed by Nonweiler [11] was derived by considering the flow past a wedge, which is a kind of planar two-dimensional flow. As shown in Figure 3a, these have come to be known as “wedge-derived”, “caret” or “ $\Lambda$ ” waveriders due to their inverted V shape [24]. Still within the planar flow field approach, the V-shaped configuration was considered by Zubin and Ostabenko ([26, 27]). Furthermore, experimental work conducted by Ostabenko [28] shows its superiority in terms of  $L/D$  compared to an equivalent conventional wing. Mazhul and Rakhcimov [29] generated another type of wedge-derived waverider, this time by making use of a power-law to generate the compression surface.

Another common kind of 2D flow field is the flow around a cone with zero incidence, appropriately termed conical flow field [24]. This type of flow field, depicted in Figure 3b, is axisymmetric in nature and waveriders generated via this method are known as cone-derived. The first instance of the cone-derived waverider is by Jones *et al.* [30]. Further research into cone-derived waveriders was conducted by Bowcutt *et al.* [31], who showed that viscous optimised cone-derived waveriders break the  $L/D$  barrier established by Küchemann [12].

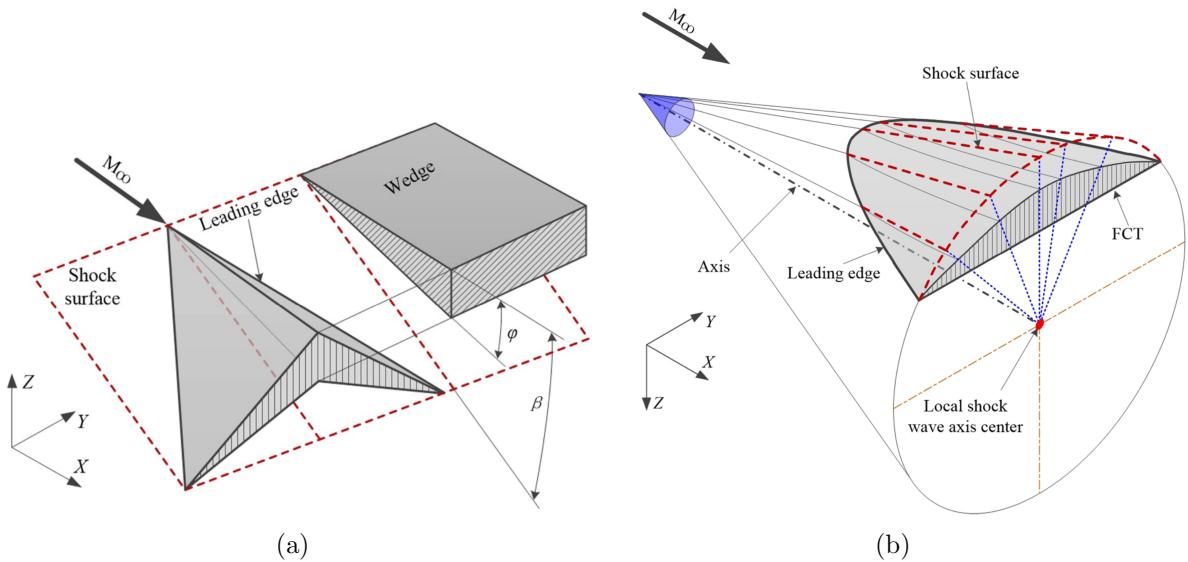


Figure 3: Graphical representation of the wedge derived waverider (a) and the cone derived waverider (b), taken from [20].  $\varphi$  is the deflection angle and  $\beta$  is the shock angle.

### 1.3.2.2 Three-dimensional Flow Fields

The second category of basic flow fields is characterised by its three-dimensionality. Rasmussen [32] and Rasmussen and Maurice [33] considered the flow around quasi-cones, resulting in the first of its kind 3D flow field. Further work on this type of flow field was carried out by Rasmussen *et al.* [34], Lin and Luo [35] and Cui and Yang

[36]. Results generally show that geometries obtained via this flow field yield a higher  $L/D$  than an equivalent cone derived waverider.

In contrast, Takashima and Lewis [37] derived waveriders through a wedge-cone flow field. In comparison to cone-derived waveriders, wedge-cone configurations can match their  $L/D$  while also allowing for a higher internal volume.

Despite the progress observed through the development of these flow fields, they do not provide much control of the waverider geometry in the spanwise direction. To address this issue, flow fields based on the osculating cone theory, by Sobieczky *et al.* [38], became the next step in waverider design - where the 3D flow around a waverider is represented by a set of local spanwise conical flows, also known as osculating cones. The streamlines are then traced for each osculating cone independently [24, p. 9] but since the flow properties inside each cone remain the same (shock angle and Mach number), the flow field must only be solved once. The use of this method has led to major improvements in extending the design space available to waverider designers while maintaining a low computational cost. It is depicted in Figure 4.

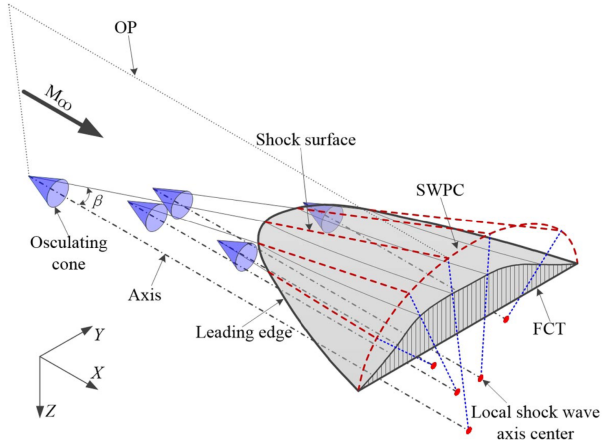


Figure 4: Graphical representation of the osculating cone method, taken from [20]

The osculating cone has been extended by Rodi [39] into the osculating flow field such that the different osculating planes are no longer restricted to a common conical flow field. Rather, a different conical flow can be applied in each plane and this results in a combination of local flow fields. This method was formulated in an effort to satisfy specific design constraints and make the waverider perform better across a wide-speed range ([24, p. 9], [25, p.4])

Waveriders obtained via osculating design methods have been shown to improve the uniformity of the flow field at the engine inlet compared to cone-derived waveriders [24, p. 9]. This makes them more suitable for the integration of an engine located behind the waverider such as a scramjet. Moreover, research has shown an increase in the  $L/D$  reached by these methods as opposed to cone derive waveriders [40]. However, a drawback of such methods is the underlying assumption that the azimuthal pressure gradients are negligible [20]. It has been shown by Chauffour and Lewis that this is not always true [41].

### 1.3.3 Problems of the Hypersonic Regime

#### 1.3.3.1 Heating

Aerodynamic heating is a major problem experienced by hypersonic waveriders [42]. The air compression caused by the shockwave leads to an extreme rise in temperature around the leading edge and on the lower surface, with a peak temperature experienced at the tip of the waverider [10, 42]. In extreme cases, this could lead to the melting of the material [43] and malfunctioning of sensors and other on-board systems. The Hypersonic Technology Vehicle 2 (HTV-2) is an example of a glide vehicle which failed due to heat stresses at Mach 20 [44]. Many solutions for a Thermal Protection System (TPS) have been proposed. For example, Engblom and Goldstein [43] showed that adding a cavity at the nose of a body in hypersonic flow reduces peak heating. However, this solution also adds unsteadiness to the flow [45]. Further studies on this type of TPS have been conducted in recent years [46, 47]. An alternative is to include a spike at the nose of the vehicle [48, 49]. This configuration aims to divert the flow from the body, shielding it from extreme temperature rises [48]. Despite its simplicity, this solution tends to cause oscillations in the flow which can disrupt the vehicle in flight [48]. More recently, efforts to study the effects of a counter-flowing jet at the nose have been made [50, 42] and revealed that this concept can tackle some of the problems of the previously mentioned TPS.

In the context of idealised waveriders produced using inverse design methods and lacking a TPS, a common way to indirectly tackle the aerodynamic heating problem is to maximise internal volume [16]. Indeed, the rationale is that maximising internal volume leads to more space to include a TPS and other internal components. This has led to internal volume being considered as an objective in some optimisation studies [51, 16]. Another quantity of interest is the volumetric efficiency [52, 53], defined as:

$$v_{\text{eff}} = V^{2/3}/S_{\text{wet}} \quad (1)$$

Where  $V$  is the internal volume of the waverider and  $S_{\text{wet}}$  is the total wetted area of the vehicle, not including its back surface.

The volumetric efficiency can capture how much usable volume a particular configuration provides. For this reason, it is important to maximise it for both heating and storage purposes.

#### 1.3.3.2 Wide-speed Problem

The wide speed problem arises due to the fact that waveriders are designed for a specific Mach number and shockwave shape. For this reason, when the waverider is operated in off-design conditions, a loss in performance can be observed. This can be quantified in many ways. For example, flow spillage to the upper surface can take place. Moreover, the resulting shockwave shape is not the design shockwave shape, and this can impact the performance of an engine located aft of the waverider. Other metrics such as lift, drag and  $L/D$  can also vary across the speed-range.

In an attempt to tackle this problem, the “combined” waverider concept was introduced. The idea behind it is to stitch together waveriders designed for certain conditions so that the performance of the overall vehicle is better in the speed range than the original configurations’ [25]. For instance, Wang *et al.* [54] combined, via a connecting segment,

a waverider designed for Mach 3 with one designed for Mach 6. The results showed that a reasonably good lift to drag ratio is maintained across the speed range [54, p. 5]. Still within the “combined” category, the “parallel” waverider was tested by Li *et al.* [55]. Here, the leading edges and trailing edges of two waveriders are assembled [55]. The results show an increase in  $L/D$  over the speed range considered [55, p. 6].

Another approach was taken by Liu *et al.* [56], who made use of the osculating flowfield [39] by varying the design Mach number in the spanwise direction i.e in each osculating plane [56, p. 2]. The main advantage of such an arrangement is that little to no overflow is present over the speed range (Mach 6 to Mach 13) [56, p. 6].

Finally, the speed range considered can also include subsonic to transonic speeds. In such cases, the waverider must be designed to operate from these regimes all the way to the hypersonic regime. This prompted the invention of the “vortex lift” waverider [57], which is designed to make use of vortical structures near the leading edge, which are prominent at subsonic and transonic speeds, to promote lift in these regimes. At the same time, the waverider should be able to maintain a good performance in the hypersonic regime as well. Numerous attempts at designing such waveriders have been made [57, 58, 59].

### 1.3.3.3 Stability & Control

A system is said to be stable “if after a disturbance of finite amplitude and duration the response ultimately becomes vanishingly small” [60, p. 224]. One can distinguish between two types of stability: static and dynamic [60]. The former refers to the aircraft’s ability to return to its initial equilibrium state after it suffers a disturbance [60, p. 225]. The latter is more concerned with the actual transient response leading to a return to equilibrium [60, p. 225].

The stability of waveriders has been investigated in numerous different ways. Bykerk *et al.* [61, 62, 63, 64] focused on investigating low-speed stability. The studies made use of experimental wind tunnel results along with CFD simulations. In terms of static stability, the findings indicate that longitudinal stability was observed up to a 22 degree angle of attack, beyond which point vortical structures lead to instability. Lateral directional static stability displayed similar results with the vortices and position of the center of gravity playing an important role. Moreover, control surfaces known as elevons were tested in their ability to provide control over pitching and rolling moments, and were found successful in trimming the waverider in various flight conditions. Bykerk *et al.* also explored dynamic stability via URANS simulations, with the aim of capturing the unsteady effects of the flow. They found that the aircraft could recover from disturbances in pitch, although this damping reduced at higher angles of attack due to the aforementioned vortical interactions.

Taking another approach, Liu et al. [65] researched the lateral-directional stability of hypersonic waveriders via a combination of wind tunnel testing, CFD simulations, and surrogate modeling. The work focused on how parametric design variables like dihedral angle and leading-edge sweep affected stability. The findings showed that an increase in dihedral angle is desirable and stability-based shape optimisation improved both static and dynamic stability.

Finally, Tarpley and Lewis [66] derived analytical formulae for the calculation of static stability derivatives for Caret waveriders. The method makes use of linear piston theory

to approximate the pressure forces acting on the waverider. The results indicate that linear piston theory is able to provide reasonably accurate estimates of stability derivatives compared to experimental work [66]. More specifically regarding longitudinal static stability, the stability derivatives indicate instability when the centre of gravity is coincident with the center of mass/volume (i.e assuming a uniform mass distribution) [66].

#### 1.3.4 Performance Estimation via CFD

As mentioned in Section 1.1, the inverse design methodology adopted does not guarantee that the performance requirements are met following the creation of the waverider [16]. For this reason, high fidelity Computational Fluid Dynamics (CFD) solvers are required to estimate key performance metrics such as  $L/D$ , lift, drag and pitching moment coefficient.

To obtain a first realistic estimation of the performance, CFD analyses are most often conducted in steady 3D inviscid flow, which translates to solving the steady 3D Euler equations. This is mainly because viscous effects are considered negligible at hypersonic speeds and so accounting for them adds unnecessary computational cost in the early stages [67, 68] - especially if the objective is to modify the shape of waverider until the required performance is met. However, it is common to then perform a viscous simulation, solving the steady Reynolds Averaged Navier Stokes (RANS) equations, to estimate the viscous contributions and compare the final performance to the one obtained via inviscid flow, as was done in [67, 68, 69, 70, 71]. Within the viscous setup, The  $k - \omega$  [71] and  $k - \omega$  SST [67, 68, 69, 70] turbulence models are the most commonly employed. Furthermore, freestream boundary conditions are applied on the domain and zero tangential velocity adiabatic boundary conditions are applied on the waverider's walls. Additionally, a symmetry boundary condition can be applied on the waverider's symmetry plane, therefore resulting in only half the geometry being simulated and further reducing computational cost [67, 68, 69, 70, 71].

In terms of grid generation, both structured [72, 73] and unstructured meshes [67, 68, 69, 70, 71] have been used. Regardless of which is employed, extra measures are needed in viscous flow to ensure the viscous effects near the wall are well captured. Specifically, a  $y^+$  value of 1 (or less) is required near the walls [69, 70, 72, 73].  $y^+$  is a dimensionless number representing the distance to the wall from the nearest grid cell, and so  $y^+ \leq 1$  ensures the viscous sub-layer is captured accurately [74].

#### 1.3.5 Aerodynamic Shape Optimisation

Aerodynamic Shape Optimisation consists in optimising the shape of a lifting body with regards to one or more aerodynamic design requirements and eventual design constraints. For example, a wing can be optimised to minimise drag at a fixed lift coefficient. This can be achieved by coupling an optimisation algorithm, an appropriate flow solver and a parametrisation of the geometry [75].

One can distinguish between two types of optimisation algorithms. The first, known as gradient-based algorithms, make use of the local gradient of the cost function with respect to the design variables [76]. The information of the gradient guides the algorithm towards an optimum. However, there is no guarantee that the solution obtained is the global optimum - especially with a large number of design variables, which tends to result in a highly multi-modal design space [76, p. 2]. Gradient-based methods run the risk

of getting stuck in a local optimum, depending on the algorithm's starting point [76, p. 6]. Gradients can be estimated through finite difference methods but this approach becomes more computationally expensive with more design variables. However, this can be overcome through the adjoint-based method which involves solving an adjoint equation to obtain all gradients at once [77]. For this reason, adjoint optimisation is a popular method in aerodynamic shape optimisation as it is independent of the number of design variables and therefore allows for direct control of the shape through its mesh surface points. Adjoint-based optimisation has been investigated in the waverider literature by Vizcaino [70] and Felix [69] who considered maximising the  $L/D$  of a cone-derived waverider. The results showed an increase in the ratio but generally at the expense of lift and internal volume. Adjoint optimisation was also performed by Qu *et al.* [58], this time with a multi-point cost function and a vortex-shock integrated waverider. Finally, a multi-disciplinary optimisation (MDO) approach was also taken by Morita *et al.* [78] using an adjoint-based optimiser, accounting for "Trajectory-Aero-Structure Coupling".

The second type of optimisation algorithms, known as search algorithms, aim to find the global optimum by direct search of the design space. These methods, unlike gradient-based optimisers, cannot directly account for constraints [75, p. 2]. Moreover, while these algorithms can offer a better chance of reaching the global optimum in higher-dimensional spaces, the associated computational cost for convergence tends to be high and so, in contrast with the adjoint method, manipulating every mesh point as a design variable is not feasible. As such, an efficient parametrisation with good design space coverage can reduce this cost and make search algorithms more practical in aerodynamic shape optimisation [75, 76] - at the expense of potentially not including the global optimum in said design space. Within the waverider literature, search-based algorithms have been considered in the past [79, 51, 80]. Of particular interest is the MDO of air breathing waveriders by Bowcutt [81], where the objective to maximise mission range while accounting for multi-disciplinary variables resulted in a 46% increase from the baseline. However, waverider optimisation has never been done through a well defined framework based on an inverse design method ; therefore, the work by Son *et al.* [16], where four efficient design variables from osculating cone theory were implemented into multi-objective optimisation, paves the way for a general optimisation framework for the aerodynamic shape optimisation of waveriders.

### 1.3.6 Knowledge Gap

While many of the problems of hypersonic waveriders have been considered in the literature, these have rarely been tackled together and even less so within a direct optimisation framework. As such, there is a need for an optimisation approach which can account for all (or some) of these problems simultaneously.

Furthermore, thus far, the optimisation of waveriders has lacked a clearly defined design space. For example, the adjoint solver, as integrated in commercial software like Star-CCM+ [82], provides detailed control over the vehicle's shape but, as a result, is very likely to get stuck in local optima and prevent a thorough exploration of the parameter space. Therefore, to overcome this, there is a need for an efficient parametrisation which can establish a broad design space, thereby improving the chances of reaching the global optimum. Only the work by Son *et al.* [16] has, thus far, clearly defined a valid design space in which to conduct optimisation based on an inverse design method.

Additionally, the waverider community lacks an open-source software for the generation of hypersonic waveriders, and this has restricted research in the field (for example, here at Cranfield University).

## 1.4 Aim and Objectives

The aim of this work is to outline and test a novel shape optimisation approach for hypersonic waveriders. In particular, the approach aims to tackle many of the problems of the hypersonic regime at once instead of individually.

To achieve this aim, the following objectives have been outlined:

1. Choosing an efficient parametrisation for the design of waveriders
2. Developing an open-source tool which can generate waveriders according to the parametrisation chosen
3. Define a design space for optimisation
4. Define optimisation objectives
5. Sample the design space and estimate performance through CFD
6. Build surrogate models
7. Choose an optimisation algorithm and perform optimisation
8. Perform a longitudinal analysis on competitive solutions

## 2 Methodology

### 2.1 Overall Approach

The methodology and approach in this thesis is inspired by the work of Son *et al.* [16], where a direct shape optimisation framework for hypersonic waveriders was presented. In summary, this takes the form of a surrogate-based multi-objective volume/drag shape optimisation approach. Here, the goal is to extend and improve this framework to consider further aspects of waverider design in the optimisation process. In particular, an emphasis is put on considering - at least in part - the wide-speed problem. To this end, the optimisation problems are formulated through multi-point cost functions which account for the following two realistic flight conditions:

1. Mach 5 at 25 km altitude (M5)
2. Mach 8 at 30 km altitude (M8)

For simplicity, these will be referred to as M5 and M8 hereafter.

Moreover, a post-optimisation longitudinal analysis of competitive waverider configurations is also included in this new approach.

Additionally, the original framework defined by Son *et al.* [16] lacked a thorough analysis of the design space as well as optimisation test cases to evaluate the performance of the surrogate models and optimisation setup. These are included in this thesis to ensure the results are more trustworthy and robust.

### 2.2 Waverider Terminology

For consistency across this report, this section introduces the waverider terminology used hereafter. Figure 5 shows a typical waverider configuration.

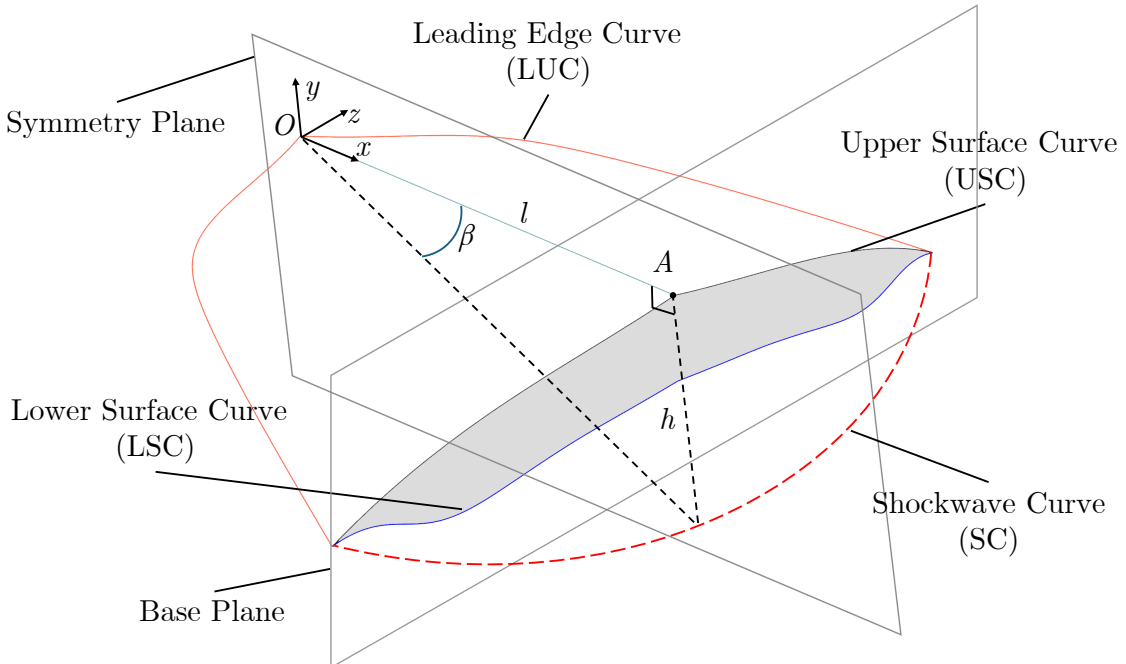


Figure 5: Waverider terminology and coordinate system in this study

As seen in Figure 5, the coordinate system originates at the tip of the waverider with  $x$  pointing along the length of the waverider,  $y$  pointing upwards and  $z$  pointing spanwise. The distance between the origin and point  $A$  represents the length  $l$  of the waverider.  $\beta$  is the shock angle and  $h$  is the height measured as the vertical distance between the SC and USC at the symmetry plane. Furthermore, the back of the waverider, shown in grey, is a flat surface normal to  $x$  and is located on the Base Plane.

## 2.3 Waverider Parametrisation

### 2.3.1 Base Plane Parametrisation

In this work, the parametrisation by Son *et al.* [16] is employed to parameterise the base plane of the waverider. The technique makes use of four geometric parameters to define the upper surface curve (USC) and the shockwave curve (SC) of the waverider. As will be shown in Section 2.3.3, this method consists of a small number of design variables while resulting in a wide variety of shapes [16], making it an efficient parametrisation method for optimisation. Figure 6 describes the parametrisation scheme:

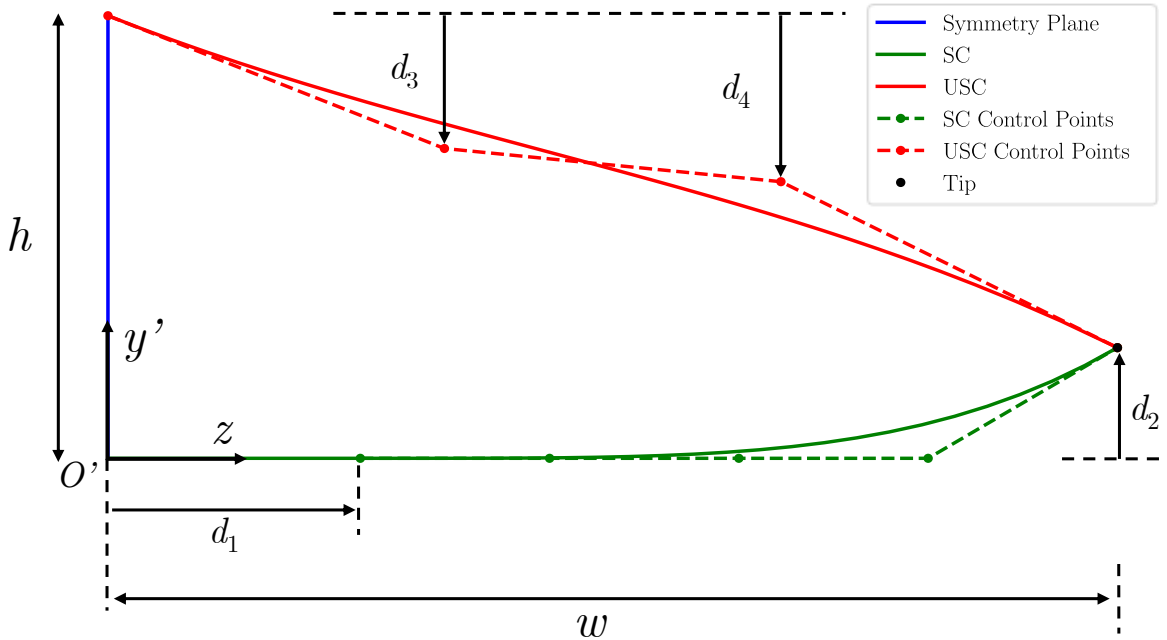


Figure 6: Parametrisation of the Base Plane

As seen in Figure 6, a local 2D coordinate system is setup such that  $y' = y + h$  and  $z' = z$ .  $w$  represents the half-width of the waverider.

The SC is composed of a flat region, defined by the distance  $d_1$ , and a curved region following it. The curved region is defined as a fourth order Bézier curve with five control points. These are equally spaced in  $z$  and lie on the line  $y' = 0$ , except for the rightmost whose vertical position is determined by the distance  $d_2$ . Furthermore, the USC is defined as a third order Bézier curve with four control points. These are also equally spaced in  $z$ , while the vertical positions of the two internal points are determined by the distances

$d_3$  and  $d_4$ . The two Bézier curves are defined as shown in Equation (2):

$$\begin{cases} \mathbf{M}_{\text{USC}} = (1-t)^3 \mathbf{P}_0 + 3(1-t)^2 t \mathbf{P}_1 + 3(1-t) t^2 \mathbf{P}_2 + t^3 \mathbf{P}_3 \\ \mathbf{M}_{\text{SC}} = (1-t)^4 \mathbf{P}_0 + 4(1-t)^3 t \mathbf{P}_1 + 6(1-t)^2 t^2 \mathbf{P}_2 + 4(1-t) t^3 \mathbf{P}_3 + t^4 \mathbf{P}_4 \end{cases} \quad (2)$$

where  $t \in [0, 1]$ ,  $\mathbf{M} = (z, y')$  is a point along the curve and  $\mathbf{P}_i = (z_i, y'_i)$  represents the  $i$ th control point of each curve, sorted in an ascending order from left to right. These distances are then normalised as follows

$$\begin{cases} X1 = \frac{d_1}{w} & \text{with } d_1 \in [0, w] , \quad X1 \in [0, 1] \\ X2 = \frac{d_2}{h} & \text{with } d_2 \in [0, h] , \quad X2 \in [0, 1] \\ X3 = \frac{d_3}{(h-d_2)} & \text{with } d_3 \in [0, h-d_2] , \quad X3 \in [0, 1] \\ X4 = \frac{d_4}{(h-d_2)} & \text{with } d_4 \in [0, h-d_2] , \quad X4 \in [0, 1] \end{cases} \quad (3)$$

which gives the final four geometric parameters  $[X1, X2, X3, X4]$ .

The following Section 2.3.2 describes the application of the osculating cone theory [38] on the Base Plane to obtain the remainder of the waverider geometry.

### 2.3.2 Osculating Cone Theory

Osculating Cone Theory (OCT) [38] consists in discretising the flowfield into spanwise stations along the SC. These stations, known as osculating planes, are locally normal to the SC and are in the direction of the flow. Within each plane, the flow is assumed conical. Moreover, to maintain the same shock strength in the spanwise direction, the shock angle  $\beta$  is assumed constant in all planes [16]. This assumption also means conical flow must only be solved once, which greatly reduces computational cost [20]. Figure 7 shows an osculating plane.

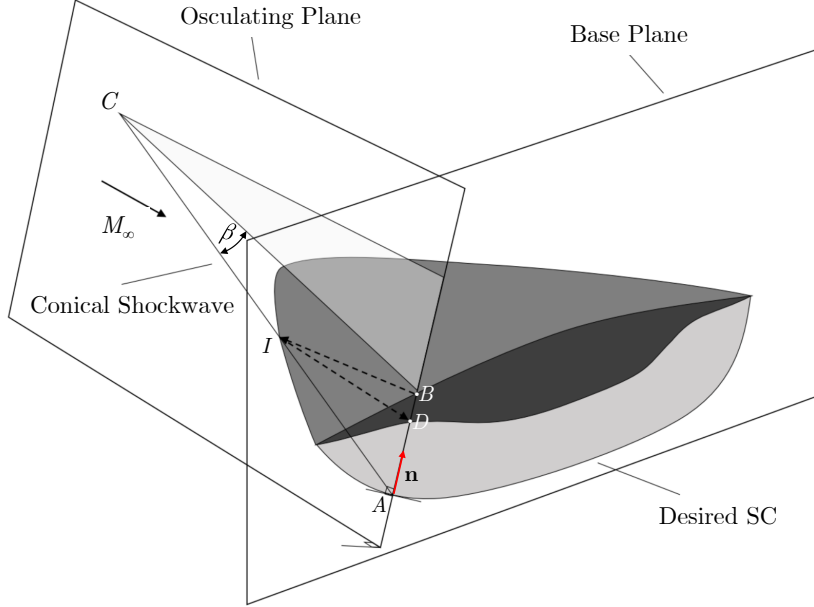


Figure 7: Representation of a waverider with an osculating plane, slightly modified figure from [16]

In the flat region of the shockwave, OCT cannot be applied due to the lack of curvature. Instead, the waverider in this region is wedge-derived as shown in Figure 3. As a result, the length of the waverider at the symmetry plane is determined as  $l = h / \tan(\beta)$ . Moreover, the deflection angle  $\theta$  is obtained through the  $\theta - \beta - M$  relation [83], given in Equation (4):

$$\tan(\theta) = \frac{2 \cot(\beta) (M_\infty^2 \sin^2(\beta) - 1)}{M_\infty^2 (\gamma + \cos(2\beta)) + 2} \quad (4)$$

Where  $\gamma = 1.4$  is the ratio of specific heats for air. This relationship allows the waverider geometry throughout the rest of the flat section to be computed.

The process of applying OCT through the curved region is summarised below for each osculating plane, while making references to the different elements of Figure 7:

- 1. Find intersection of the osculating plane with the USC**

The intersection corresponds to point  $B$  and is found by computing the inward pointing normal vector  $\mathbf{n}$ .

- 2. Find intersection between the shock line and the freestream flow**

The intersection corresponds to point  $I$  and is found as the point where  $y_I = y_B$  along the shock line. To find the shock line, the location of the cone centre  $C$  is determined by calculating the local radius of curvature.

- 3. Compute the upper surface**

This is done by lofting the straight lines between  $I$  and  $B$  at each osculating plane.

- 4. Streamline tracing**

Having already solved the Taylor–MacColl equations [84] which describe conical flow for a given cone angle and shock angle, the solution is propagated from point  $I$  until the back of the waverider is reached at point  $D$ . This process traces the streamline

from  $I$  to  $D$ . Similar to the upper surface, the streamlines along the span are then lofted together to produce the lower surface.

### 2.3.3 Waverider Generator

The open-source Python library “Waverider Generator” [85], programmed and published by the author, integrates the osculating cone theory and the aforementioned parametrisation. It was used to produce all geometries in this work. To generate a geometry, the user makes use of the class `waverider` and then uses the `to_CAD` function to produce a CAD model. An example of this is shown in Appendix C. For simplicity, the inputs and outputs of the procedure are summarised in Figure 8:

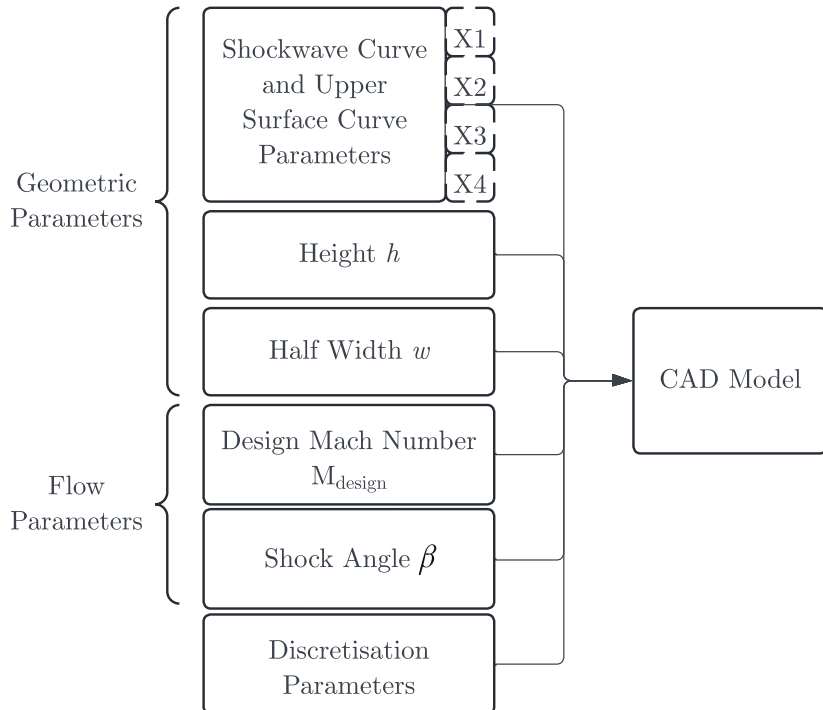


Figure 8: Inputs/Output of Waverider Generator [85]

The geometric parameters are those which directly influence the geometry of the waverider. The flow parameters also play a role in determining the shape and dimensions of the waverider but reflect the desired flow conditions.  $M_{\text{design}}$  is the Mach Number for which the waverider is designed for, not to be confused with the freestream Mach Number  $M_\infty$ . If  $M_{\text{design}} = M_\infty$ , then the waverider is flown in design condition and the opposite scenario refers to operating in off-design conditions.

On the other hand, the discretisation parameters influence the accuracy of the final CAD model, as the upper and lower surfaces are interpolated between the discrete points which define them. The reader is referred to the documentation<sup>1</sup> for further details on those parameters.

Figure 9 demonstrates the variety of shapes which can be obtained through Waverider Generator:

---

<sup>1</sup><https://github.com/jade5638/waverider-generator>

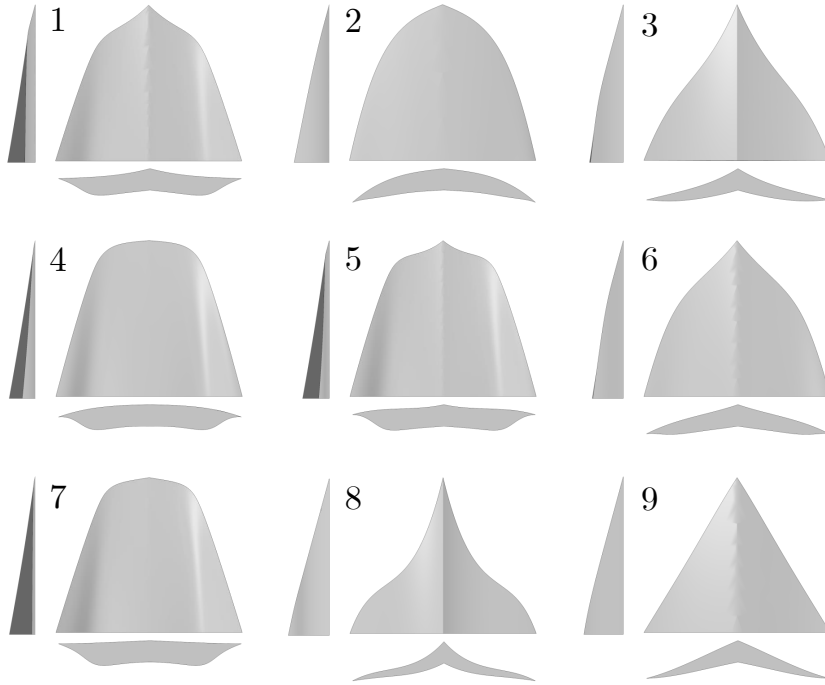


Figure 9: Example of 9 configurations obtained through Waverider Generator with  $\beta = 15^\circ$ ,  $M_{\text{design}} = 6.5$ ,  $w = 4.2$  m and  $h = 1.876$  m.

The views from the bottom, the back and the side are shown for each configuration in Figure 9. The corresponding set of geometric parameters are summarised in Table 3:

Table 3: Values of the design variables in Figure 9

Number	X1	X2	X3	X4
1	0.117	0.758	0.819	0.888
2	0.219	0.180	0.099	0.192
3	0.145	0.239	0.604	0.743
4	0.119	0.699	0.047	0.111
5	0.111	0.755	0.677	0.109
6	0.234	0.290	0.356	0.467
7	0.053	0.922	0.402	0.915
8	0.597	0.045	0.869	0.577
9	0.264	0.082	0.337	0.793

#### 2.3.4 Design Space Inputs

Son *et al.* [16] made use of the geometric parameters X1...X4 to define a design space for optimisation. Their design space is defined as:

$$\mathbf{V} = \begin{cases} \mathbf{X1} \in [0, 1[ \\ \mathbf{X2} \in [0, 1] \\ \mathbf{X3} \in [0, 1] \\ \mathbf{X4} \in [0, 1] \end{cases} \quad \text{with respect to GC : } \frac{\mathbf{X2}}{(1 - \mathbf{X1})^4} < \frac{7}{64} \left( \frac{w}{h} \right)^4 \quad (5)$$

Where  $\mathbf{V}$  is the vector of input/design variables and the other parameters ( $h$ ,  $w$ ,  $M_{\text{design}}$ ,  $\beta$ ) are kept constant.

The constraint shown in Equation (5) will be referred to as the Geometric Constraint (GC) hereafter. The GC is a result of OCT and is established to ensure the inverse design method does not fail. Indeed, OCT requires the intersection between any two osculating planes to be above the USC [16, p. 5]. This is because the opposite scenario would result in the streamlines of both planes intersecting, leading to an invalid geometry [16]. As such, the GC dynamically restricts the maximum value that  $X_2$  can take based on the value of  $X_1$ .

The same design space will be used in this study, with the addition of the design Mach number  $M_{\text{design}}$  as a design variable. This is because the optimisation problems considered here are multi-point and aim to optimise the performance of the waverider across two flight conditions, outlined in Section 2.1. The following Section 2.3.4.1 details the rationale behind the inclusion of  $M_{\text{design}}$  in the design space.

#### 2.3.4.1 Design Mach Number & Shockwave Considerations

A waverider designed for Mach 5 will not maintain the design shockwave shape at Mach 8 and vice versa. For this reason, it makes sense in this optimisation framework to consider the influence of  $M_{\text{design}}$  on the shockwave shape as this is part of the wide-speed problem. Figure 10 shows the shock angle at the symmetry plane, denoted as  $\beta_0$ , against  $M_{\text{design}}$  for both flight conditions. Here, the design shock angle is  $\beta = 15^\circ$ . The curves are obtained by making use of the  $\beta - \theta - M$  relation covered in Equation (4).

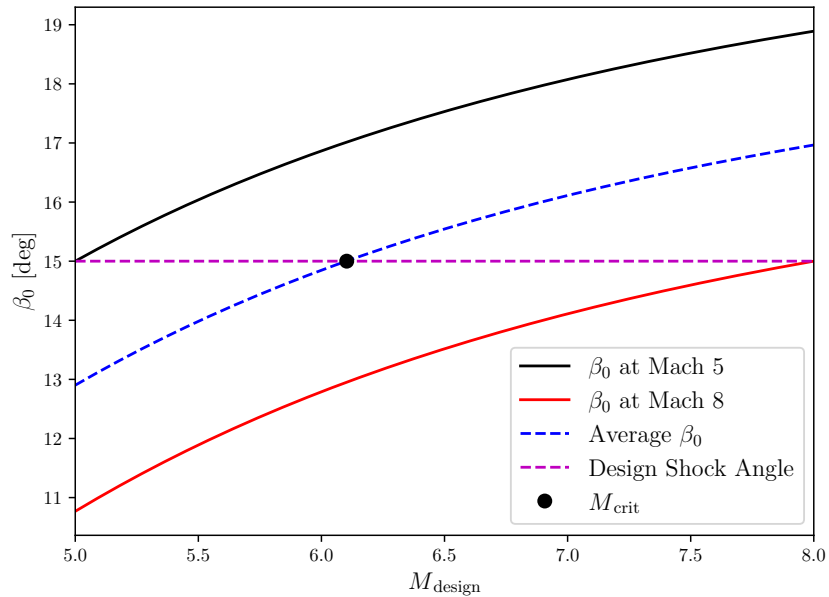


Figure 10: Shock angle at symmetry plane against  $M_{\text{design}}$

As expected, at Mach 5, a waverider designed for that flight condition will have  $\beta_0 = \beta = 15^\circ$ . Similarly, at Mach 8, a waverider designed for that flight condition will display  $\beta_0 = \beta = 15^\circ$ . However, when  $M_\infty \neq M_{\text{design}}$ , the resulting  $\beta_0$  is either higher (Mach 5) or lower (Mach 8) than the target. For simplicity and consistency across a range of

waverider shapes, the change in the shockwave shape can therefore be quantified as:

$$\Delta\beta = |\beta_0 - \beta| \quad (6)$$

Where  $\beta$  is the target shock angle.

At  $M_{\text{design}} = M_{\text{crit}} \approx 6.1$ ,  $\Delta\beta$  is equal for both flight conditions, and this can serve as an important point to compromise between the two design conditions.

Furthermore, it's important to note that  $M_{\text{design}}$ 's contribution's to the geometrical properties of the waverider is an increase in the deflection angle with an increase in  $M_{\text{design}}$ , as predicted by the  $\beta - \theta - M$  relation (see Equation (4)). This translates to an increase in the thickness of the waverider for a specific shockwave shape. An example is shown in Figure 11, where this phenomenon is clearly visible:

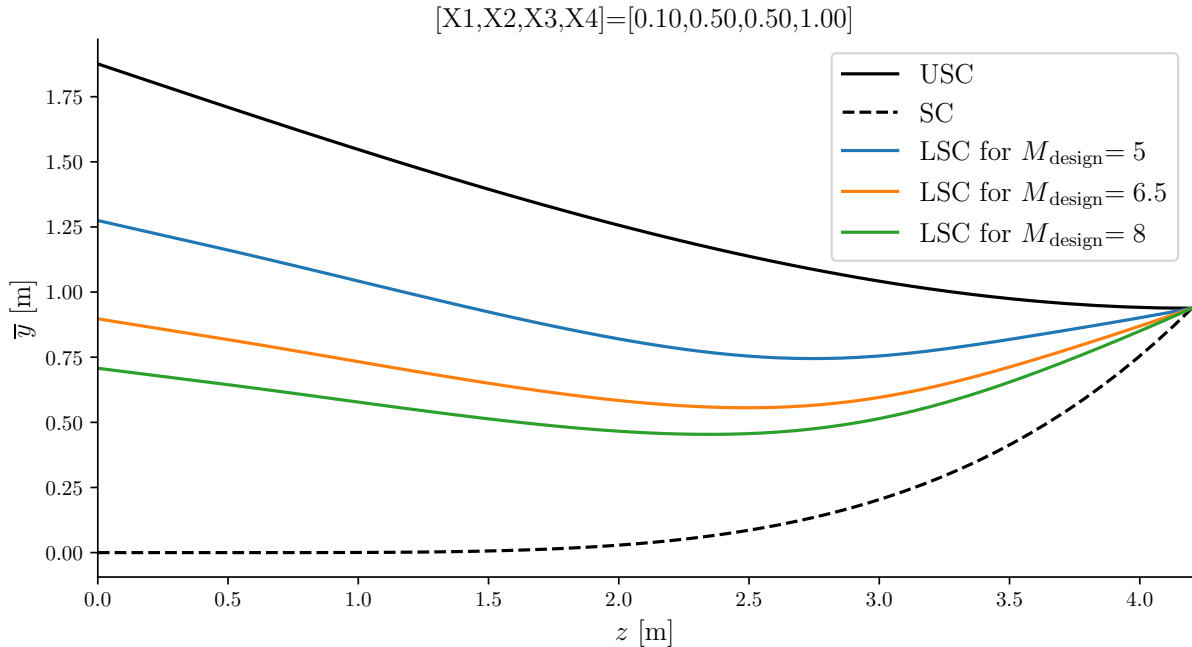


Figure 11: Effect of  $M_{\text{design}}$  on the lower surface of the waverider. View from the base plane. For  $\beta=15^\circ$ ,  $h = 1.876$  m and  $w = 4.2$  m.

$M_{\text{design}}$  is added to Son *et. al's* [16] design space to give the final design space used in this study:

$$\mathbf{X} = [M_{\text{design}}, X_1, X_2, X_3, X_4] \quad (7)$$

where  $\mathbf{X}$  is the vector of design variables and

$$\mathbf{X} = \begin{cases} M_{\text{design}} & \in [5, 8] \\ X_1 & \in [0, 1[ \\ X_2 & \in [0, 1] \\ X_3 & \in [0, 1] \\ X_4 & \in [0, 1] \end{cases} \quad \text{with respect to} \quad \begin{cases} \text{GC : } \frac{X_2}{(1-X_1)^4} < \frac{7}{64} \left(\frac{w}{h}\right)^4 \\ \beta = 15^\circ \\ h = 1.876 \text{ m} \\ w = 4.2 \text{ m} \end{cases} \quad (8)$$

This leads to a length  $l = h / \tan(\beta) \approx 7.00133 = 7$  m.

### 2.3.5 Design Space Dynamics

The GC (see Equation (8)) limits the maximum value that  $X_2$  can take as a function of  $X_1$ . By denoting the RHS of the GC as  $k$ ,  $X_{2\max}$  can be calculated as:

$$X_{2\max} = \min(1, k(1 - X_1)^4) \quad (9)$$

Figure 12 plots the corresponding constraint curve:

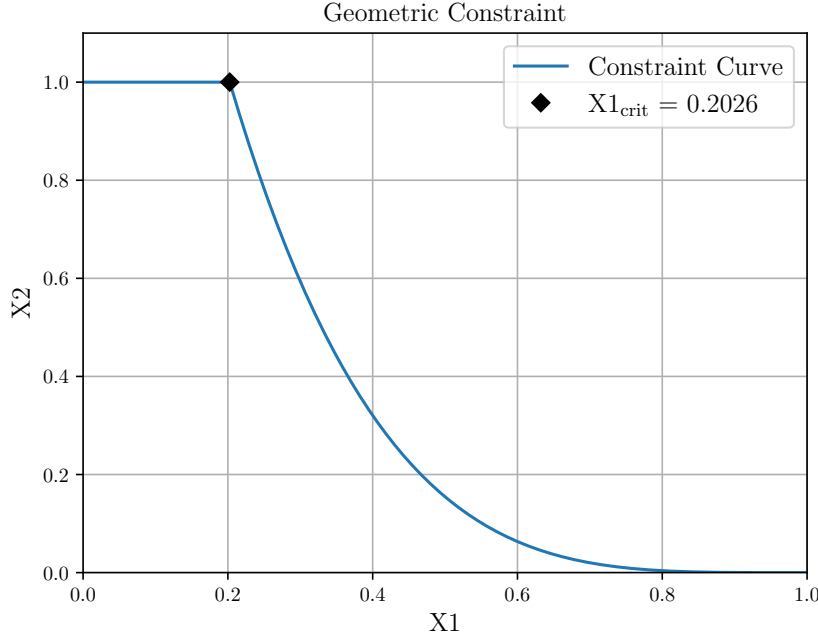


Figure 12: Geometric constraint curve

As shown in Figure 12, when  $X_1 \leq X_{\text{crit}}$ ,  $X_2$  is not limited and can take any value between 0 and 1. After that point,  $X_{2\max}$  is less than 1 and decreases quartically. Note that throughout this work,  $k$  is multiplied by 0.9 to prevent floating-point errors during the optimisation process, and this is in line with the work by Son *et al.* [16].

In addition to the GC, the design space established in the previous section exhibits intricate relationships between the variables because of the parameter  $X_2$ . Indeed, as seen in Equation (3) and Figure 6, the parameters  $X_3$  and  $X_4$  are coupled to  $X_2$  such that, as  $X_2$  increases, their influence on the geometry decreases. Ultimately, when  $X_2 = 1 \Rightarrow d_2 = h$ ,  $X_3$  and  $X_4$  become redundant as the distances  $d_3$  and  $d_4$  will be calculated as

$$\begin{cases} d_3 = X_3 \cdot (h - d_2) = X_3 \cdot 0 = 0 \text{ m} \\ d_4 = X_4 \cdot (h - d_2) = X_4 \cdot 0 = 0 \text{ m} \end{cases} \quad (10)$$

which will result in the same geometry regardless of the values of  $X_3$  and  $X_4$ . This configuration corresponds to a waverider with a flat USC. Hereafter,  $X_3$  and  $X_4$  will be treated as 0 whenever a solution with  $X_2 = 1$  is reached to denote this specific case. It

can be written in terms of  $\mathbf{X}$  as:

$$\mathbf{X}_{\text{Flat USC}} = \begin{bmatrix} M_{\text{design}} \\ X_1 \\ X_2 \\ X_3 \\ X_4 \end{bmatrix} = \begin{bmatrix} M_{\text{design}} \\ X_1 \\ 1 \\ 0 \\ 0 \end{bmatrix} \text{ w.r.t } X_1 \leq X_{1\text{crit}} \quad (11)$$

Additionally, setting  $X_2 = 0$  results in a planar shockwave. As a consequence, when  $X_2 = 0$ ,  $X_1$  becomes redundant as the entirety of the SC is already flat. Similar to the previous case, this case will be denoted hereafter as:

$$\mathbf{X}_{\text{Flat SC}} = \begin{bmatrix} M_{\text{design}} \\ X_1 \\ X_2 \\ X_3 \\ X_4 \end{bmatrix} = \begin{bmatrix} M_{\text{design}} \\ 0 \\ 0 \\ X_3 \\ X_4 \end{bmatrix} \quad (12)$$

### 2.3.6 Design Space Outputs

Having established the inputs of the design space, many outputs of interest can be obtained, some of which are used in the optimisation problems. A database containing these outputs for 99 points across the design space was created and stored in this project's GitHub Repository<sup>2</sup>. The full sampling strategy is outlined later in Section 2.5.1. Table 4 lists the main outputs considered in this study and the methods by which these were obtained.

Table 4: Outputs of the design space

Symbol	Units	Output Description	Method
$D$	N	Inviscid Drag force	Inviscid CFD
$L$	N	Inviscid Lift force	Inviscid CFD
$(L/D)$	[-]	Inviscid Lift to Drag ratio	Inviscid CFD
$D^{\text{visc}}$	N	Viscous Drag force	Viscous Drag Corrections
$V$	$\text{m}^3$	Internal Volume	cadquery [86]
$S_{\text{wet}}$	$\text{m}^2$	Wetted Surface Area	cadquery [86]
$v_{\text{eff}}$	[-]	Volumetric Efficiency	$V^{2/3}/S_{\text{wet}}$

Note that, for convenience, all forces are those acting on only half the geometry as a symmetry plane boundary condition is applied in the CFD setup. Moreover, unless

<sup>2</sup>[https://github.com/jade5638/jade\\_nassif\\_thesis](https://github.com/jade5638/jade_nassif_thesis)

specified, the Lift and Drag are obtained at angle of attack  $\alpha$  of  $0^\circ$  representing cruise condition and this is the case throughout the optimisation. Furthermore, the subscripts “M5” and “M8” will be used hereafter to denote forces at the M5 and M8 flow conditions respectively.

On the other hand, geometric properties such as  $V$ ,  $S_{\text{wet}}$  and  $v_{\text{eff}}$  are obtained on the entire geometry through `cadquery` [86], which is a Python library for handling and creating CAD models.

## 2.4 Performance Estimation - Inviscid Flow

This section describes the CFD setup used to solve the inviscid flow around a waverider. Inviscid flow is represented by the Euler Equations which are derived from the Navier Stokes Equations [87] by omitting viscous effects. In this case, the flow is solved in a steady-state to represent cruising condition and minimise computational cost.

The commercial CFD solver Simcenter STAR-CCM+ 19.02.009-R8 [82] was used to conduct all CFD simulations in this work, owing to its compact user interface which handles all stages of the simulation from meshing to post-processing. This feature, along with the use of Java macros, provides a significant advantage in terms of workflow automation which is not found alternatives such as Ansys Fluent.

Throughout this section, the figures produced as well as the Grid Convergence Study were done on the waverider with

$$\mathbf{X} = [M_{\text{design}}, X_1, X_2, X_3, X_4] = [6.5, 0.25, 0.5, 0.5, 0.5]$$

which corresponds to the mid-range of each design variable - except for  $X_1$  as this would break the GC.

### 2.4.1 Domain and Mesh

The domain presented in Figure 13 was kept for all inviscid CFD simulations.

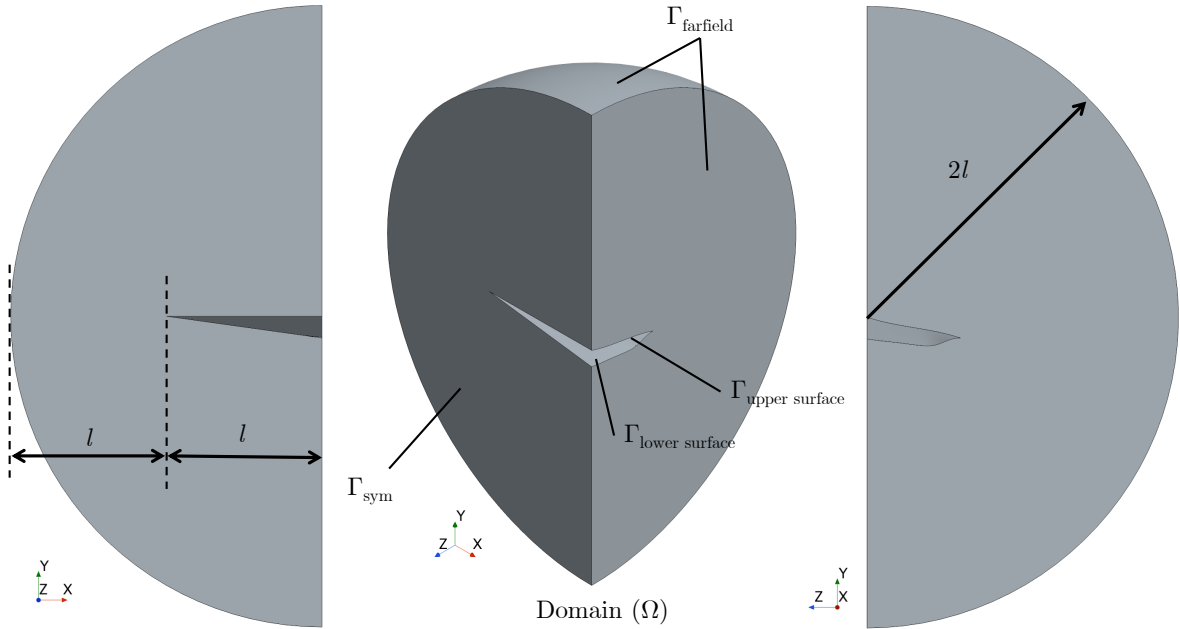


Figure 13: Inviscid domain  $\Omega \in \mathbb{R}^3$  used in this study, showing a view from the symmetry plane (left), isometric view (middle) and view from the back plane (right)

As is commonly done in the literature [16, 58, 79], the wake behind the waverider is not included in the domain due to the lack of viscosity which prevents an accurate representation of the wake. Furthermore, only half the body is included due to the symmetry about the XY plane. The boundaries of the domain  $\partial\Omega$  have been divided into four regions such that:

$$\partial\Omega = \Gamma_{\text{farfield}} \cup \Gamma_{\text{sym}} \cup \Gamma_{\text{upper surface}} \cup \Gamma_{\text{lower surface}} \quad (13)$$

The boundary conditions applied to each region are summarised in Table 5, where  $\mathbf{n}$  represents the vector normal to the relevant boundary:

Table 5: Boundary conditions applied

Region(s)	BC	Implementation
$\Gamma_{\text{farfield}}$	Freestream	$\begin{cases} \mathbf{u} = U_\infty[\cos(\alpha), \sin(\alpha), 0] \\ p = p_\infty \\ T = T_\infty \end{cases}$
$\Gamma_{\text{sym}}$	Symmetry Plane	$\begin{cases} \mathbf{u} \cdot \mathbf{n} = 0 \\ \frac{\partial T}{\partial \mathbf{n}} = 0 \\ \frac{\partial p}{\partial \mathbf{n}} = 0 \end{cases}$
$\Gamma_{\text{upper surface}}$ $\Gamma_{\text{lower surface}}$	No-slip Adiabatic Walls	$\begin{cases} \mathbf{u} = 0 \\ \frac{\partial T}{\partial \mathbf{n}} = 0 \\ \frac{\partial p}{\partial \mathbf{n}} = 0 \end{cases}$

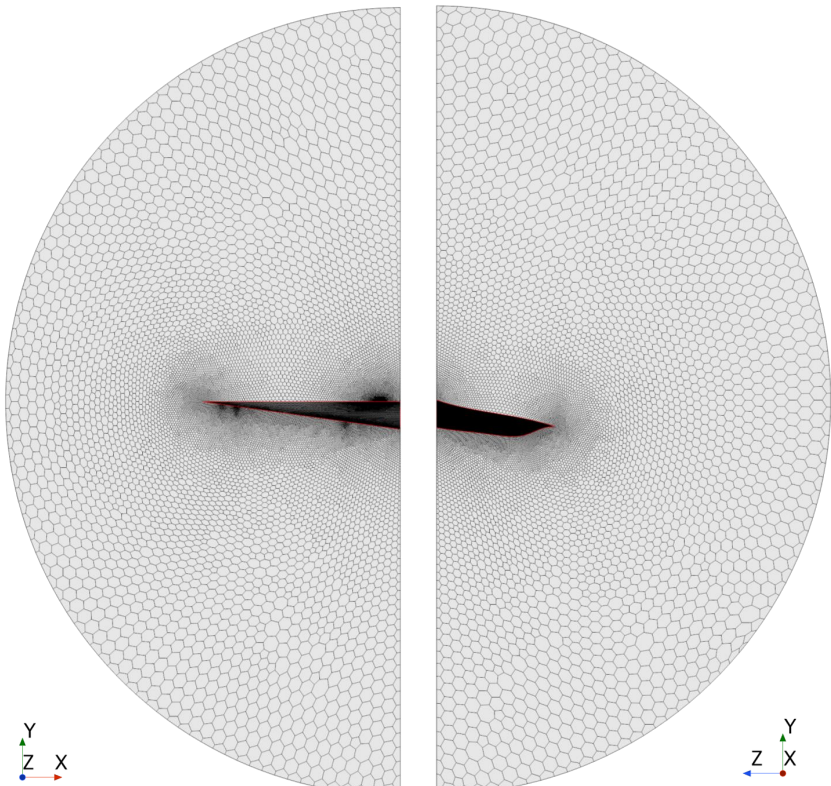
The mesh is unstructured and generated using Polyhedral elements. A minimum face

quality of 0.15 was set to prevent poor quality cells from diverging the solution. A target surface size of 0.5 m was chosen along with a minimum surface size of 0.01 m. Moreover, the growth rate was fixed at 1.05 to maintain a smooth and gradual transition in the mesh and therefore capture the high gradients around the region of the shock with better accuracy. Finally, a local refinement was added around the lower surface as this is where the shockwave is present. These settings are summarised in Table 6.

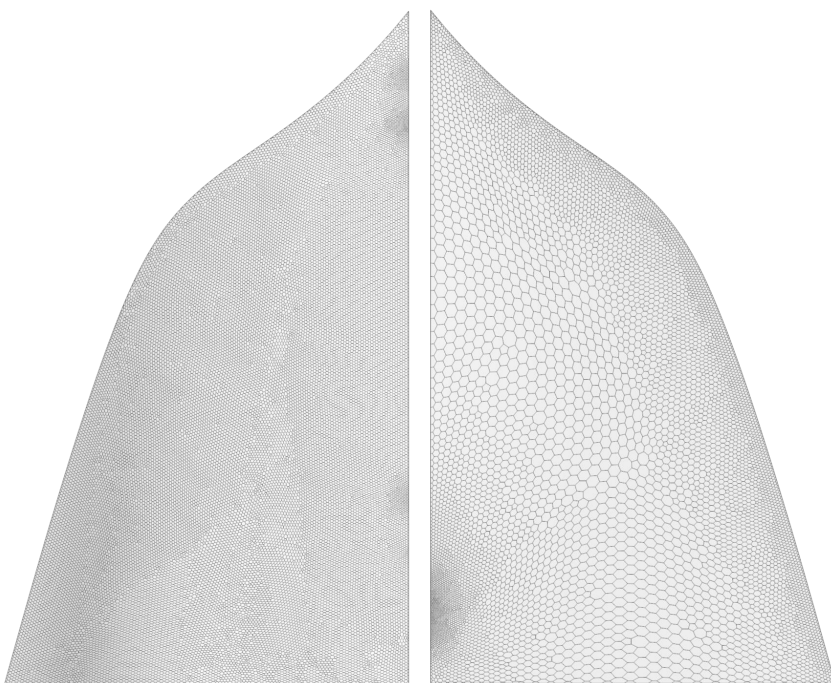
Table 6: Mesh settings

<b>Setting</b>	<b>Value</b>
Minimum Face Quality	0.15
Target Surface Size	0.5 m
Minimum Surface Size	0.01 m
Growth Rate	1.05
Lower Surface Refinement (Target Surface Size)	0.03 m

A typical mesh obtained with this setup is shown in Figure 14. The local sizing near the lower surface is clearly visible while the upper surface is coarser. Moreover, the lower surface refinement propagates to the region around the leading edge on the upper surface, and this is beneficial in capturing any potential flow spillage.



(a)



(b)

Figure 14: (a) View of the mesh from symmetry plane (left) and back plane (right)  
(b) View of the mesh on the lower surface (left) and upper surface (right)

### 2.4.2 Adaptive Mesh Refinement

The shockwave is the main feature of the flow and is responsible for the overwhelming majority of the lift and the drag. As such, Adaptive Mesh Refinement (AMR) was included in the CFD setup to ensure the sharp gradients around the shock are well captured and reasonable estimates of lift and drag are reached. The criterion chosen is shown in Equation (14):

$$C = \|\nabla M(x, y, z)\| \times s = \sqrt{\left(\frac{\partial M}{\partial x}\right)^2 + \left(\frac{\partial M}{\partial y}\right)^2 + \left(\frac{\partial M}{\partial z}\right)^2} \times s \quad (14)$$

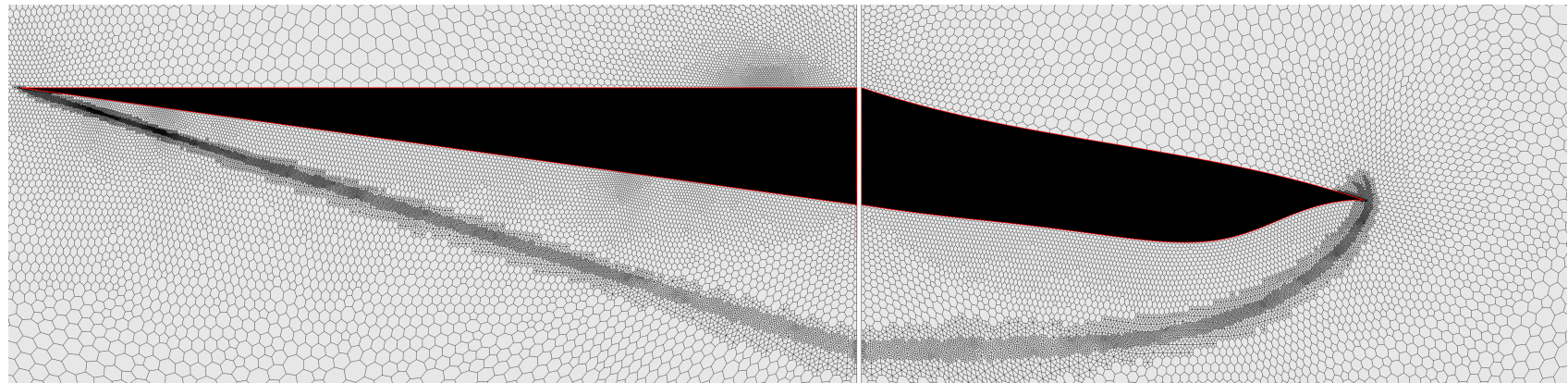
where  $M(x, y, z)$  is the local Mach number represented as a scalar field across the domain and  $s$  is the Adaptation Cell Size (ACS), calculated as “twice the maximum distance between a cell centroid and any of the cell vertices” in Star-CCM+ [82]. The criterion is implemented in StarCCM+ as a field function with the expression:

```
mag(grad($MachNumber)) * ($AdaptionCellSize)
```

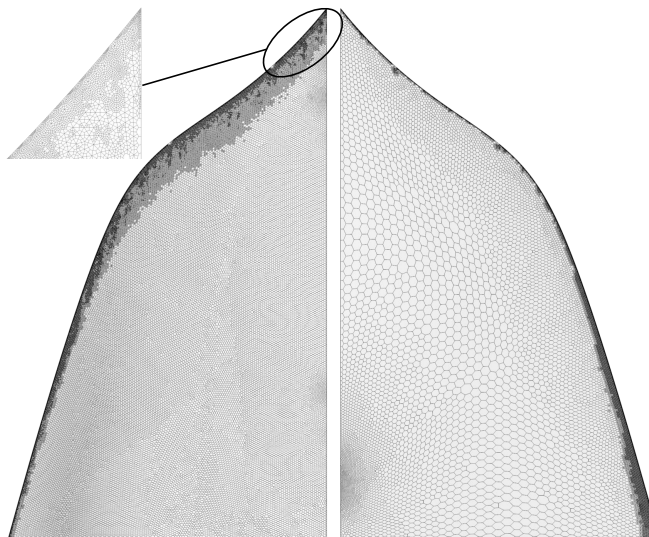
The refinement can take place when  $C \notin [0, 0.1]$ , with a maximum refinement level of 2. Furthermore, the minimum Face Validity was set at 0.9 to prevent bad quality cells in the refined regions. Additionally, only cells with an ACS greater than 0.001 m were eligible for refinement, and this was done to match the Minimum Surface Size set in Section 2.4.1.

AMR was set to take place every 100 iterations to allow the solution on the current mesh to reach a realistic steady-state convergence before being refined. A number of refinements  $n_{ref}$  is also predefined to serve as a minimum number of iterations before considering the convergence criterion. For example, if  $n_{ref} = 2$ , then a minimum of  $2 \times 100 = 200$  iterations is set before checking for convergence. Details on the convergence criterion are specified in Section 2.4.4.

Figure 15, where the waverider outline is shown in red, showcases this AMR setup after 3 refinements at  $\alpha = 0^\circ$  for the M5 flow condition. It is clear that the criterion is suitable for this type of flow as it successfully refines the region of the shock and the overflow to the upper surface.



(a)



(b)

Figure 15: (a) AMR on the symmetry plane (left) and back plane (right) with  $n_{\text{ref}} = 3$   
(b) AMR on the lower lower surface (left) and upper surface (right) with  $n_{\text{ref}} = 3$

### 2.4.3 Numerical Solver Configuration

This section details the numerical approach taken in solving the flow. Significant attention has been devoted to selecting settings which promote accuracy and convergence in hypersonic flow conditions.

#### 2.4.3.1 Real Gas

Given the hypersonic nature of the flow, the air cannot be assumed to be an ideal gas [88, 89] due to effects such as:

- ionisation
- dissociation
- excitation

These arise as a result of the shockwave and high speeds, and must be accounted for in the gas model. For this reason, a Real Gas model known as Equilibrium Air [90], recommended by Cross *et al.* [89] and the Star-CCM+ user guide [82] was chosen. This model is meant to account for such effects in the estimation of the flow quantities.

#### 2.4.3.2 Coupled Implicit Solver

The Coupled Implicit solver was employed as it is more suitable for compressible flows as the equations get solved simultaneously through pseudo-time marching [82, 89]. Moreover, the Advection Upstream Splitting Method (AUSM) + Flux Vector Splitting (FVS) [91] scheme was chosen to evaluate inviscid fluxes. The scheme is more stable than the alternative Roe Flux Difference Splitting (FDS) [92] scheme for inviscid hypersonic flows [82, 89]. Indeed, the latter is not robust in hypersonic conditions and may result in the appearance of several non-physical flow features near the region of the shock [93].

In addition to this, the Courant–Friedrichs–Lewy (CFL) number was determined through the Automatic Control method built into Star-CCM+ [82]. Furthermore, the Incomplete Lower Upper (ILU) [94] relaxation scheme was selected for the Algebraic Multigrid (AMG) Linear Solver as it “promotes faster convergence” [82] in hypersonic flows than the Gauss-Seidel scheme.

#### 2.4.3.3 Spatial Discretisation

A third order Monotonic Upstream-centered Scheme for Conservation Laws (MUSCL) scheme with central differencing was selected in conjunction with the Venkatatkrishnan [95] slope limiter. The scheme results in 3<sup>rd</sup> order accuracy except around regions with strong gradients, where the limiter reduces the accuracy to 2<sup>nd</sup> order [89].

The Venkatatkrishnan limiter [95] was favored over minmod [96] as the latter tends to be overly diffusive and therefore smear out strong gradients, which would compromise the accuracy of the solution around the shock. On the other hand, Venkatakrishnan is a limiter which is commonly used on unstructured meshes and is known to maintain good accuracy while also preventing spurious oscillations [97].

#### 2.4.3.4 Initialisation

Grid Sequencing Initialisation [82] was used to initialise the flowfield around the waverider. Grid Sequencing works by initialising the flow quantities then providing a first-order inviscid solution on a series of finer and finer grid levels until a certain convergence tolerance is reached [82]. Given the inviscid nature of the flow, this feature serves as a convergence accelerator and aims to reduce the number of iterations required to reach the stopping criterion [89].

The CFL number for the initialisation process was set at a low value of 2.5 due to the high gradients around the shock, which can produce instabilities later on in the solution if not properly resolved in the initialisation stage [82, 89].

#### 2.4.4 Convergence

The convergence of the lift to drag ratio  $L/D$  was chosen as a convergence criterion. This is because lift and drag are the two quantities which are obtained from the CFD setup and used in the optimisation problems, described in Section 2.6. The lift  $L$  and drag  $D$  were obtained as:

$$\begin{cases} L &= F_y \cos(\alpha) - F_x \sin(\alpha) \\ D &= F_x \cos(\alpha) + F_y \sin(\alpha) \end{cases} \quad (15)$$

Where  $\alpha$  is the angle of attack,  $F_x$  is the resultant force in the  $x$  direction and  $F_y$  is the resultant force in the  $y$  direction.

The solution is considered converged if

$$|(L/D)_{\max} - (L/D)_{\min}| < \epsilon \quad (16)$$

Where  $(L/D)_{\max}$  and  $(L/D)_{\min}$  are the maximum and minimum values of  $L/D$  over 40 sequential samples, and  $\epsilon = 1 \times 10^{-6}$ .

A maximum number of iterations was also set at 1000. In the event that convergence is not reached, the behavior of  $L/D$  is observed. If the quantity seems to oscillate about a certain value but does not settle enough to reach the established criterion, then the solution is still deemed valid and the last value of  $L/D$  is recorded.

#### 2.4.5 Flow Conditions

As specified earlier in Section 2.1, the multi-objective optimisation problems consider two flow conditions:

1. Mach 5 at 25 km altitude (M5)
2. Mach 8 at 30 km altitude (M8)

In both cases, estimates for various quantities such as atmospheric freestream pressure  $p_\infty$ , freestream velocity  $U_\infty$ , freestream static temperature  $T_\infty$  and freestream air density  $\rho_\infty$  were obtained through International Standard Atmosphere (ISA) calculations. In particular, the CFD Toolbox [98] program, with a Mean Sea Level (MSL) temperature of 15°, was used to estimate the respective quantities. The two flow conditions are summarised in Table 7:

Table 7: Flow conditions

	M5 at 25 km alt.	M8 at 30 km alt.
$p_\infty$ [Pa]	2506.0	1169.0
$U_\infty$ [m.s <sup>-1</sup> ]	1490.0	2416.0
$T_\infty$ [K]	221.65	226.65
$\rho_\infty$ [kg.m <sup>-3</sup> ]	$3.940 \times 10^{-2}$	$1.797 \times 10^{-2}$

#### 2.4.6 Grid Convergence Study

A Grid Convergence Study (GCS) was done to determine an appropriate grid setup for both flow conditions described in Section 2.4.5. The initial mesh settings specified in Section 2.4.1 were used, the objective being to determine the appropriate number of refinements  $n_{\text{ref}}$ . As such, four grid levels were considered in the study, from no refinement ( $n_{\text{ref}} = 0$ ) to three refinements ( $n_{\text{ref}} = 3$ ). The results are summarised in Tables 8 and 9.

Table 8: Grid convergence study at the M5 flow condition

$n_{\text{ref}}$	Cells	Iterations	$(L/D)_{M5}$
0	$1.78 \times 10^5$	129	6.840425
1	$7.19 \times 10^5$	199	6.850357
2	$2.16 \times 10^6$	356	6.853450
3	$2.26 \times 10^6$	356	6.853264

At M5, there is not much change in the number of cells between  $n_{\text{ref}} = 2$  and  $n_{\text{ref}} = 3$  and also little change in the Lift to Drag ratio. However, the ratio does vary visibly between  $n_{\text{ref}} = 0$  and  $n_{\text{ref}} = 2$ . For this reason, a total of 2 refinements were chosen for the M5 flight condition.

Table 9: Grid convergence study at the M8 flow condition

$n_{\text{ref}}$	Cells	Iterations	$(L/D)_{M8}$
0	$1.78 \times 10^5$	119	6.796198
1	$1.25 \times 10^6$	174	6.810751
2	$4.30 \times 10^6$	265	6.811526
3	$1.68 \times 10^7$	NA	NA

At M8, the number of cells after each refinement is much higher than at M5 and this is due to the increase in Mach number leading to stronger gradients around the shock. Since the AMR criterion is based on the magnitude of the gradient of the Mach number, more cells will be refined as a result. At  $n_{\text{ref}} = 3$ , convergence issues were observed which prevented a solution from being recorded. Moreover, little change is observed in the solution between 1 and 2 refinements. For these reasons, 1 refinement was deemed sufficient at M8.

#### 2.4.7 Schlieren Imaging

Schlieren imaging [99] is a type of flow visualisation method which allows sharp flow features like shocks to be visualised. Here, a digital version of the method is implemented by considering the magnitude of the first derivative of density. The Schlieren number is mathematically defined as:

$$\text{Schlieren} = \|\nabla\rho(x, y, z)\| \quad (17)$$

which is implemented through a field function in StarCCM+ [82] as:

$$\text{mag}(\text{grad}(\$\text{Density}))$$

#### 2.4.8 High Performance Computing

To complete this work within the allocated time-frame, Cranfield University's High Performance Computing (HPC) facilities were used to run all CFD simulations. 16 cores were selected by default with a maximum time of one hour per simulation. In most cases, the computational time did not exceed 30-40 minutes.

### 2.5 Surrogate Modelling

The first step in building a surrogate model is to determine a set of sample points to accurately represent the design space and which will be used to train the model. As such, Section 2.5.1 focuses on the sampling methodology while Section 2.5.2 focuses on the training and validation of the surrogate models used in optimisation. The Surrogate Modeling Toolbox (SMT) Python library [100] was chosen to conduct all the steps outlined in these sections, as it provides a wide range of tools and options to construct surrogate models.

#### 2.5.1 Sampling

The Latin Hypercube Sampling method [101] was selected to sample the design space due to its numerous advantages over classic random sampling. Firstly, it ensures a thorough coverage of the parameter space across every dimension by partitioning each parameter's range into equal segments and sampling within each segment [102]. Secondly, Latin Hypercube Sampling ensures that no point is sampled more than once, as it keeps track of previously chosen points when adding new ones [102]. These advantages reflect the importance of obtaining a diverse set of samples in the five-dimensional space considered for optimisation.

In the work by Son *et al.* [16], which considers the same design space with the exception of the design Mach number, a final set of 60 points were used to train the surrogate models for volume,  $C_D$  and  $C_L$ . However, the latter two displayed poor accuracy in some regions, which could be partly due to an insufficient number of points. For this reason, and given the addition of  $M_{\text{design}}$  in the design space, a target was set to sample 100 points.

Due to the Geometric Constraint (see Section 2.3.4) which dynamically restricts X2, 500 samples were initially obtained via Latin Hypercube Sampling and these were then filtered to only keep the ones which satisfy the constraint, resulting in 183 valid points. The K-Means clustering algorithm, as implemented in the Scikit-learn Python package

[103], was then applied to select 100 representative points from this set. These can be seen in Appendix B, where each point has a corresponding index  $i \in [1, 100]$  and is referred to as Waverider  $i$ . This terminology will be used hereafter to refer to the  $i$ th sample point of the database. Waverider 63 was omitted from the set due to meshing issues, leading to 99 final sample points. Slices of the sampling across the design space are shown in Figure 16.

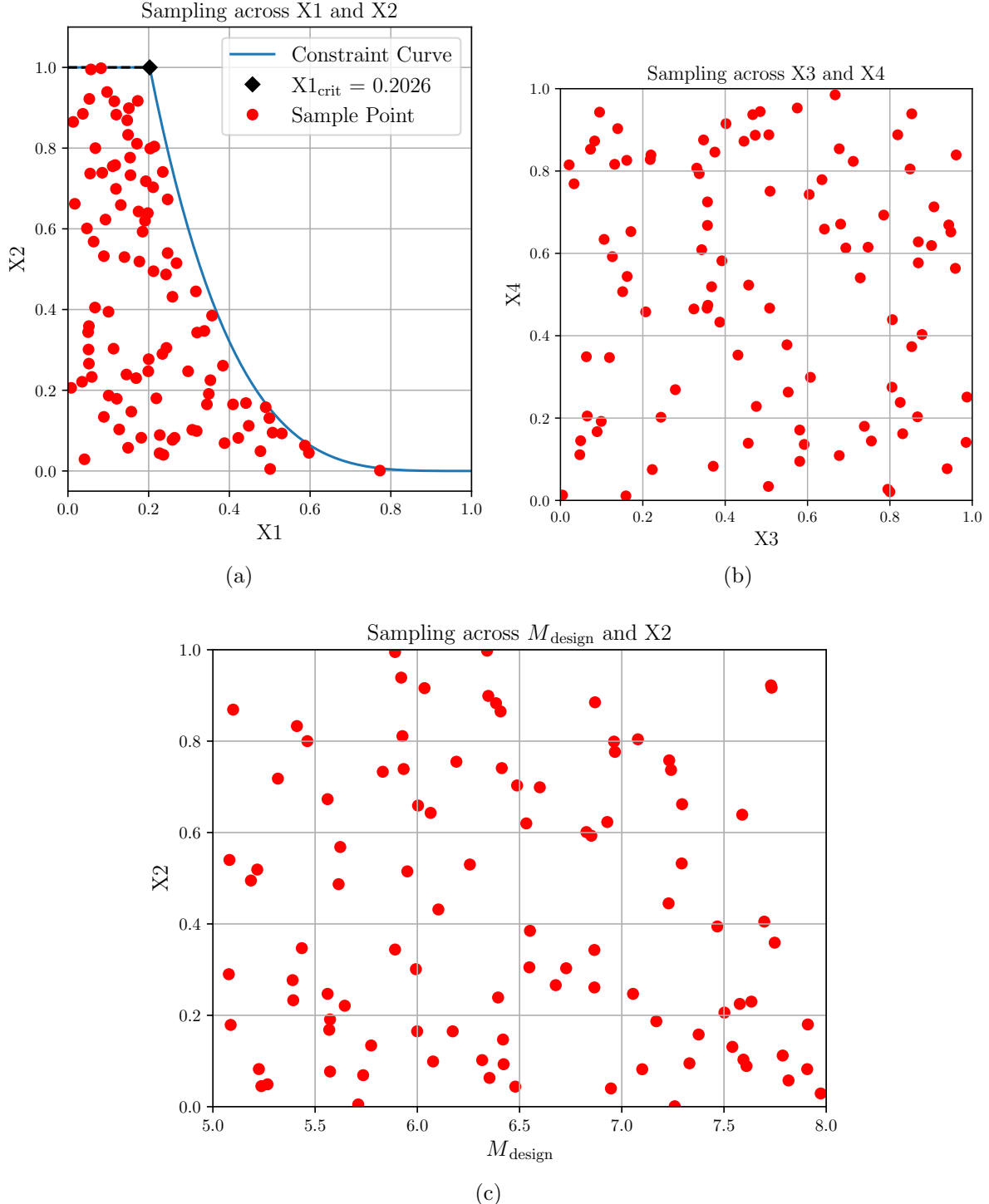


Figure 16: (a) Sample points across X1 and X2  
 (b) Sample points across X3 and X4  
 (c) Sample points across M<sub>design</sub> and X2

### 2.5.2 Kriging Surrogate Model

An ordinary Kriging surrogate model [104], may be represented as:

$$\hat{y}(\mathbf{X}) = \beta_0 + Z(\mathbf{X}) \quad (18)$$

Where  $\hat{y}(\mathbf{X})$  is the predicted output,  $\mathbf{X}$  is the vector of design variables,  $\beta_0$  is the regression coefficient and  $Z(\mathbf{X})$  is the realisation of a Gaussian process with zero mean and spatial covariance between two points  $\mathbf{X}$  and  $\mathbf{X}'$  given as:

$$\text{cov}(Z(\mathbf{X}), Z(\mathbf{X}')) = \sigma_Z^2 R(\mathbf{X}, \mathbf{X}') \quad (19)$$

Where  $R$  is a correlation function and  $\sigma_Z^2$  is the variance of the process.

In this context, Kriging provides many advantages over other types of surrogate models:

1. Exact interpolation, meaning the predicted output for the known training points matches the training data [105]. Here, the CFD setup and other methods used to obtain the relevant outputs are assumed robust enough so that they produce little to no noise, and so this features complements this assumption.
2. Can model both linear and non-linear relationships [106].
3. Simple to implement compared to a Neural Network whose meta-parameters and architecture need extensive tuning [106].

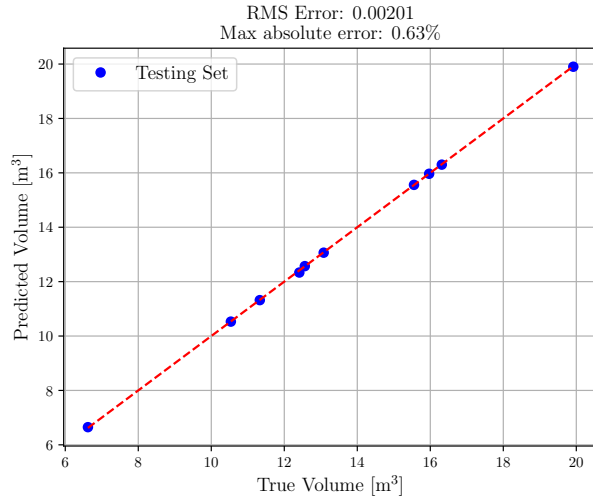
A Kriging model was built for each of the following quantities:

- $V$  (Internal Volume)
- $S_{\text{wet}}$  (Wetted Area)
- $L_{M5}$  (Lift at M5)
- $L_{M8}$  (Lift at M8)
- $D_{M5}$  (Drag at M5)
- $D_{M8}$  (Drag at M8)

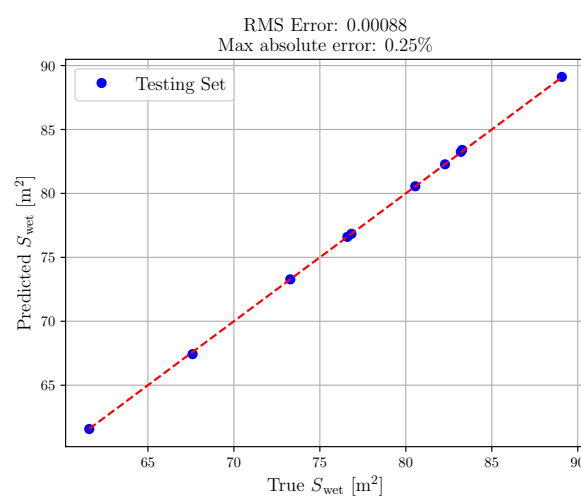
The samples obtained via Latin Hypercube Sampling (see Section 2.5.1) were first separated into a testing (10%) and a training (90%) dataset. The KRG class of the SMT Python package [100] was then used to train the surrogate models, each instance of this class representing an individual surrogate model. The models were then evaluated on testing data and this is shown in Figure 17. For each surrogate model, the percentage of maximum absolute error and the Root Mean Square (RMS) error, calculated as in Equation (20), are included in the corresponding plot.

$$\text{RMS Error} = \sqrt{\frac{1}{n_{\text{test}}} \sum_{i=1}^{n_{\text{test}}} e_i^2} \quad (20)$$

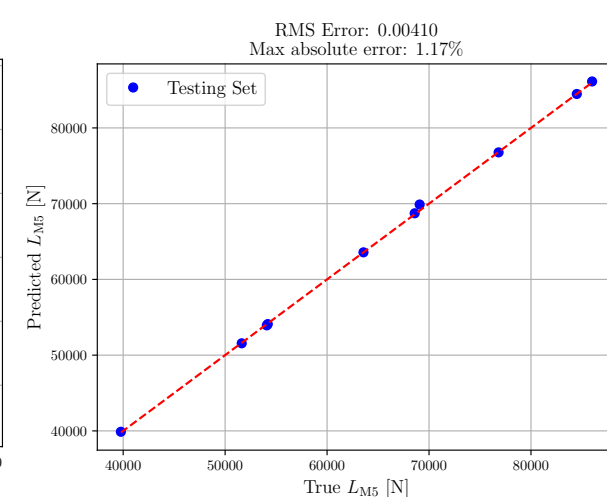
Where  $e_i$  is the error of the  $i$ th point in the testing set and  $n_{\text{test}}$  is the total number of points in the testing set.



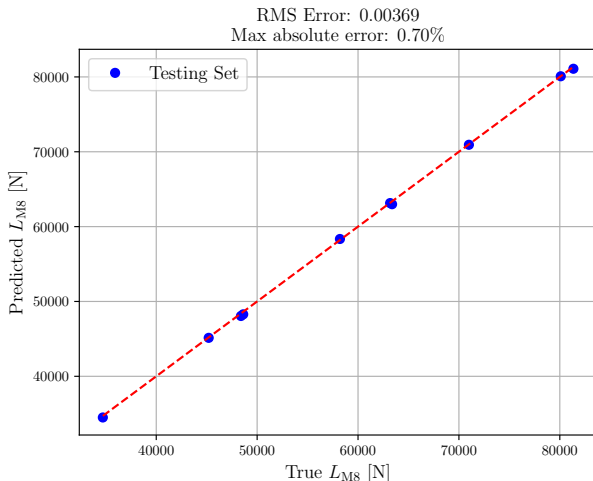
(a)



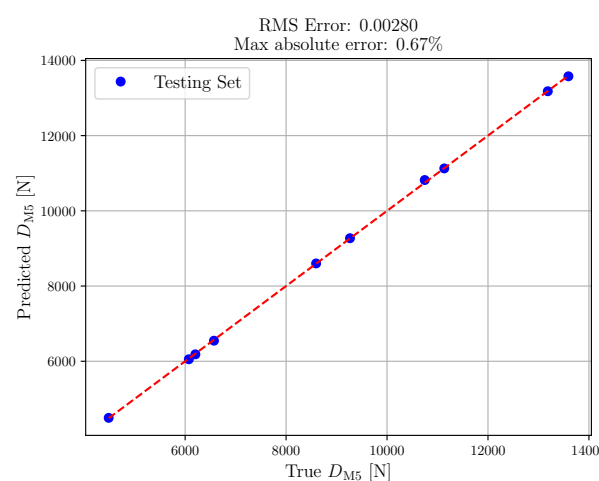
(b)



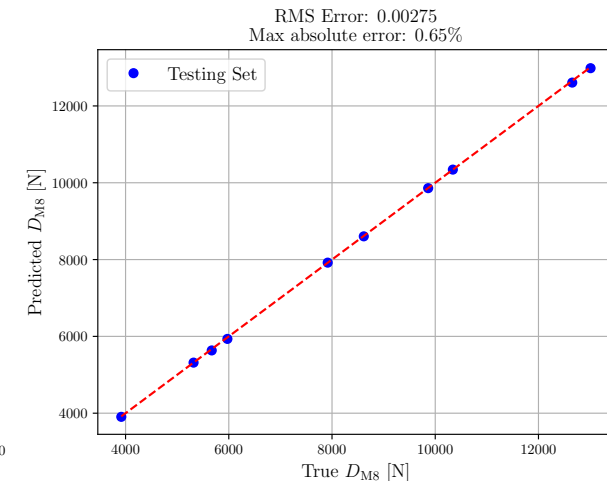
(c)



(d)



(e)



(f)

Figure 17: Cross-validation for the surrogate models of Volume (a),  $S_{\text{wet}}$  (b),  $L_{\text{M5}}$  (c),  $L_{\text{M8}}$  (d),  $D_{\text{M5}}$  (e) and  $D_{\text{M8}}$  (f)

## 2.6 Shape Optimisation

This section outlines the optimisation approach taken and the different cases considered. The implementation of the Genetic Algorithm (GA) used in the optimisation is first covered in Section 2.6.1. Single objective unconstrained test cases are then presented in Section 2.6.2, the objectives of these being to:

- evaluate the performance of the surrogate model and optimisation algorithm on simple cases.
- identify redundant optimisation objectives.

Five multi-objective optimisation cases are finally presented in Section 2.6.3.

Note that across the optimisation cases, the cost function may be normalised with respect to a reference value for easier comparison across these cases. These values are obtained as the averages across the database of samples and are summarised in Table 10:

Table 10: Reference values

Quantity	Description	Value [N]
$\bar{D}_{M5}$	Average Drag at M5	9600
$\bar{D}_{M8}$	Average Drag at M8	8951
$\bar{L}_{M5}$	Average Lift at M5	65996
$\bar{L}_{M8}$	Average Lift at M8	60866

### 2.6.1 Genetic Algorithm

Genetic algorithms (GA) [107], which mimic the process of natural selection, evolve a set of solutions over many generations. This makes them suitable for multi-objective problems with conflicting objectives, where a set of optimal trade-off solutions is more relevant than a single optimal solution. At every generation, “genetic” operations are applied on “parent” solutions to obtain new “off-spring” solutions based on their performance (fitness value). This allows for a thorough exploration of the design space.

The GA of the Python library PyGAD [108] was used in this work, owing to its flexibility and extensive documentation. It is worth noting that PyGAD maximises the solution, and so this may be reflected in the way the optimisation problems are tackled and presented hereafter.

Sections 2.6.1.1 and 2.6.1.2 outline the optimisation setup.

#### 2.6.1.1 Overall Setup

Table 11 summarises the main parameters of the GA for the Test Cases and Multi-objective Cases.

Table 11: Main parameters of the GA setup for both Test and Multi-objective cases

#	Parameter	Test Cases	Multi-obj. Cases
1	Runs	5	10
2	Generations	1000	2500
3	Parents Mating	40	80
4	Solutions per Population	70	120
5	Parent Selection Algorithm	Default	NSGA-II
6	Crossover Type	Uniform	Uniform

GAs are inherently random due to their stochastic processes. As such, the optimisation was run more than once to ensure robustness and consistency in the results. In multi-objective problems, after each run, the set of Pareto-optimal (non-dominated) solutions from the last generation was recorded. Once all the runs were performed, the set of non-dominated solutions across all runs was computed to give the final Pareto Front.

The choice was taken to increase parameters 2-4 for multi-objective cases to obtain a diverse and large set of solutions and promote convergence to the Pareto Front.

Furthermore, the popular Non-dominated Sorting Genetic Algorithm II (NSGA-II) [109], was selected for parent selection as it reflects the conflicting nature of the objectives and puts an emphasis on finding non-dominated solutions [110].

### 2.6.1.2 Constraint Evaluation

Given that GAs cannot directly evaluate constraints, it was decided to indirectly account for broken constraints via a penalty approach.

Firstly, to favor geometrically valid solutions, it was decided to attribute a fitness value of 0 whenever the Geometric Constraint (GC) is broken. This would prioritise valid solutions and minimise the number of non-valid solutions present at every generation.

Consider now an optimisation problem with  $m \in \mathbb{N}^*$  objectives and  $n \in \mathbb{N}^*$  inequality constraints. The constraints may be written as:

$$\underbrace{\begin{bmatrix} q_1(\mathbf{X}) \\ \dots \\ q_n(\mathbf{X}) \end{bmatrix}}_{\mathbf{Q}(\mathbf{X})} \geq \underbrace{\begin{bmatrix} k_1 \\ \dots \\ k_n \end{bmatrix}}_{\mathbf{K}} \quad (21)$$

Where  $q_1(\mathbf{X}) \dots q_n(\mathbf{X})$  are outputs of the design space and  $k_1 \dots k_n$  are constants.

The  $i$ th constraint is broken if  $g_i > 0$ , where  $g_i = k_i - q_i(\mathbf{X})$ . The absolute percentage by which it is broken can be computed as:

$$p_i = \left| \frac{g_i}{k_i} \right|, \quad i \in 1 \dots n \quad (22)$$

The  $j$ th objective's fitness/cost is then penalised as follows:

$$F_j = \frac{\bar{F}_j}{1 + 10 \cdot n_b \cdot \max([p_1, \dots, p_{n_b}])}, \quad j \in 1 \dots m \quad (23)$$

Where  $F_j$  is the penalised fitness,  $\bar{F}_j$  is the fitness before penalty and  $n_b$  is the total number of broken constraints.

In this way, the fitness is penalised based on how many constraints are broken as well as the extent to which these are broken. The factor of 10 was determined on a trial and error basis.

### 2.6.2 Test Cases

A total of 6 single objective optimisation test cases were explored. These are summarised in Table 12.

Table 12: Test cases considered

Test Case	Objective	Cost Function
1	Maximise Volume	$C = V$
2	Maximise $D_{M5}$	$C = D_{M5}/\bar{D}_{M5}$
3	Minimise Volume	$C = 1/V$
4	Minimise $D_{M5}$	$C = \frac{1}{D_{M5}/\bar{D}_{M5}}$
5	Minimise $L_{M5}$	$C = \frac{1}{L_{M5}/\bar{L}_{M5}}$
6	Maximise $L_{M5}$	$C = L_{M5}/\bar{L}_{M5}$

### 2.6.3 Multi-objective Optimisation Cases

Five multi-objective optimisation cases were considered in this study. For the reader's ease of understanding, these are described in Table 13 before being outlined technically in the following Sections 2.6.3.1 to 2.6.3.5.

Table 13: Description of the Multi-objective Cases

Case	Objectives	Constraints
1	Maximise Volume Minimise Inviscid Drag	None
2	Maximise Volumetric Efficiency Minimise Inviscid Drag	None
3	Maximise Volume Minimise Viscous Drag	None
4	Maximise Volume Minimise Inviscid Drag	Yes
5	Maximise Inviscid Lift Minimise Inviscid Drag	None

#### 2.6.3.1 Case 1

Case 1 may be presented as:

$$\text{Maximise } \begin{cases} V \\ 1/D_{\text{avg}} \end{cases}$$

where:

$$D_{\text{avg}} = \frac{0.5D_{M5} + 0.5D_{M8}}{0.5\bar{D}_{M5} + 0.5\bar{D}_{M8}} \quad (24)$$

#### 2.6.3.2 Case 2

Case 2 may be presented as:

$$\text{Maximise } \begin{cases} v_{\text{eff}} = V^{2/3}/S_{\text{wet}} \\ 1/D_{\text{avg}} \end{cases}$$

where  $D_{\text{avg}}$  is given as in Equation (24).

#### 2.6.3.3 Case 3

Case 3 may be presented as:

$$\text{Maximise } \begin{cases} V \\ 1/D_{\text{avg}}^{\text{visc}} \end{cases}$$

where:

$$D_{\text{avg}}^{\text{visc}} = \frac{0.5D_{M5}^{\text{visc}} + 0.5D_{M8}^{\text{visc}}}{0.5\bar{D}_{M5} + 0.5\bar{D}_{M8}} \quad (25)$$

And the superscript “visc” denotes a viscous estimate of drag. Estimates of the viscous contributions were obtained through corrections found in the work by Viola *et al.* [67], given as:

$$(\Delta C_D)_{\text{visc}} = 0.455 \cdot \frac{1}{\log_{10}(Re)^{2.58}} \cdot \frac{1}{(1 + 0.144M_\infty^2)^{0.65}} \cdot \frac{S_{\text{wet}}}{S_{\text{ref}}} \quad (26)$$

Where  $(\Delta C_D)_{\text{visc}}$  is the viscous contribution of the drag coefficient,  $Re$  is the Reynolds number and  $S_{\text{ref}}$  is a reference area.

The length  $l$  of the waverider was used in the calculation of the Reynolds number. The drag coefficient was then redimensionalised to estimate the viscous drag force.

#### 2.6.3.4 Case 4

Case 4 may be presented as:

$$\text{Maximise } \begin{cases} V \\ 1/D_{\text{avg}} \end{cases} \quad \text{with respect to } \begin{cases} L_{M5} \geq L_{\min} \\ L_{M8} \geq L_{\min} \\ D_{\text{avg}} \leq D_{\max} \end{cases}$$

where  $D_{\text{avg}}$  is given as in Equation (24),  $L_{\min} = 47000$  N and  $D_{\max} = 14000$  N.

#### 2.6.3.5 Case 5

Case 5 may be presented as:

$$\text{Maximise } \begin{cases} L_{\text{avg}} \\ 1/D_{\text{avg}} \end{cases}$$

where  $D_{\text{avg}}$  is given as in Equation (24) and:

$$L_{\text{avg}} = \frac{0.5L_{M5} + 0.5L_{M8}}{0.5\bar{L}_{M5} + 0.5\bar{L}_{M8}} \quad (27)$$

### 3 Results & Discussions

#### 3.1 CFD Verification

This section aims to verify the CFD setup against the reference inviscid flowfield. To this end, two waverider geometries from the database (see Appendix B) were chosen. Namely, Waveriders 10 and 65 were selected as their design Mach numbers are very close to M8 and M5 respectively. This means the flow characteristics can be compared to the analytical solution in both on and off-design conditions. The two waveriders' design properties are summarised in Table 14:

Table 14: Waveriders used for verification purposes

Index	$M_{\text{design}}$	X1	X2	X3	X4
65	5.078	0.234	0.290	0.356	0.467
10	7.907	0.264	0.082	0.337	0.794

To avoid confusion, these waveriders will be denoted as Waverider-M5 and Waverider-M8 in this section.

First, contours of pressure coefficient were plotted as seen from the symmetry plane, and this is shown in Figure 18. Throughout this work, the pressure coefficient is obtained as in Equation (28):

$$C_p = \frac{p - p_\infty}{0.5\rho_\infty U_\infty^2} \quad (28)$$

Such that a positive pressure coefficient represents an increase in static pressure from the freestream and vice versa.

For visualisation purposes, the waverider is represented in black with a white outline. Starting with Waverider-M5, as expected, the target shockwave angle ( $15^\circ$ ) is reached at M5. In off-design conditions at M8,  $\beta_0 \approx 11^\circ$  which matches  $\beta_0 \approx 10.96^\circ$  predicted by the  $\beta - \theta - M$  relation for  $M_{\text{design}} = 5.078$ . Similarly, the target angle is reached at M8 for Waverider-M8. In off-design conditions at M5,  $\beta_0 \approx 19^\circ$  which matches  $\beta_0 \approx 18.82^\circ$  predicted by the  $\beta - \theta - M$  relation for  $M_{\text{design}} = 7.907$ .

The shape of the Shockwave Curve (SC) in design conditions was then compared to the design SC. This can be seen in Figure 19, where the SC is visualised via Schlieren imaging. For both geometries, there is very good agreement between the CFD results and the expected SC.

Overall, Figures 18 and 19 clearly demonstrate that the CFD setup correctly solves the inviscid flowfield and that it can be trusted to provide reasonably accurate estimates of inviscid flow quantities.

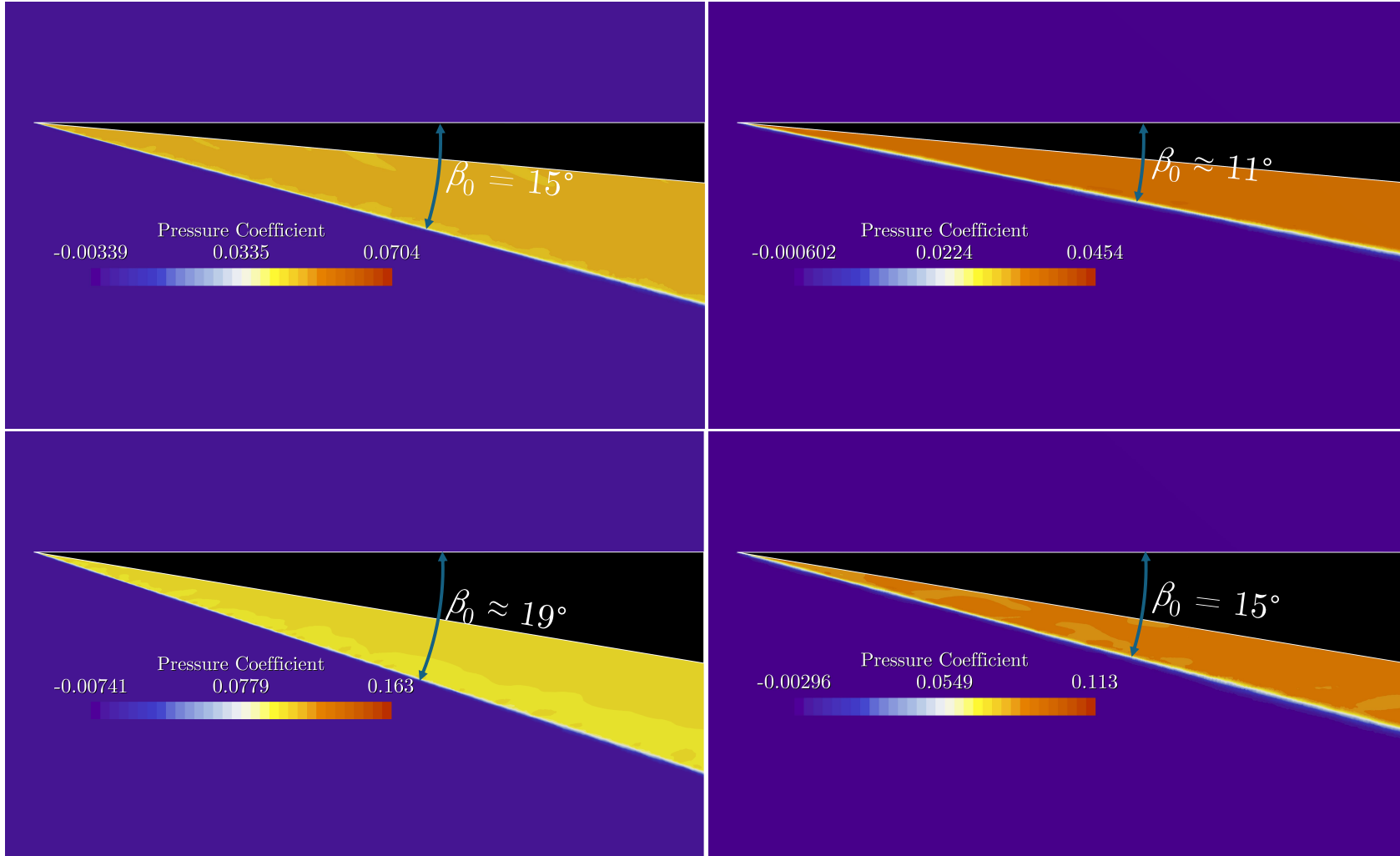


Figure 18: Contour plot of pressure coefficient for Waverider-M5 (top) and Waverider-M8 (bottom) at M5 (left) and M8 (right) as viewed from the Symmetry Plane

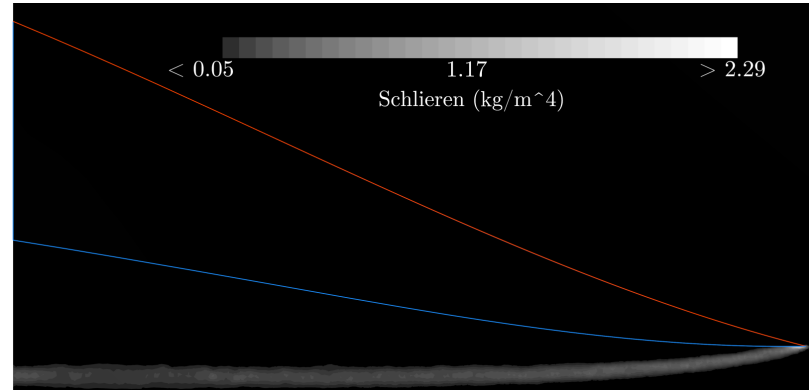
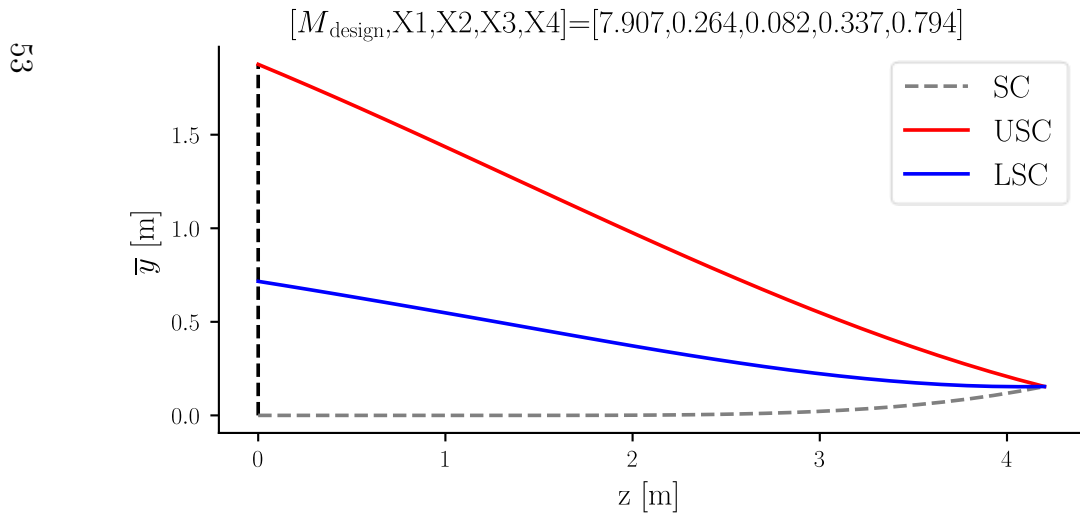
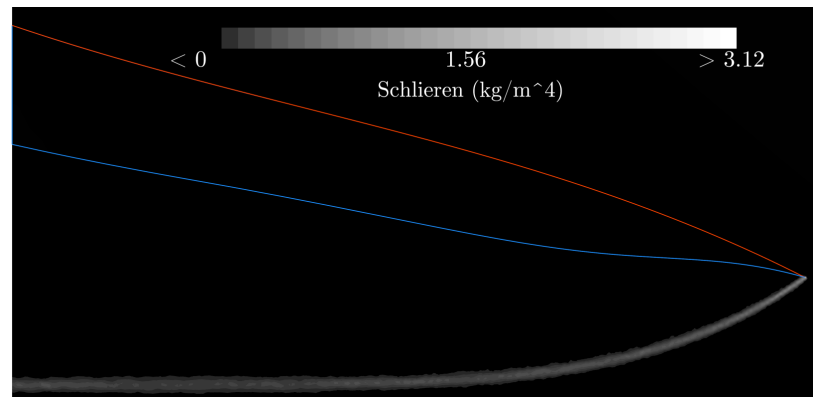
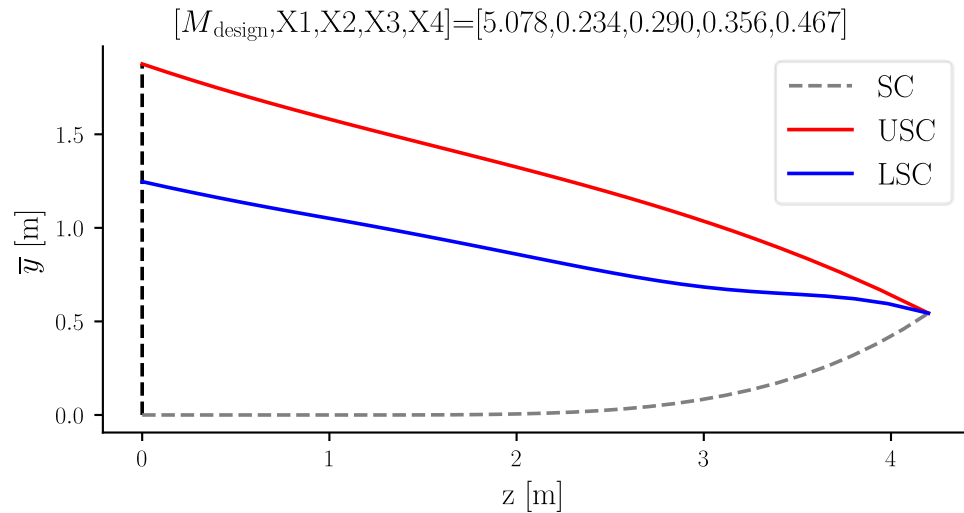


Figure 19: Shockwave shape on the Base Plane for Waverider-M5 (top) and Waverider-M8 (bottom). Left shows the design SC while the right shows the SC obtained through inviscid CFD in design conditions. Visualised via digital Schlieren imaging.

## 3.2 Design Space Analysis

### 3.2.1 Main Trends

The main trends concerning the outputs of the design space were identified and plotted in Figure 20 below.

As seen in Figure 20a, the lift to drag ratio does not vary much between M5 and M8. Nevertheless, a small decrease is typically observed at M8 compared to M5. On the other hand, the lift and the drag both decrease from M5 to M8. Given  $L/D$  stays relatively constant, this indicates that lift and drag both decrease by a similar percentage.

Moreover, as expected, an increase in volume tends to result in an increase in lift and drag, the relationship appearing almost linear. An increase in volume also tends to correspond to an increase in volumetric efficiency ; however, the relationship is not as clear as with lift and drag.

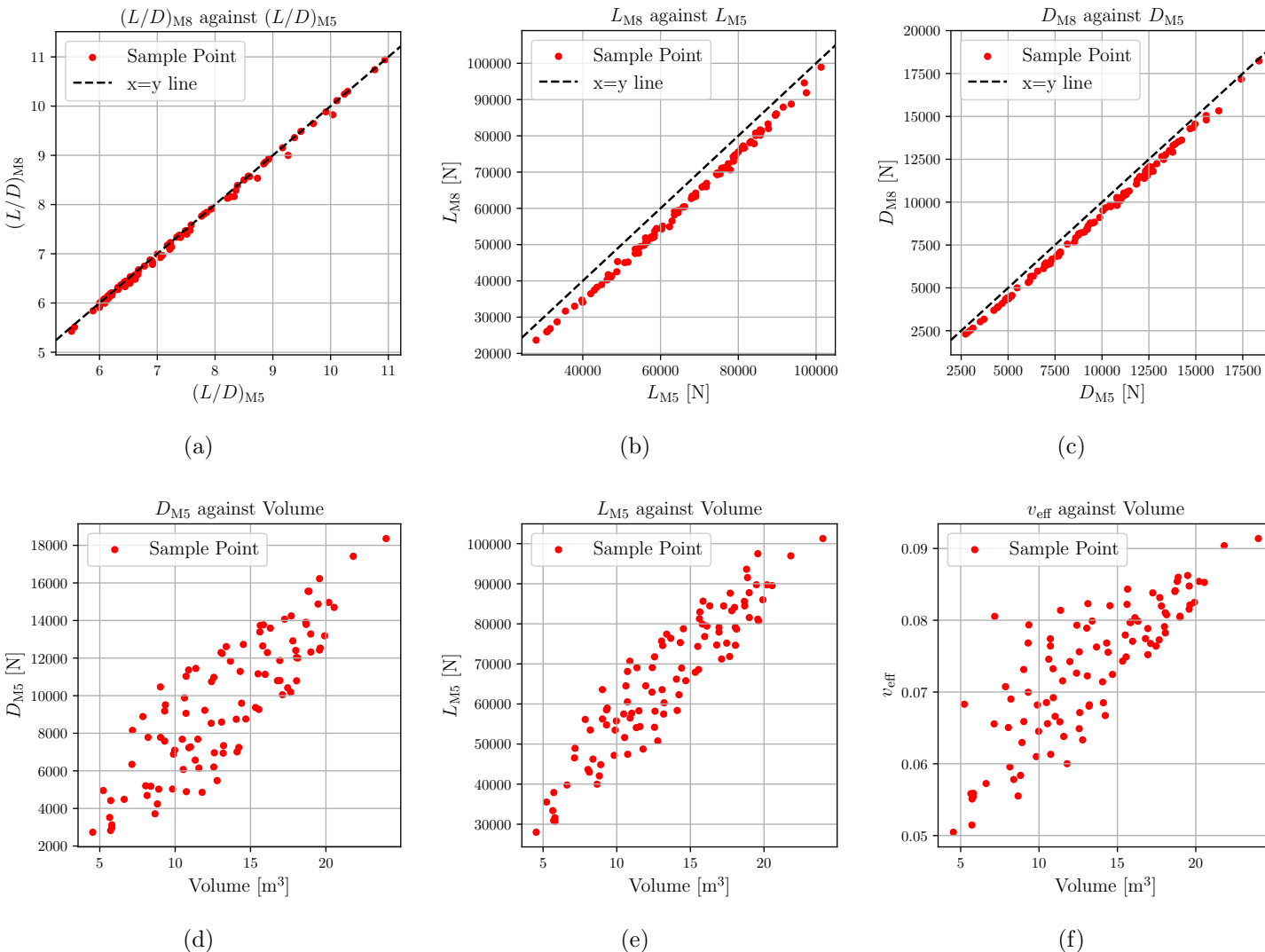


Figure 20:  $(L/D)_{M5}$  against  $(L/D)_{M8}$  (a),  $L_{M5}$  against  $L_{M8}$  (b),  $D_{M5}$  against  $D_{M8}$  (c), Volume against  $D_{M5}$  (d), Volume against  $L_{M5}$  (e)

### 3.2.2 Feature Importances

Son *et al.* [16] made use of Analysis of Variance (ANOVA) to determine the influence of the inputs on the outputs of the design space. However, ANOVA assumes independence between the design variables. As demonstrated in Section 2.3.5, interdependencies do exist between the design variables, and this can lead to inaccuracies in the outcome of ANOVA. In this work, another approach was taken by training Random Forest Models (RFMs) and extracting the Feature Importances. In a RFM, the importance of a feature directly reflects how crucial this feature is in correctly predicting the output, as it is calculated based on the feature’s contribution to minimising error across the ensemble of decision trees [111]. Moreover, RFMs do not assume Independence and are able to model complex relationships, making them a more suitable and flexible alternative to ANOVA. These models were trained solely for this purpose via the Scikit-learn Python package [103] with 1000 trees.

The feature importances are shown below in Figure 21. Each output is then plotted against its dominant feature in Figure 22. Here, it was deemed sufficient to analyse  $L/D$ ,  $D$  and  $L$  at M5 solely, as the relationship between these properties at M5 and M8 have been identified and discussed in the previous section.

Starting with  $(L/D)_{M5}$  (Figure 21a), it is clearly dominated by  $M_{\text{design}}$  with the other variables playing little to no importance in determining the ratio. Figure 22a confirms this, as an increase in  $M_{\text{design}}$  generally leads to a decrease in  $(L/D)_{M5}$ . The relationship is non-linear and appears to “cap” the maximum lift to drag ratio achievable as a function of  $M_{\text{design}}$ .

Similarly,  $L_{M5}$  and  $D_{M5}$  (Figures 21b and 21c) are mainly driven by  $M_{\text{design}}$ . From Figure 22, an increase in  $M_{\text{design}}$  generally leads to an increase in both parameters. However, the geometric parameters have gained more importance than with  $(L/D)_{M5}$ , especially in the prediction of lift. Furthermore, in the paper by Son *et al.* [16, Figure 10], X3 has significantly more influence on lift and drag compared to X4. Here, their importances are similar, and this may be a result of one, or a combination of, the following:

- Larger number of samples.
- Introduction of  $M_{\text{design}}$  to the design space.
- Use of a RFM instead of ANOVA.

When it comes to Volume (Figure 21d), X2 has the most influence on the output and this is similar to the findings of Son *et al.* [16]. This is because X2 controls the curvature of the SC, which determines the location of the center of the local osculating cone and therefore influences the flowfield the most [16]. As seen in Figure 22d, a higher value of X2 tends to result in a higher volume. This is in line with the findings of Son *et al.* [16] where the maximum volume waveriders found in the optimisation neared X2 = 1. Moreover, X3 is more important than X4, which is the opposite in [16]. Once again, this may be attributed to one of the reasons mentioned above.

Overall, the introduction of  $M_{\text{design}}$  to the design space reveals the major role it plays in determining key aerodynamic properties like  $L/D$ , lift and drag. This is because, for a combination X1...X4 (i.e specific shockwave and upper surface shapes),  $M_{\text{design}}$  determines the upper and lower bounds of volume. Indeed, as mentioned in Section 2.3.4.1, an

increase in  $M_{\text{design}}$  results in an increase in the deflection angle, which increases overall volume. With this in mind, the trade-off relationships between lift/drag and volume, identified in the previous section, explain why lift and drag tend to increase with  $M_{\text{design}}$ .

Furthermore, it can be seen in Figure 22 that, as  $M_{\text{design}}$  increases, the range of lift and drag also appears to increase (i.e the difference between the maximum and minimum values). For a given  $M_{\text{design}}$ , the minimum volume waverider is obtained when:

$$\mathbf{X} = [M_{\text{design}}, X_1, X_2, X_3, X_4] = [M_{\text{design}}, 0, 0, 1, 1]$$

Which corresponds to a flat Shockwave Curve (SC) with the lowest possible Upper Surface Curve (USC). On the other hand, the maximum volume waverider is obtained when:

$$\mathbf{X} = [M_{\text{design}}, X_1, X_2, X_3, X_4] = [M_{\text{design}}, X_{1\text{crit}}, 1, 0, 0]$$

Which corresponds to a SC with maximum curvature, flat USC and maximum flat section in the SC. The minimum and maximum volumes were recorded for three values of  $M_{\text{design}}$  and this is shown in Table 15.  $\Delta V$  denotes the difference between the maximum and minimum.

Table 15: Maximum and minimum values of volume for three design mach numbers

$M_{\text{design}}$	$V_{\min}$ [ $\text{m}^3$ ]	$V_{\max}$ [ $\text{m}^3$ ]	$\Delta V$ [ $\text{m}^3$ ]
5.0	2.54	13.31	10.68
6.5	4.11	21.02	16.91
8.0	4.91	24.90	19.99

Table 15 highlights the increase in  $\Delta V$  with  $M_{\text{design}}$ . Therefore, this explains why the plots of lift and drag against  $M_{\text{design}}$  appear to “widen” with an increase in design Mach number.

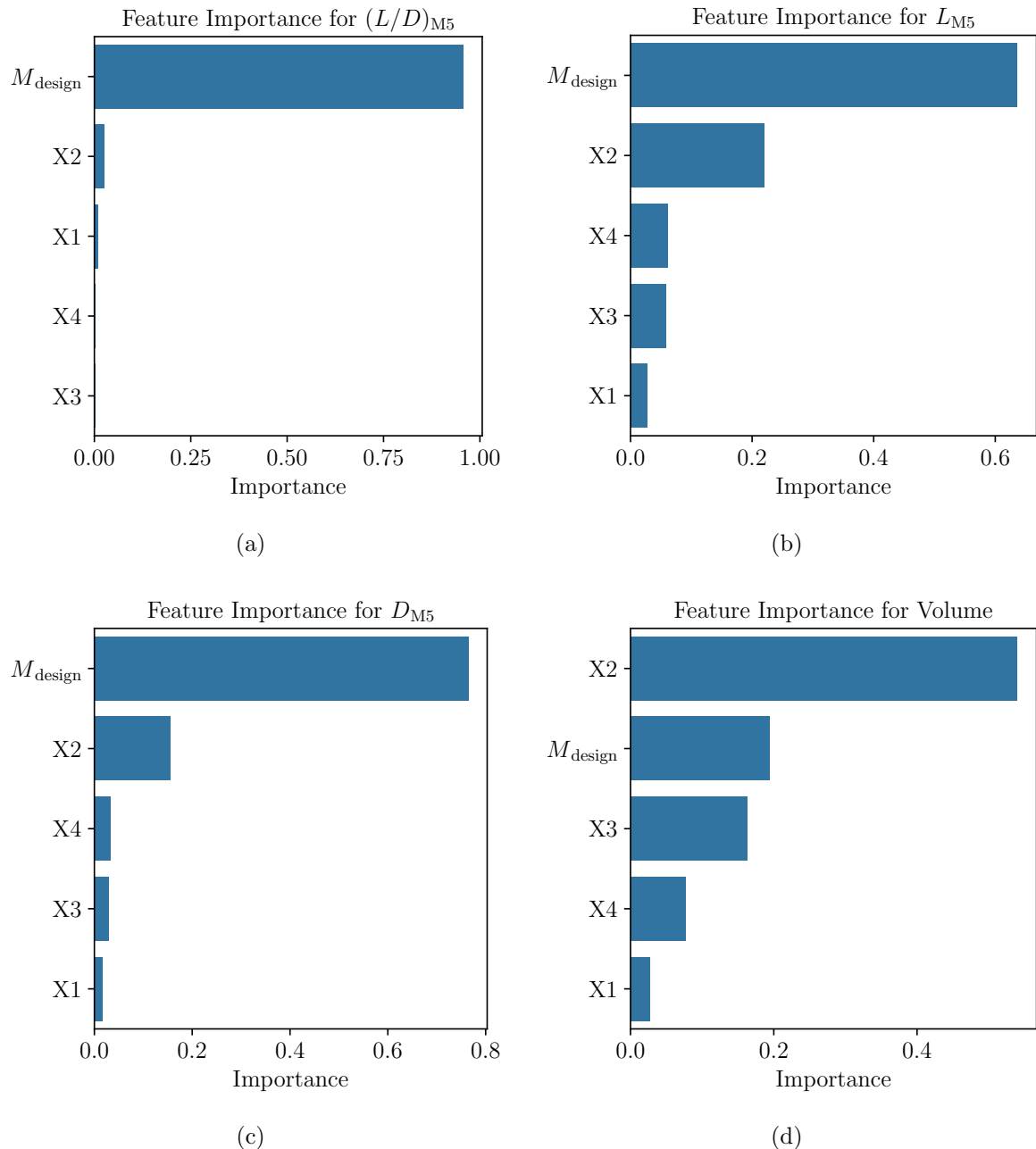


Figure 21: Feature importances for  $(L/D)_{M5}$  (a),  $L_{M5}$  (b),  $D_{M5}$  (c) and Volume (d)

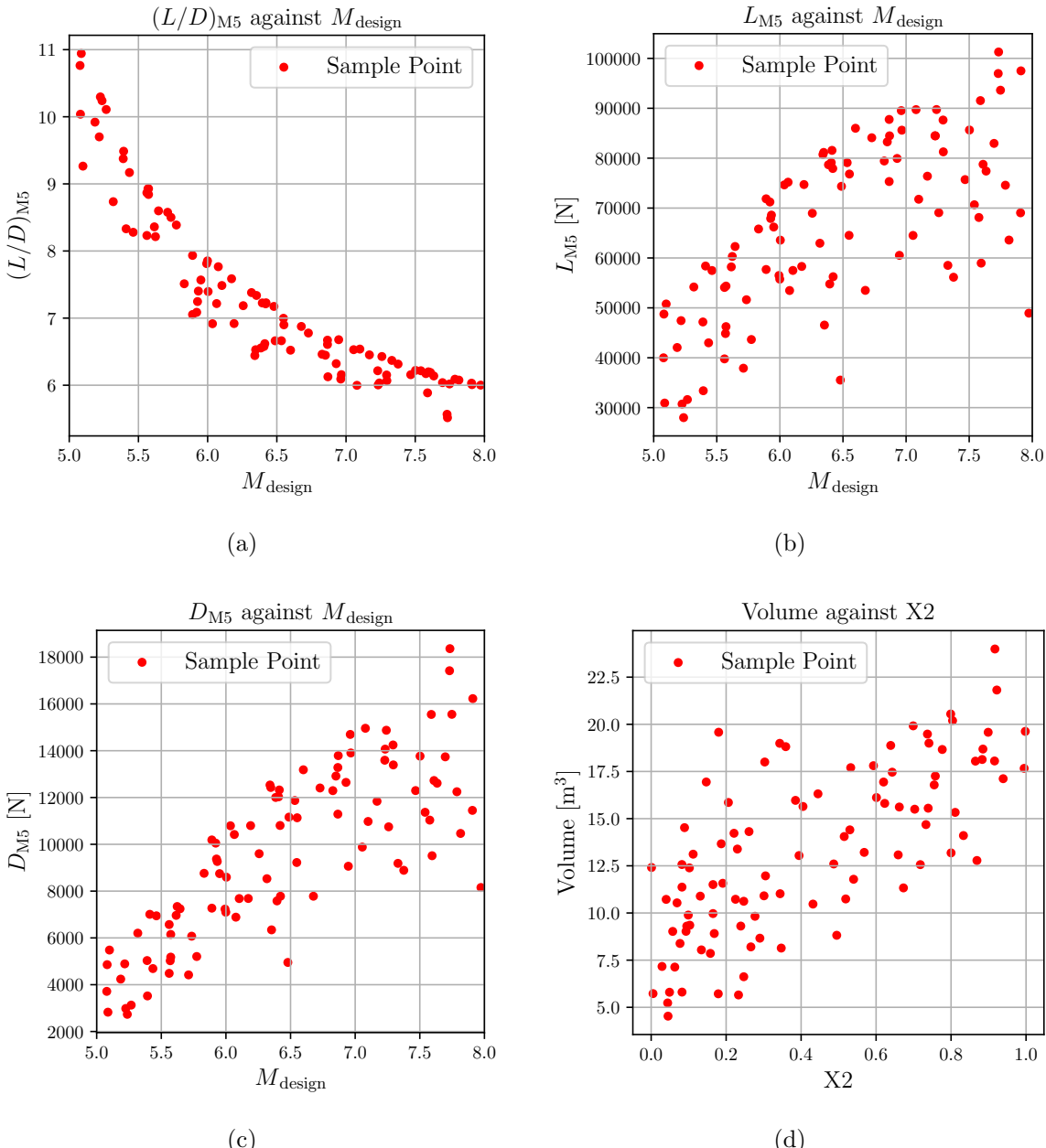


Figure 22:  $(L/D)_{M5}$  (a),  $L_{M5}$  (b),  $D_{M5}$  (c) and Volume (d) against their most important features

### 3.3 Shape Optimisation

#### 3.3.1 Test Cases

The results of the optimisation test cases are summarised in Table 16. Here, the surrogate prediction and the true value are based on the chosen cost functions (see Section 2.6.2). In cases where the objective is to minimise, the inverse of the cost function was taken to yield the original quantities of interest. The cases were divided based on the common optimum reached.

Table 16: Results of the test cases

Test Case	Objective	Run	Optimum					Surrogate Prediction	True Value	% Abs. Error	Units
			M <sub>design</sub>	X1	X2	X3	X4				
1	Maximise Volume	1	8.000	0.202	1.000	0.000	0.014	24.970	24.885	0.344	$\text{m}^3$
		2	8.000	0.212	0.952	0.000	0.000	24.942		0.230	
		3	8.000	0.203	0.999	0.000	0.003	24.971		0.348	
		4	7.999	0.205	0.986	0.000	0.000	24.962		0.311	
		5	8.000	0.202	0.999	0.000	0.000	24.968		0.334	
2	Maximise Drag	1	8.000	0.202	0.999	0.000	0.022	2.033	1.964	3.525	-
		2	8.000	0.201	1.000	0.297	0.000	2.034		3.591	
		3	8.000	0.204	0.990	0.100	0.000	2.032		3.450	
		4	7.999	0.202	1.000	0.299	0.000	2.034		3.587	
		5	8.000	0.202	0.999	0.276	0.000	2.034		3.575	
3	Minimise Volume	1	5.001	0.205	0.000	0.994	1.000	2.565	2.541	0.934	$\text{m}^3$
		2	5.001	0.212	0.000	0.998	0.996	2.562		0.795	
		3	5.001	0.205	0.000	0.996	0.999	2.561		0.760	
		4	5.001	0.206	0.000	0.998	0.998	2.558		0.650	
		5	5.003	0.207	0.000	0.999	0.997	2.560		0.713	
4	Minimise Drag	1	5.002	0.997	0.000	0.997	0.996	0.128	NA	NA	-
		2	5.001	0.966	0.000	0.999	1.000	0.127		NA	
		3	5.001	0.999	0.000	0.998	0.995	0.128		NA	
		4	5.001	0.997	0.000	0.997	0.996	0.127		NA	
		5	5.001	0.998	0.000	0.993	1.000	0.127		NA	
5	Minimise Lift	1	5.001	0.966	0.000	0.997	0.999	0.214	NA	NA	-
		2	5.000	1.000	0.000	0.999	0.998	0.214		NA	
		3	5.000	0.997	0.000	0.999	0.998	0.214		NA	
		4	5.003	0.999	0.000	0.997	1.000	0.214		NA	
		5	5.002	0.974	0.000	0.999	0.999	0.214		NA	
6	Maximise Lift	1	7.992	0.350	0.428	0.000	0.000	1.645	1.640	0.283	-
		2	7.998	0.370	0.390	0.000	0.000	1.647		0.413	
		3	8.000	0.340	0.463	0.000	0.000	1.645		0.310	
		4	7.998	0.370	0.372	0.000	0.000	1.646		0.360	
		5	7.996	0.356	0.424	0.000	0.000	1.646		0.365	

As expected from the trade-off relationship identified in the design space analysis (Section 3.2), maximising Volume is equivalent to maximising drag. However, lift was also identified to increase with volume. Despite this, maximising lift resulted in a unique optimum. In a similar light, minimising volume is equivalent to minimising both lift and drag.

The optimum reached by test cases 1 and 2 is the expected solution for maximum volume (see previous section):

$$\mathbf{X} = [M_{\text{design}}, X_1, X_2, X_3, X_4] = [8, X_{1\text{crit}}, 1, 0, 0]$$

For volume, the surrogate prediction is very accurate with an error below 1% at every run. For drag, the error is higher at approximately 3.5%.

Looking at cases 3-4-5, the optimum reached is the expected solution for minimum volume (see previous section):

$$\mathbf{X} = [M_{\text{design}}, X_1, X_2, X_3, X_4] = [5, 0, 0, 1, 1]$$

For volume, the surrogate is, once again, very accurate with an error below 1% at every run. Unfortunately, estimating lift and drag was not possible for this waverider as its thickness tends to 0 at its lateral extremities, and this caused meshing issues during the CFD process.

Finally, case 6 reached a unique and unexpected optimum for lift maximisation. The values of X1 and X2 vary slightly between runs. Therefore, the average solution was taken

and an estimate of lift was obtained from it. As shown, the predictions are accurate to the second decimal place. This unexpected optimum demonstrates the surrogate's success in modelling the relationship between the input and output spaces.

Overall, the optimisation setup's ability to successfully reach both known and unknown solutions with high accuracy has been demonstrated by these test cases. As a consequence, the results obtained from multi-objective optimisation can be assumed robust and reliable.

In comparison to the reference paper by Son *et al.* [16, p. 13], the surrogate models are far more accurate in their prediction of aerodynamic quantities, and this is demonstrated both by these results and the correlation plots included in Section 2.5.2.

The geometries corresponding to the three optima are shown in Figure 23.

62

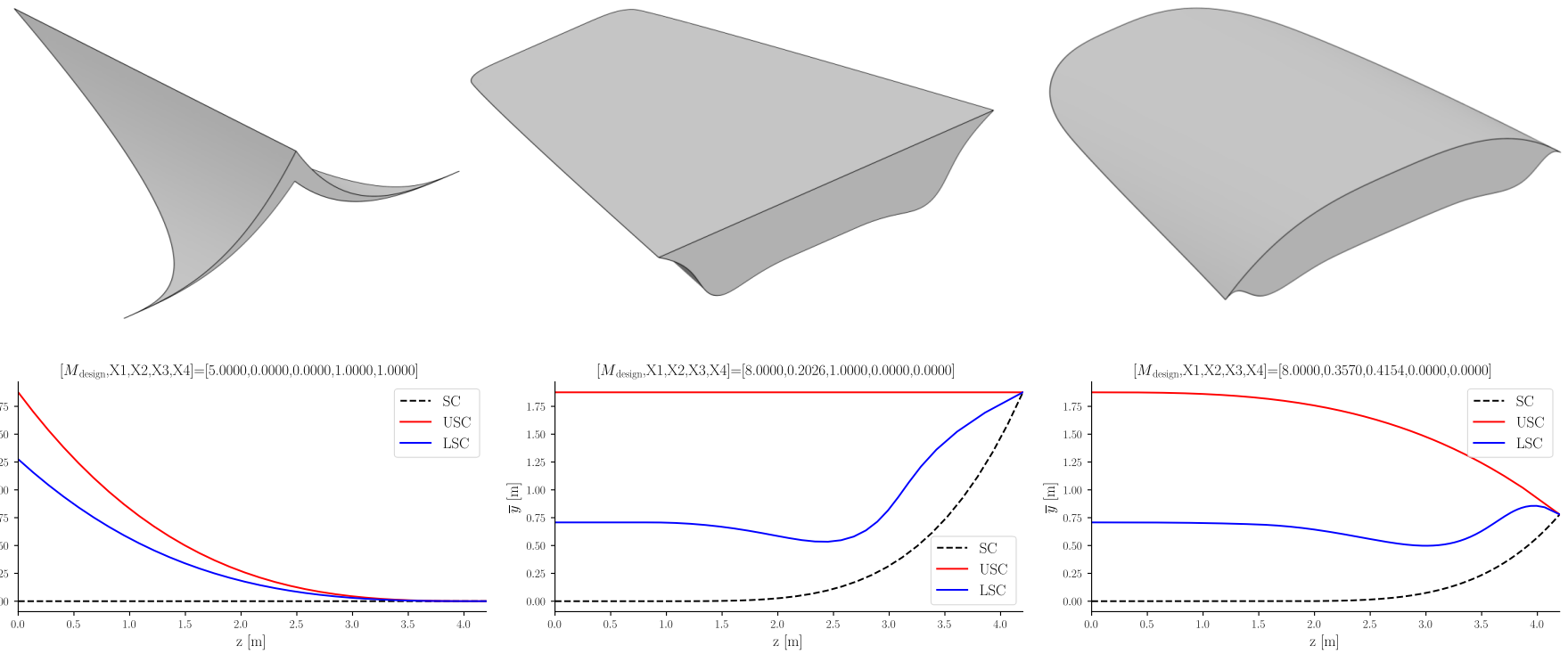


Figure 23: 3D view of the three optima reached in the test cases (top) along with a plot of the base plane (bottom). Minimum volume (left), maximum volume (middle) and maximum lift (right)

### 3.3.2 Multi-objective Cases

This section presents the results of the multi-objective optimisation cases. Here, as in the previous section, “Drag Fitness” refers to the inverse of the relevant cost function to yield the drag value itself. Given that all the drag-related cost functions have been normalised by the same quantity, the drag quantity can be compared across multiple cases with ease.

In each case, a representative Pareto Front is obtained after applying the K-Means clustering algorithm. With the exception of Case 2, the reader is referred to Appendix A for plots of the full Pareto Fronts.

#### 3.3.2.1 Results from Cases 1 & 4

##### 3.3.2.1.1 Case 1

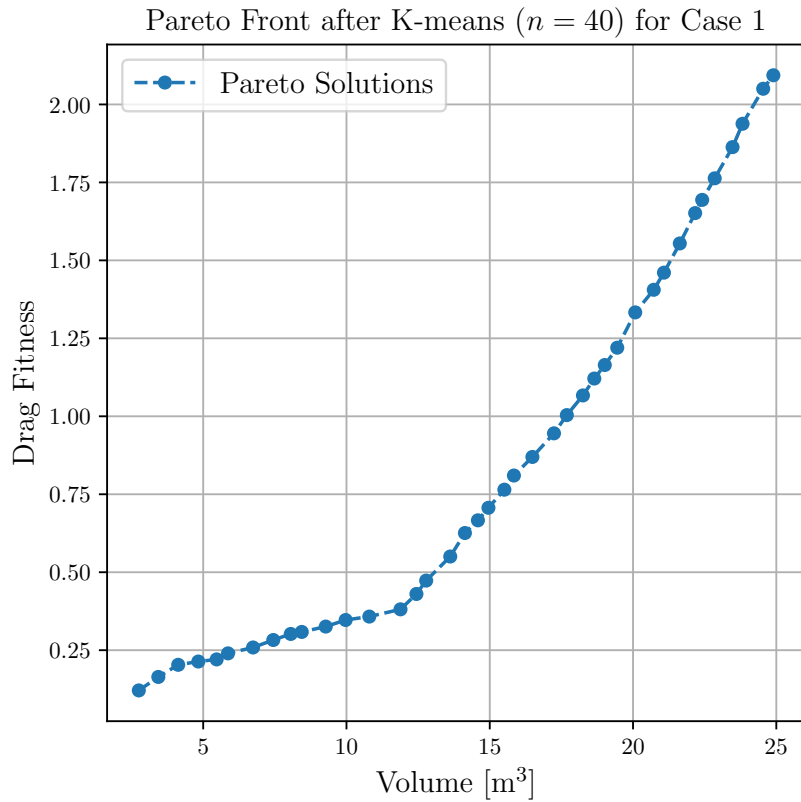


Figure 24: Representative Pareto Front for Case 1

Case 1’s representative Pareto Front is shown in Figure 24. As expected, there is a clear trade-off relationship between volume and drag. In the Pareto Front obtained by Son *et al.* [16, Figure 12], the trade-off relationship is non-linear. Here, the relationship between the two appears linear. Indeed, two linear regions can be identified from the plot. The first one spans from minimum volume to  $V \approx 12.5 \text{ m}^3$ , while the second spans from  $V \approx 12.5 \text{ m}^3$  to maximum volume. The slope of the curve increases between the two regions. For simplicity, these will be referred to as the first and second intervals hereafter.

The change in  $M_{\text{design}}$ ,  $(L/D)_{M5}$  and  $v_{\text{eff}}$  along the Pareto Front is plotted in Figure 25.

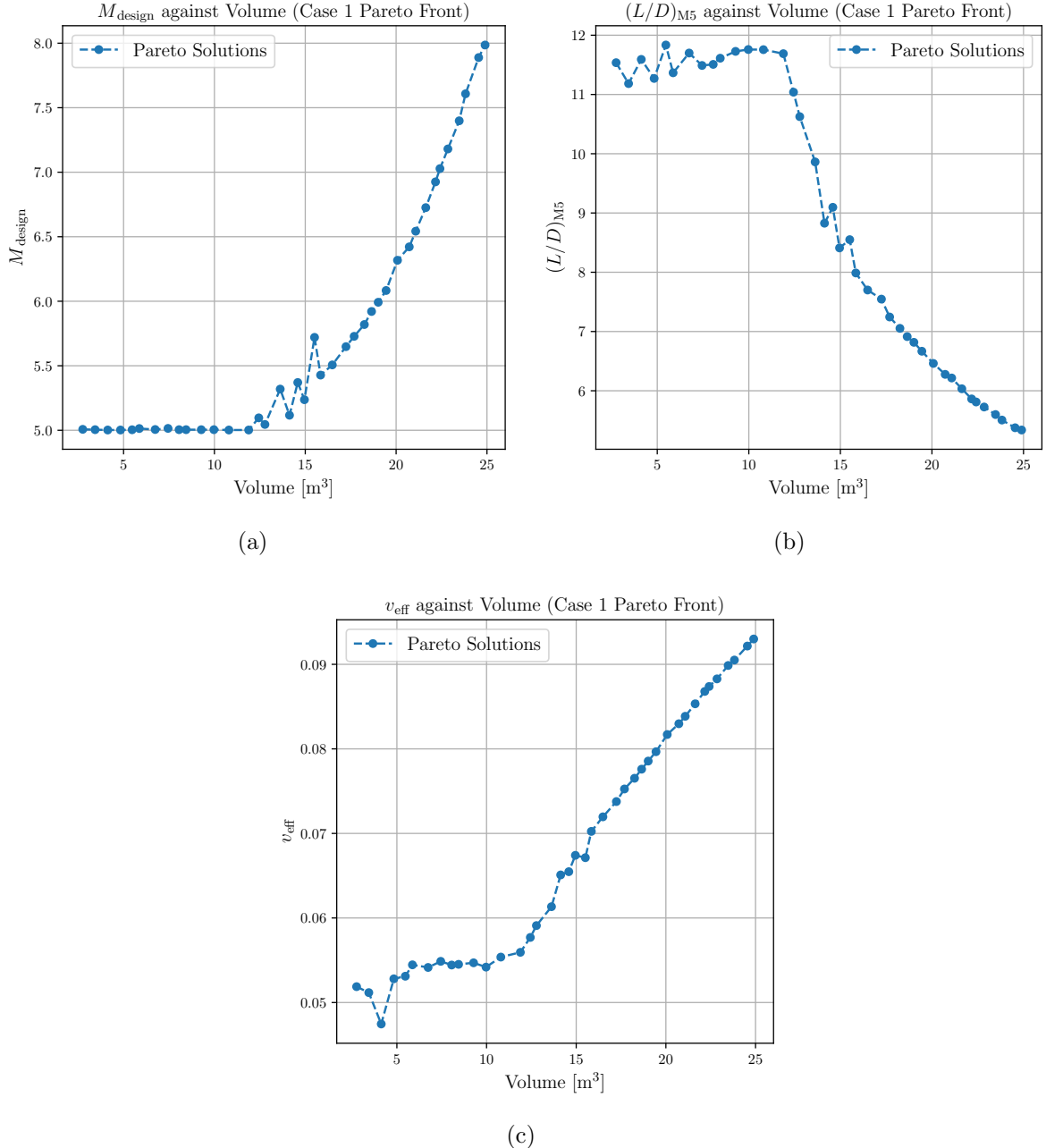


Figure 25: Variation of  $M_{\text{design}}$  (a),  $(L/D)_{M5}$  (b) and  $v_{\text{eff}}$  (c) across the Case 1 Pareto Front

Following on from the above, it can be seen that in the first interval,  $M_{\text{design}}$  (Figure 25a) remains more or less constant around 5. Then, it oscillates slightly until it starts stably increasing throughout the second interval. Similarly,  $(L/D)_{M5}$  (Figure 25b) remains more or less constant throughout the first interval until a sharp drop occurs at the second interval. Similar behaviour is observed with the volumetric efficiency (Figure 25c). This indicates that these two “parts” of the Pareto Front are visible through multiple outputs of the design space.

Figure 26 shows the behaviour of X1 and X2 across the Pareto Front.

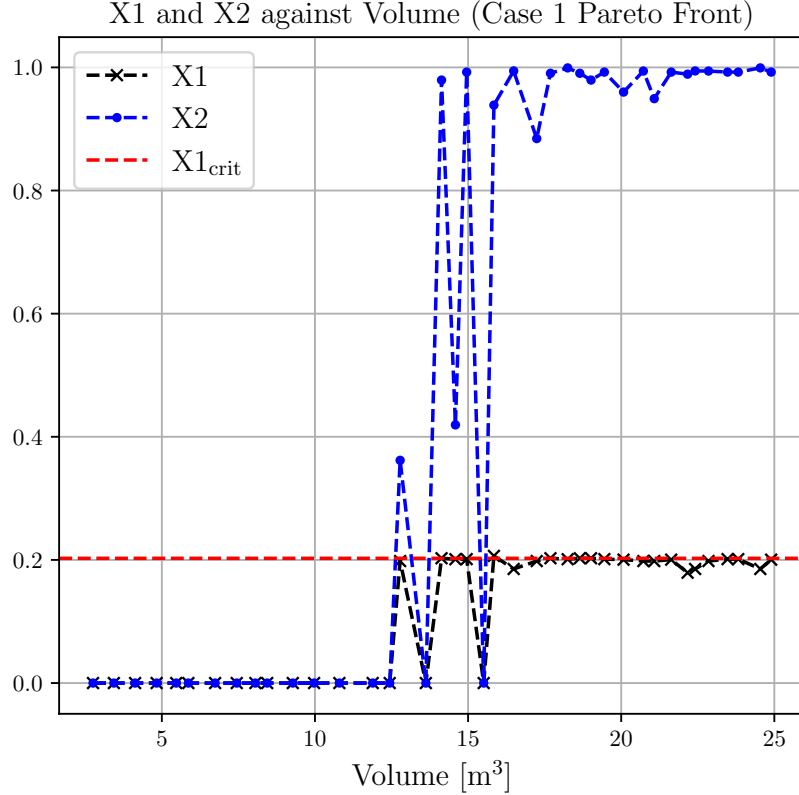


Figure 26: Variation of X1 and X2 across the Case 1 Pareto Front

As can be seen in Figure 26, the overall behaviour of X1 and X2 resembles that of  $M_{\text{design}}$ . During the first interval, both variables are zero, which corresponds to waveriders with a flat Shockwave Curve (SC). Then, a buffer/transition zone takes place until the variables stabilise into the second interval. In this second part, X2 tends towards its maximum value of 1 while X1 stabilises around  $X1_{\text{crit}}$ . When X2 reaches its maximum value,  $X1_{\text{crit}}$  is the maximum value X1 can take according to the Geometric Constraint (GC). For a given  $M_{\text{design}}$ , this configuration also represents the maximum volume waverider, as has been shown in Section 3.2.2. Along with the previous discussions, this further confirms the findings that:

- The Pareto Front for Case 1 is divided into two main linear regions. In the first region, the increase in drag is less steep than in the second.
- In the first region,  $M_{\text{design}} \approx 5$  and a flat SC is favored. Furthermore,  $(L/D)_{M5}$  and  $v_{\text{eff}}$  do not vary much.
- In the second region, the maximum volume configuration for a given  $M_{\text{design}}$  is favored. Additionally,  $M_{\text{design}}$  and  $v_{\text{eff}}$  increase rapidly while  $(L/D)_{M5}$  decreases rapidly.

Furthermore, this division in the Pareto Front shows that, in the first section, the increase in volume is provided by a change in the shape of the Upper Surface Curve (USC) - given that the SC is flat and  $M_{\text{design}}$  is constant. On the other hand, in the second section the increase in volume is provided purely by an increase in  $M_{\text{design}}$ . With regards to the Pareto Front, this indicates that the flat SC configuration can provide a sufficient increase

in volume early on and maintain a low drag. However, at some point a steep increase in drag becomes inevitable if an increase in volume is to be achieved and so the solution then shifts to the second section of the Pareto Front with the increase in  $M_{\text{design}}$ .

It's also worth addressing the behavior of the volumetric efficiency along the Pareto Front. Indeed, the increase in volumetric efficiency is only possible if volume increases while  $S_{\text{wet}}$  remains constant or decreases, as per its definition in Section 2.3.6. Given the sharp increase in  $v_{\text{eff}}$  in the second part of the Pareto Front (Figure 25c), this means the increase in  $M_{\text{design}}$  causes  $S_{\text{wet}}$  to either remain constant or decrease with volume. The wetted surface areas of three waveriders from the second part of the Pareto Front were recorded and displayed in Table 17.

Table 17: Wetted surface area of three waveriders with varying  $M_{\text{design}}$

$M_{\text{design}}$	$S_{\text{wet}} [\text{m}^2]$
5.0	89.00
6.5	91.24
8.0	91.79

Table 17 shows that  $S_{\text{wet}}$  remains almost constant with an increase in  $M_{\text{design}}$ . As a consequence, for a given  $X_1 \dots X_4$ , increasing  $M_{\text{design}}$  increases volume and volumetric efficiency without affecting the wetted surface area. Therefore, this explains the increase in volumetric efficiency in the second interval of the Pareto Front.

A clear drawback of the introduction of  $M_{\text{design}}$  into the design space can be identified from Case 1, which is the lack of variety in the shapes obtained. Indeed, only two “types” of waveriders were obtained. Son *et al.* [16, Figure 12] fixed the design Mach number and performed optimisation only through the geometric parameters  $X_1 \dots X_4$ . Their Pareto Front is shown in Figure 27.

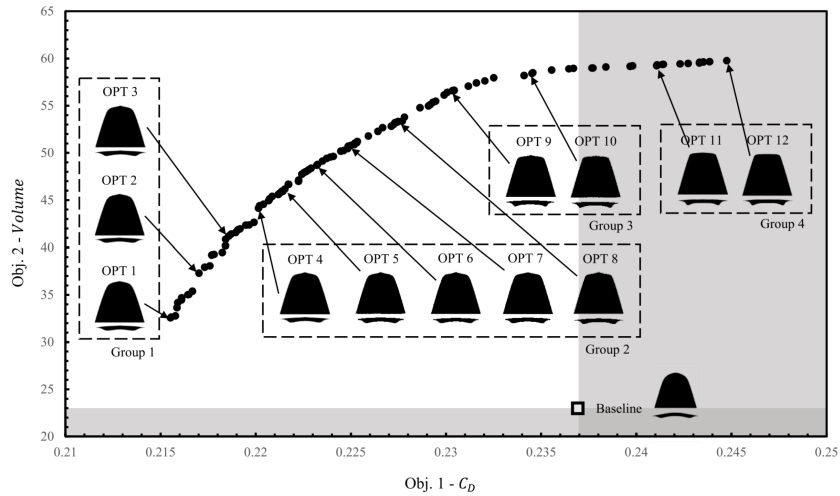


Figure 27: Pareto Front from Son *et al.* [16]

As can be seen in Figure 27, the shapes obtained progressively change through the Pareto Front. Therefore, introducing  $M_{\text{design}}$  may prevent such a diverse set of solutions from

being reached. This is likely because, as has been clearly shown, an increase in volume can also be obtained via  $M_{\text{design}}$ . Whereas, when  $M_{\text{design}}$  is constant, the increase in Volume can only be achieved via the manipulation of the geometric parameters, yielding a Pareto Front like Son *et. al's* [16].

### 3.3.2.1.2 Case 4

Case 4 is the “constrained” version of Case 1. Therefore, it was decided to discuss it together with Case 1. The representative Pareto Front of Case 4 is shown in Figure 28.

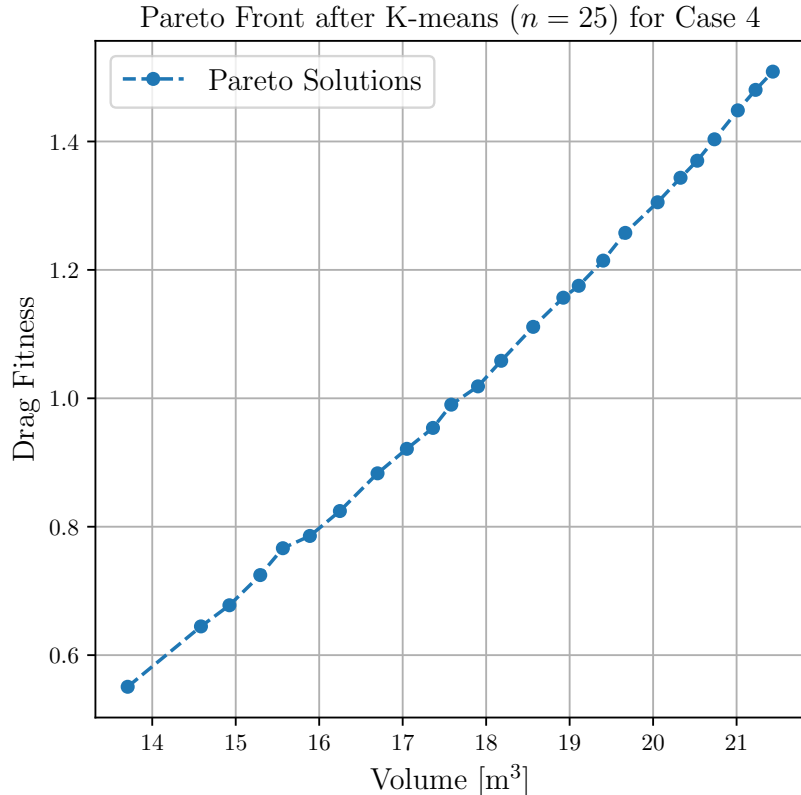


Figure 28: Representative Pareto Front for Case 4

Given the relationship between lift, drag and volume, it is expected that the constraints imposed in this case (see Section 2.6.3.4) restrict the Pareto Front of Case 4 to a portion of the unconstrained Pareto Front obtained in Case 1.

Looking at Figure 28, it is indeed the case as the bounds of volume and drag are reduced in comparison to Case 1. Furthermore, the Pareto Front obtained resembles the second linear portion of Case 1's Pareto Front. This shows the penalty approach implemented successfully constrained the Pareto Front.

### 3.3.2.2 Results from Case 2

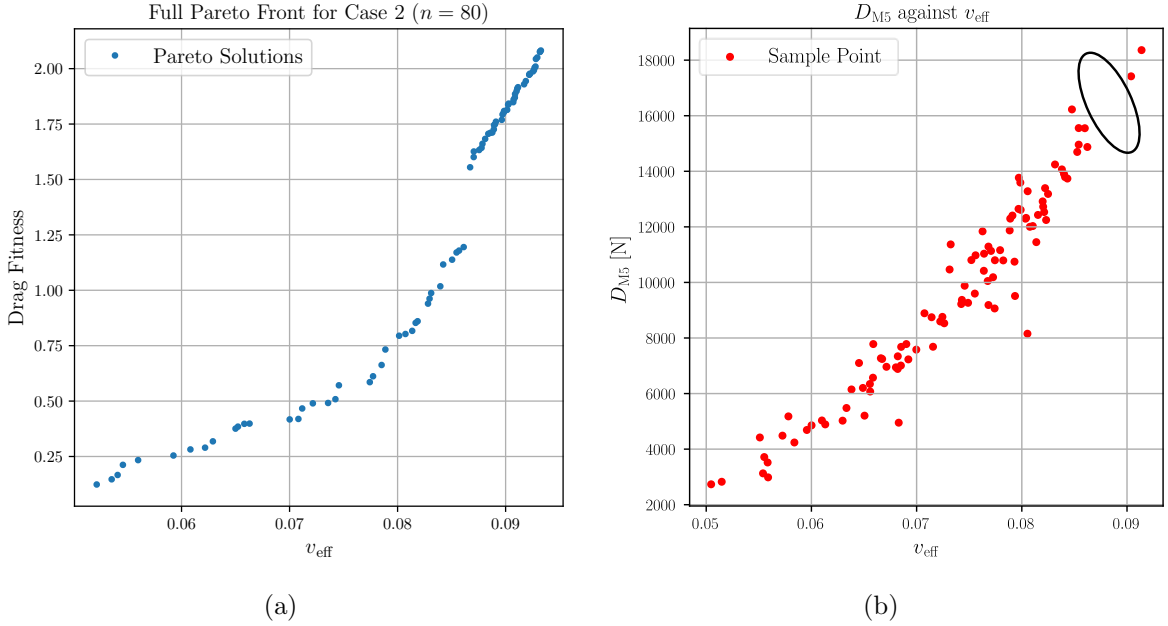


Figure 29: Full Pareto Front for Case 2 (a) and  $D_{M5}$  against  $v_{\text{eff}}$  across the sample points (b)

Figure 29a shows the full Pareto Front for Case 2. As observed, the range of the Drag Fitness is similar to the one found in Case 1 (Figure 24). Moreover, a similar range of volumetric efficiencies is achieved (see Figure 25c). Despite this, large “jumps” and “gaps” are seen throughout the Pareto Front. Figure 29b displays a gap highlighted in a black outline. This gap is reflected in the same region of the Pareto Front. This phenomenon has been deemed a result of the non-linearity of the cost function (i.e volumetric efficiency itself). Indeed, volumetric efficiency is obtained by taking the volume to the power of 2/3 divided by the wetted area. As such, the poor coverage of the volumetric efficiency with regards to other outputs like drag prevents the optimisation setup from reaching “continuous” Pareto Fronts similar to what has been shown in the previous cases.

### 3.3.2.3 Results from Case 3

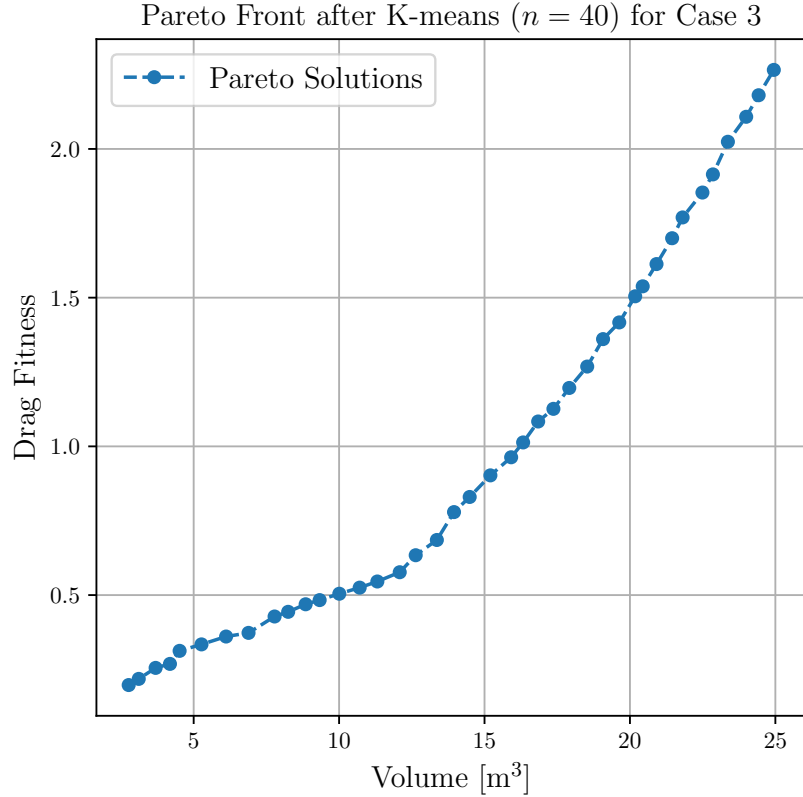


Figure 30: Representative Pareto Front for Case 3

Figure 30 shows the representative Pareto Front for Case 3. As expected, the Pareto Front has shifted upwards in terms of the Drag Fitness due to the addition of the viscous drag contribution. However, the overall behavior resembles Case 1 as the same two linear regions can be identified.

The viscous corrections employed are described in Section 2.6.3.3 in Equation (26). For a given set of flow conditions (Reynolds number, Mach number), these corrections become a function of the wetted area of the vehicle  $S_{\text{wet}}$ . Therefore, a waverider with a higher  $S_{\text{wet}}$  will have a higher viscous drag contribution according to the formula. Figure 31 shows the viscous drag contribution at M5 ( $\Delta D_{\text{visc}, \text{M5}}$ ) as well as the percentage of viscous drag with regards to overall drag at M5.

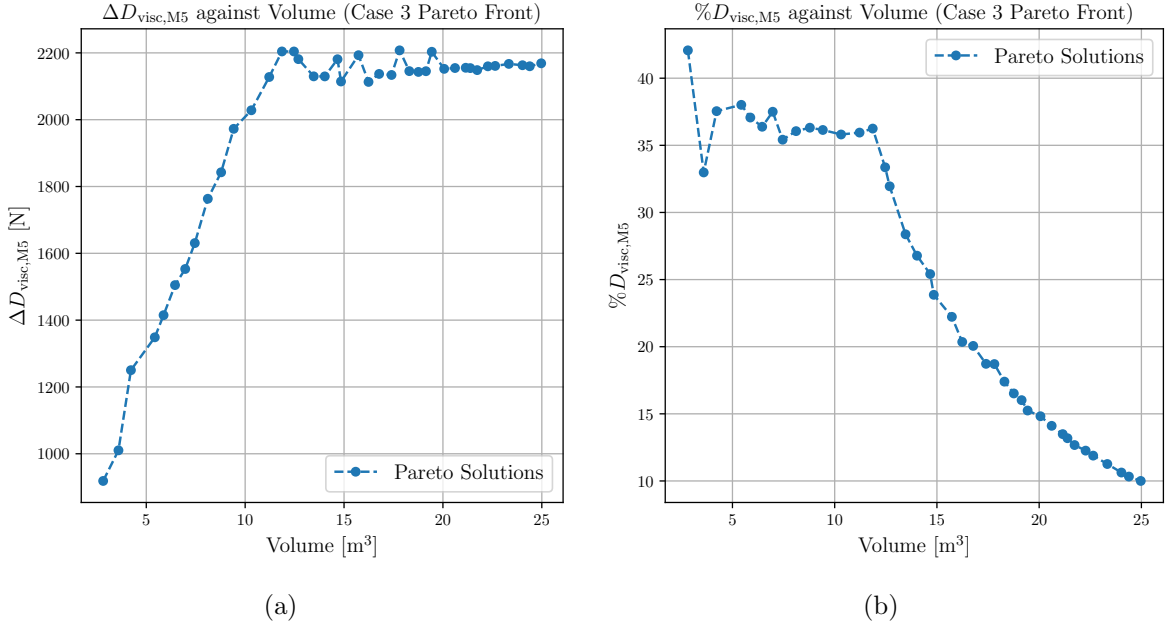


Figure 31: Absolute viscous drag contribution at M5 along the Case 3 Pareto Front (a)  
Percentage of viscous drag at M5 along the Case 3 Pareto Front (b)

In the first segment of the Pareto Front, the viscous drag contributions increase with volume (Figure 31a). This indicates that the wetted surface area increases with volume in this region. On the other hand, the viscous drag contribution remains more or less constant in the second segment, which indicates that  $S_{\text{wet}}$  remains constant, as expected from the discussion of Case 1 (Section 3.3.2.1). For the same reason, as overall drag increases, the percentage of viscous drag decreases in the second segment (Figure 31b). This reveals a shortcoming of the viscous corrections as one would not expect the same viscous drag contribution for waveriders of varying volume. Moreover, according to Anderson [10] who summarised the work by Bowcutt *et al.* [31], the main parameter which determines the balance between wave drag and viscous drag in a cone-derived waverider is the conical shock angle [10]. Indeed, Bowcutt *et al.* [31] determined an optimum for maximum  $L/D$  at a shock angle of 12 degrees, where viscous and wave drag are the same. Below this angle, viscous effects dominate ; above this angle, wave drag dominates [10]. Here, the viscous drag percentage varies greatly along the Pareto Front, despite the shock angle remaining fixed. Therefore, the viscous corrections used cannot be applied to this design space. Instead, methods like Newtonian Theory can be used as in the work by Bowcutt *et al.* [31] to provide more accurate estimates of viscous forces. Alternatively, viscous effects can also be computed via RANS CFD simulations, albeit at a high computational cost.

### 3.3.2.4 Results from Case 5

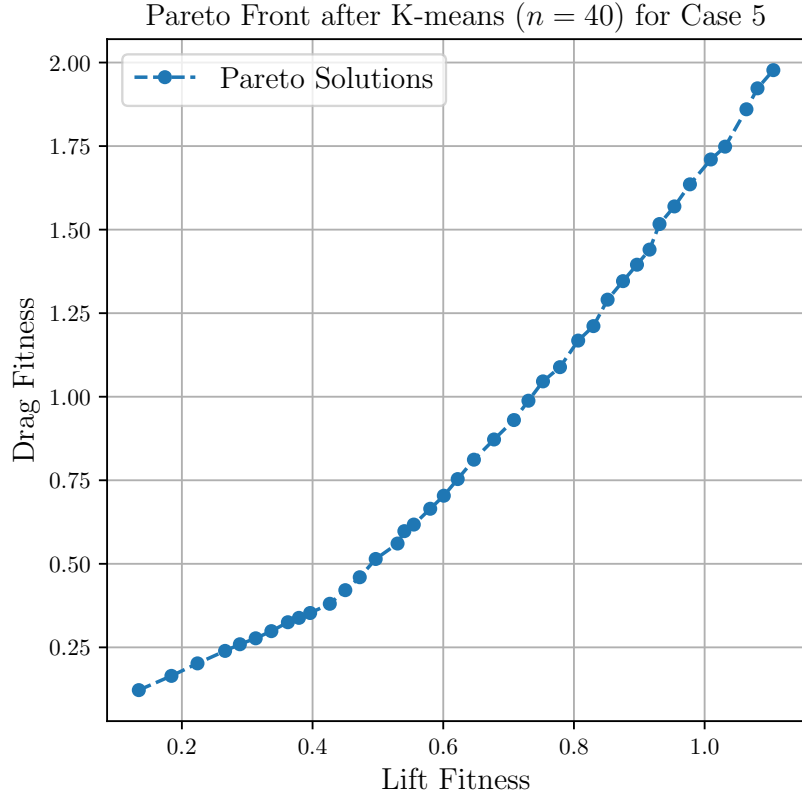
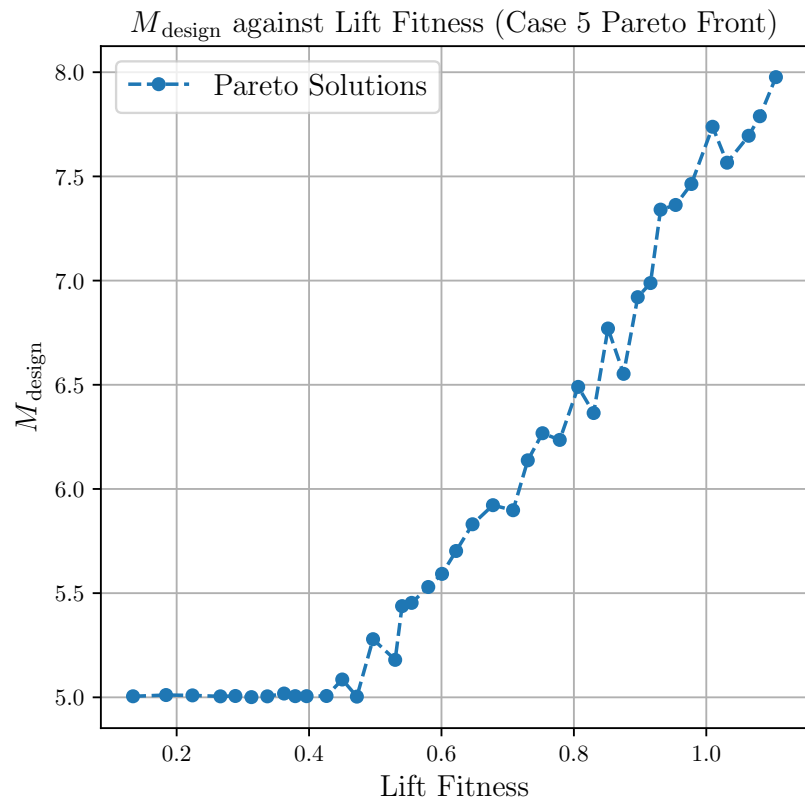


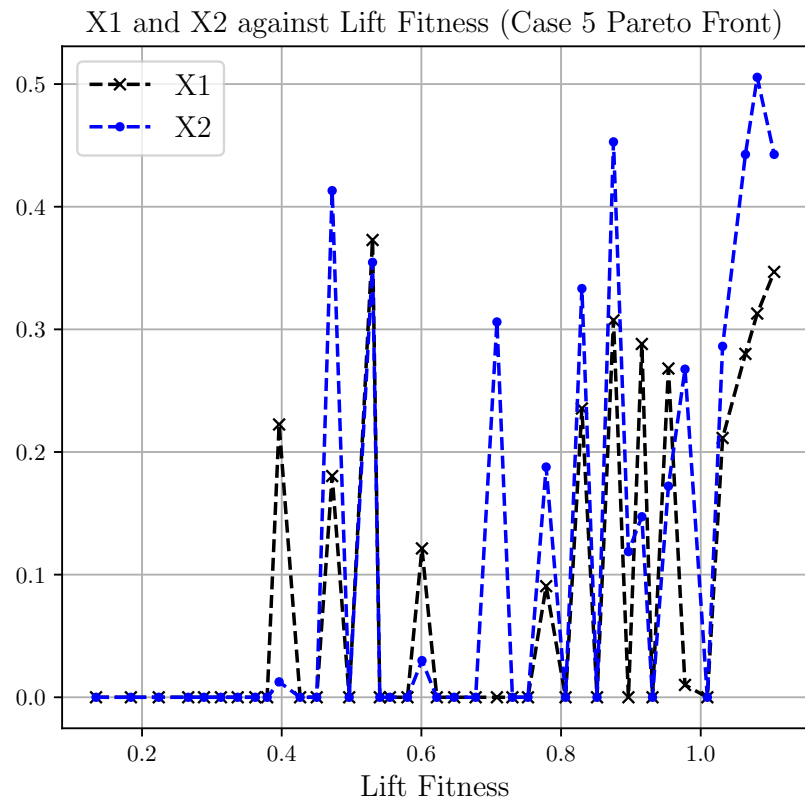
Figure 32: Representative Pareto Front for Case 5

The representative Pareto Front of Case 5 is shown in Figure 32. Similar to the previously discussed cases, the Pareto Front can be divided into two linear segments. The first, from minimum lift to  $\approx 0.4$ , appears equivalent to the first interval identified in Case 1. However, the second segment, from  $\approx 0.4$  to maximum lift, ends at a lower drag value than Case 1. This is because, as observed in Section 16, maximising lift is not equivalent to maximising drag. On the other hand, minimising lift and minimising drag have been shown to be equivalent objectives, and this explains why the first segment behaves similarly in both cases.

Figure 33 shows the behavior of  $M_{\text{design}}$  and  $X1-X2$  across the Pareto Front.



(a)



(b)

Figure 33: Variation of  $M_{\text{design}}$ (a) and X1-X2 (b) across the Case 5 Pareto Front

As shown in Figure 33a, the overall behavior of  $M_{\text{design}}$  matches that of Case 1. In the first interval, it is mostly constant at 5 and then starts increasing. However, the increase seen here is not like that of Case 1 as the solution oscillates much more in this case.

Moreover, the behavior of X1 and X2, shown in Figure 33b, further demonstrates that the second part of the Pareto Front differs from the previously established trends. Indeed, during the first interval, the values of X1 and X2 correspond to a flat Shockwave Curve (SC), which reinforces the fact that the first part of the Pareto Front is like that of Case 1. However, in the second interval there is no clear trend in the behavior of X1 and X2. Instead, the solutions obtained correspond neither to a maximum volume or minimum volume configuration. Once again, this can be explained by the fact that lift maximisation is not equivalent to maximising volume. It can be seen that the solutions reached resemble the maximum lift configuration discussed in Section 16.

Overall, these results demonstrate that maximising lift results in different kinds of solutions and behavior in the second part of the Pareto Front.

### 3.4 Longitudinal Analysis

This section discusses the longitudinal analysis performed as a post-optimisation step. Through the K-Means clustering algorithm, 10 geometries from the Case 1 Pareto Front were selected, including the minimum and maximum volume solutions. With the exception of the minimum volume solution, the inviscid flow at M5 around those geometries was solved at three angles of attack ( $\alpha = -2.5^\circ$ ,  $\alpha = 0^\circ$  and  $\alpha = 2.5^\circ$ ). To reduce computational cost and remain in the project's time frame, solving the flow at M8 was deemed outside the scope of this study. Note that the pitching moment coefficient  $C_M$  was obtained as:

$$C_M = \frac{M}{0.5 \cdot \rho_\infty \cdot U_\infty^2 \cdot S_{\text{ref}} \cdot l} \quad (29)$$

Where  $M$  is the pitching moment about a point,  $S_{\text{ref}} = 36 \text{ m}^2$  is a reference area and  $l = 7 \text{ m}$  is the length of the waverider.

Outside of its cruising condition ( $\alpha \neq 0^\circ$ ), the shock structure around the waverider will differ from the expected behavior in design conditions. Moreover, the upper surface is no longer freestream. The flow at the three angles of attack around one of the waveriders is shown in Figure 34.

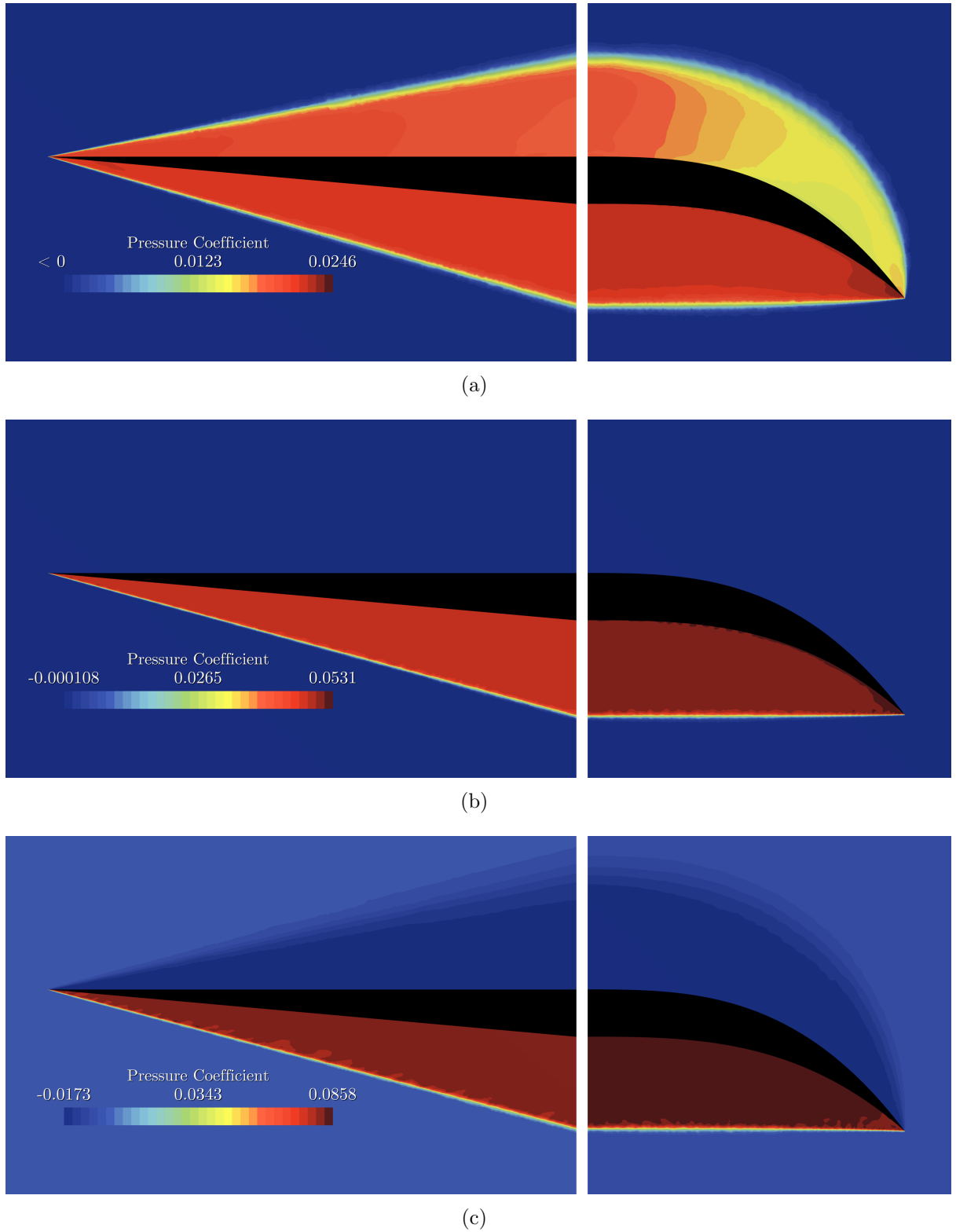


Figure 34: Contours of pressure coefficient around a waverider at  $\alpha = -2.5^\circ$  (a),  $\alpha = 0^\circ$  (b) and  $\alpha = 2.5^\circ$  (c) with a view from the symmetry plane (left) and base plane (right). M5 flow conditions.

As observed in Figure 34, a shock forms over the upper surface at  $\alpha = -2.5^\circ$ . The shock's intensity appears to decrease in the spanwise direction as lower pressure coefficients are

reached towards the right-side tip. Moreover, the pressure is positive throughout the shock.

At  $\alpha = 0^\circ$ , as expected the upper surface is freestream and the shock is contained to the lower surface. At  $\alpha = 2.5^\circ$ , an upper surface shock is produced again but this time the pressure coefficient is negative throughout the shock. Moreover, it appears more uniform in terms of spanwise pressure gradients than at  $\alpha = -2.5^\circ$ .

To understand the effect of these new shocks on the performance of the waveriders, the lift contribution from the upper surface and lift to drag ratio were measured at the three angles of attack. This is summarised in Table 18, where the subscript “US” stands for Upper Surface and  $\%L_{US}$  represents the percentage contribution of the upper surface on the total lift.

Table 18: Lift and  $L/D$  characteristics of the nine waveriders at the three angles considered

#	$V$ [m <sup>3</sup> ]	$M_{\text{design}}$	$\alpha = -2.5^\circ$			$\alpha = 0^\circ$	$\alpha = 2.5^\circ$		
			$L/D$	$L_{US}$ [N]	$\%L_{US}$		$L/D$	$L_{US}$ [N]	$\%L_{US}$
1	6.91	5.01	1.83	-11371	-85.39	11.60	8.53	9184	17.81
2	9.09	5.01	1.12	-15309	-90.79	11.60	8.56	12212	18.68
3	11.76	5.07	2.20	-16923	-82.11	11.18	8.33	13562	17.83
4	14.05	5.18	3.24	-19083	-66.04	8.72	7.15	14987	17.93
5	16.30	5.66	5.33	-18395	-48.08	8.36	6.71	14767	14.37
6	18.38	6.00	5.04	-19059	-41.15	7.11	5.97	15437	14.23
7	20.82	6.48	4.81	-19381	-35.37	6.24	5.38	15741	13.48
8	23.10	7.30	4.77	-19220	-29.51	5.65	4.93	15924	12.28
9	24.82	7.99	4.65	-19151	-26.65	5.32	4.68	16182	11.71

As seen in Table 18, at the lower angle of attack, the net lift produced by the upper surface is negative. This can be explained by the fact that the pressure coefficient is positive through the entire upper surface shock. This creates a region of high pressure above the upper surface which counters the lift produced by the lower surface. As a result, the pressure difference between the two surfaces is reduced and this results in the upper surface contributing negatively to the overall lift. The negative lift contribution is of the same order of magnitude across the nine configurations and generally increases with volume. Despite this, its effect is more prominent in the lower volume configurations where the upper surface causes up to 90% reduction in lift. In contrast, the upper surface causes only a 26.65% reduction in lift for the maximum volume waverider. This is because higher volume waveriders tend to produce more lift than lower volume ones. As a result, the effect is felt a lot more on the lower end of the volume range. For the same reason, ( $L/D$ ) is significantly reduced in the lower volume solutions compared to the cruising condition at  $\alpha = 0^\circ$  (for example,  $L/D = 1.12$  for the second waverider at  $\alpha = -2.5^\circ$ ).

Given that these estimates are obtained in a inviscid framework, one can even expect a further reduction in the lift to drag ratio if viscous effects are accounted for. Overall, this shows that lower volume configurations are not desirable as they are subject to a big loss in performance if ever disrupted into a negative angle of attack.

At the higher angle of attack ( $\alpha = 2.5^\circ$ ), the shock on the upper surface creates a region of low pressure, which provides a positive lift contribution to the overall lift. Similar to  $\alpha = -2.5^\circ$ , the contribution is of the same order of magnitude for all waveriders. However, the opposite effect occurs here, whereby the lower volume configurations have a higher  $\%L_{US}$  than the higher volume ones. The lift to drag ratio is still reduced but less than at  $\alpha = -2.5^\circ$ .

Experimental work [112, 113] has shown that the lift to drag ratio increases with  $\alpha$  to a maximum value, then proceeds to decrease. This is not the case here, which is likely due to the omission of viscous effects in the CFD setup.

Figure 35 shows how the  $x$  position of the centre of pressure varies with angle of attack. Also included are the variations of pitching moment  $C_M$  measured from the centre of volume, lift and drag.

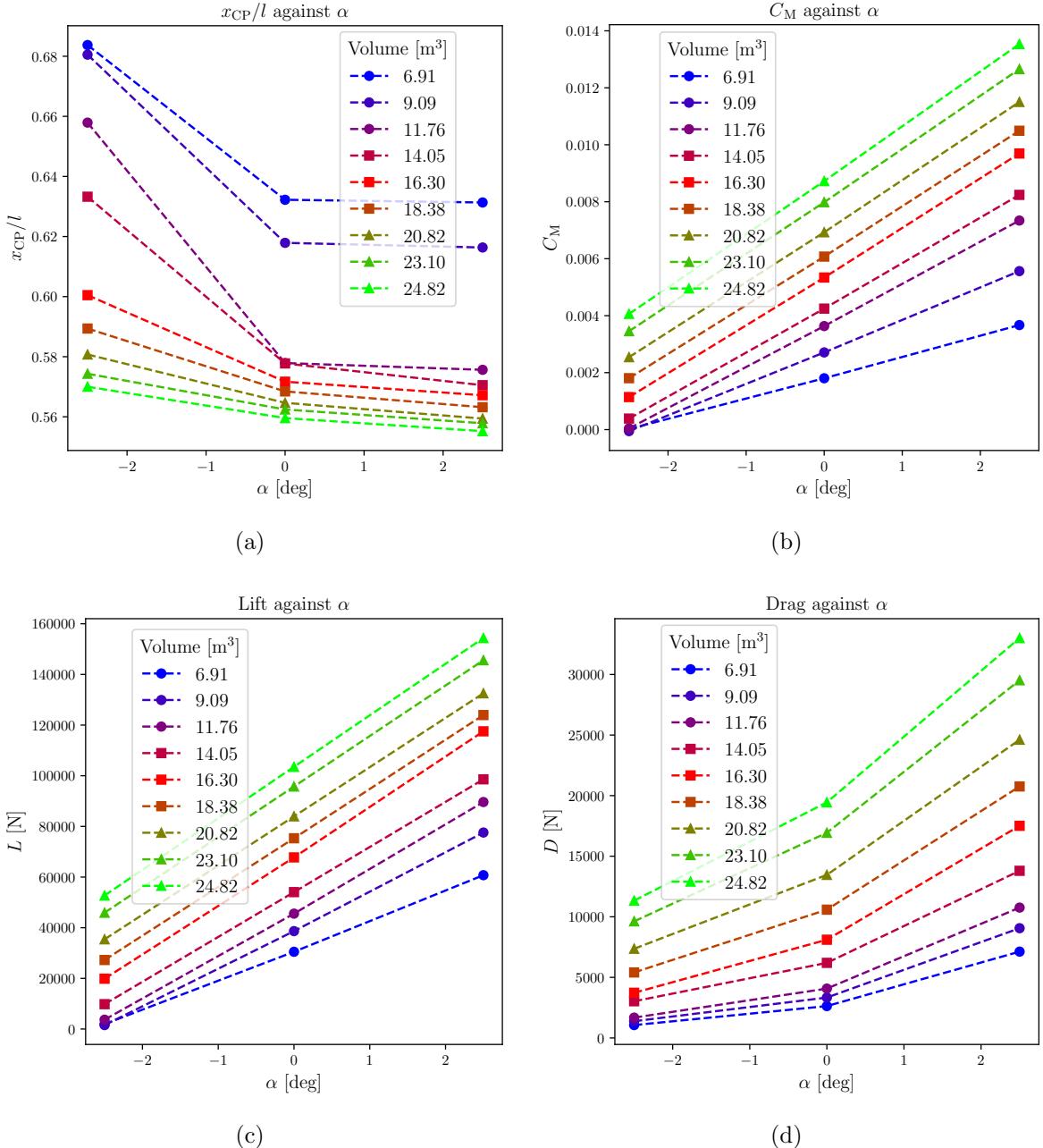


Figure 35:  $x_{CP}$  (a),  $C_M$  (b), Lift (c) and Drag (d) against angle of attack

As would be expected, the CP moves forward with an increase in angle of attack [114]. Furthermore, the higher the volume, the less the CP varies with angle of attack. This is a desirable trait as less variation in CP makes it easier to trim the aircraft and avoid unpredictable behavior [114]. It can also be observed that  $\alpha = -2.5^\circ$  causes a much larger change in CP from the cruising condition than  $\alpha = 2.5^\circ$ .

The moment coefficient  $C_M$ , measured from the center of mass (i.e assuming a uniform mass distribution) is plotted against  $\alpha$  in Figure 35b. To achieve static longitudinal stability, the following condition must be true [115]:

$$\frac{\partial C_M}{\partial \alpha} < 0 \quad (30)$$

Which represents a restoring moment.

Figure 35b clearly demonstrates that the condition is not met as the pitching moment coefficient increases with  $\alpha$ . This means that all the waveriders considered are longitudinally statically unstable if the CG is placed at the center of volume. Tarpley *et al.* [66] showed Caret waveriders are always longitudinally unstable when the CG is at the centre of mass. These results show that it is not just the case for Caret waveriders but for all solutions extracted from Case 1.

To achieve longitudinal static stability as in Equation (30), it is a well-known fact that the CG must be located ahead of the centre of pressure to provide the required restoring moment [116]. Therefore, the lower volume configurations provide a larger stability margin than higher volume solutions ; but this is at the expense of performance loss and larger variations in CP with  $\alpha$ .

Additionally, the lift increases linearly with angle of attack. However, the drag appears to increase in a non-linear manner. Both these trends are in line with experimental observations [113].

Overall, the longitudinal analysis demonstrates the fact that the volume remains a driving factor in the design and stability of waveriders. Moreover, this analysis shows that, while higher volume waveriders may reach lower lift to drag ratios and provide a smaller stability margin, they remain less affected by changes in  $\alpha$  in terms of:

- changes in centre of pressure.
- the detrimental effect of the shock on the upper surface at negative angles of attack.

## 4 Conclusions

An approach for the aerodynamic shape optimisation of hypersonic waveriders, based on the reference framework by Son *et al.* [16], was tested in this work. The approach made use of a design space based on osculating cone theory. Inviscid CFD simulations were used for performance estimation, and an accurate Kriging surrogate model was trained for outputs of interest. A genetic algorithm was then coupled to the surrogate models and used to perform optimisation.

An analysis of the design space was first performed. Lift and drag were found to decrease between M5 and M8 by around the same percentage, causing the lift to drag ratio to remain almost constant. Moreover, the trade-off relationship between lift/drag and volume was found to behave almost linearly. Feature Importances were then obtained via Random Forest Models (RFMs). Results show that the design Mach number is the driving factor for  $L/D$ , lift and drag. In particular,  $M_{\text{design}}$  appears to heavily influence the behavior of  $L/D$ . Volume remains primarily controlled by X2 due to the curvature of the shockwave playing the biggest role in the volume of the vehicle.

Single-objective optimisation test cases were then performed to assess the accuracy of the surrogate and performance of the overall optimisation setup, as well as identify any redundant optimisation objectives. Results show that minimising volume is equivalent to minimising lift and drag. Similarly, maximising volume is equivalent to maximising drag. However, rather unexpectedly, maximising lift results in its own optimum. Surrogate predictions were found to be quite accurate and generally below 1%, with a maximum error of about 3.5%.

Following the test cases, several multi-objective multi-point cases with conflicting objectives were run. Case 1's Pareto Front consists of two linear regions. In the first region, the optimisation favors solutions with a flat shockwave shape and a fixed design Mach number. In the second region,  $M_{\text{design}}$  begins increasing while favoring solutions with a flat upper surface, maximum curvature and a maximum flat shock region ( $X_1 = X_{1\text{crit}}$ ). Additionally, through Case 2 the volumetric efficiency was found to be an unsuitable optimisation objective due to the non-linearity in the way it is defined. Case 3 revealed that the viscous corrections cannot correctly account for viscous drag effects across the entire design space. As such, other methods like RANS CFD or Newtonian Theory may be used to estimate viscous contributions. Case 5, which consisted in maximising lift and minimising drag, displayed a similar first part of the Pareto Front as Case 1, favoring flat shockwave solutions. However, the second part of the Pareto Front is unique and the solutions reached resemble that of the single-objective test cases for lift maximisation. Overall, a major drawback of introducing  $M_{\text{design}}$  to the parameter space was identified, it being that there is less variety in the shapes reached in the Pareto Front compared to the work by Son *et al.* [16].

Finally, a longitudinal analysis of nine competitive solutions obtained in Case 1 was performed. The results show that, at negative angles of attack, the upper surface produces negative lift due to the formation of an upper surface shock. This has a significant impact on the performance of lower volume configurations, while higher volumes remain less affected by this phenomenon. In comparison, at positive angles of attack, the upper surface contributes positively to lift. Moreover, except for  $L/D$ , likely due to the omission of viscous effects, experimental work agrees with the trends obtained for lift and drag.

Furthermore, it was found that the centre of pressure changes less with angle of attack as volume increases, which is favorable for control of any aerospace vehicle via control surfaces. At the same time, the centre of pressure moves forward with volume. Higher volumes can therefore maintain a better performance across a wider range of angles of attack but this is at the expense of the centre of pressure moving forward, therefore providing smaller stability margins. It was also found that all waveriders considered are longitudinally statically unstable when the CG is placed at the centre of mass due to the centre of mass being located behind the centre of pressure.

## 5 Future Work

The purpose of this section is to outline recommendations for future work.

Of the utmost importance is the reproduction, at least in part, of this work in a viscous framework. Indeed, while viscous effects are usually assumed less important than pressure effects in this regime, the omission of the former adds uncertainties to the results at every step of the optimisation process. Key optimisation results may be proven false when making the switch to viscous CFD simulations. Furthermore, critical hypersonic issues like aerodynamic heating cannot be fully accounted for within an inviscid framework.

As a further extension of this optimisation framework, lateral-directional (and more generally dynamic) stability should be integrated. Given the established design space can produce a wide variety of shapes, investigating these types of stabilities as a function of the design parameters may reveal additional trends which have not been identified here. Additionally, a similar analysis should be conducted at M8 as it is lacking in this study due to the allocated time frame.

Another issue to give additional thought to is the change in the shockwave shape in off-design conditions. Here, a very simplified quantification of this issue was presented through the shock angle at the symmetry plane. However, a more sophisticated approach may be needed and which would potentially allow the change in the shockwave shape to become an optimisation objective in itself. It would also be worth accounting for more than just two flow conditions in the optimisation process. Especially given that a hypersonic commercial aircraft like the one Destinus is developing will be expected to go from the subsonic all the way to the hypersonic regime on its own. For this reason, considering subsonic speeds in the optimisation process, much like in the vortex-integrated waverider approach, is worth investigating.

From a more general point of view, the use of a Neural Network within this design space can reveal trends and behavior which cannot be easily identified by human engineers. With the increasing popularity of Neural Networks into most engineering fields, it makes sense to explore its feasibility within the waverider field of research.

Finally, while a lot of thought has been put into ensuring and demonstrating the results achieved by the inviscid setup and surrogate are reliable, there is a need to implement uncertainty quantification methods to gauge the robustness and accuracy of said results. This would allow the designer to account for potential inconsistencies in the simulation setup.

## Appendix A : Pareto Fronts

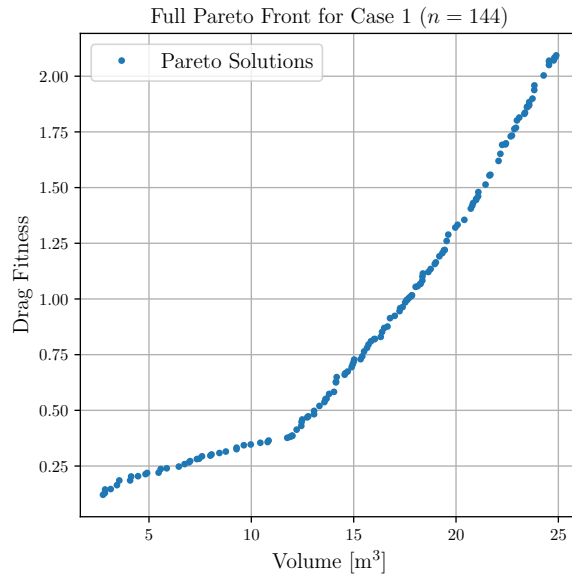


Figure 36: Full Pareto Front for Case 1

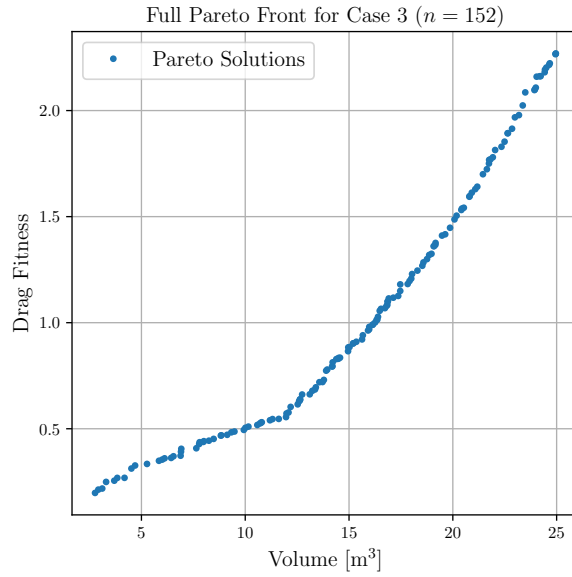


Figure 37: Full Pareto Front for Case 3

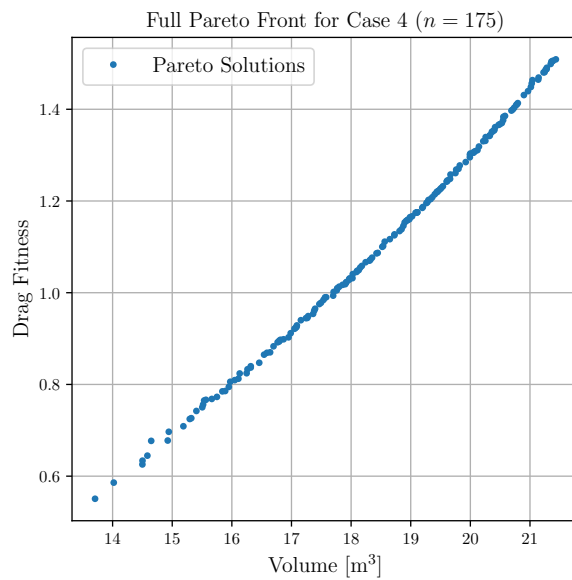


Figure 38: Full Pareto Front for Case 4

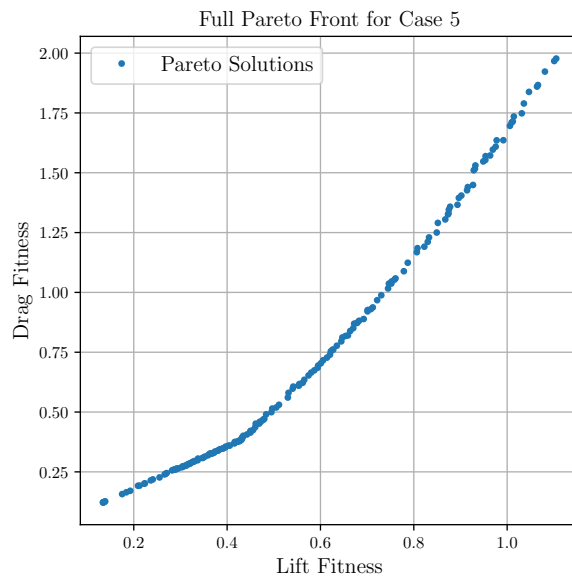


Figure 39: Full Pareto Front for Case 5

## Appendix B : Sample Points

Index	$M_{\text{design}}$	X1	X2	X3	X4
1	5.891	0.050	0.344	0.738	0.180
2	7.577	0.353	0.225	0.680	0.671
3	5.390	0.200	0.277	0.358	0.474
4	6.827	0.047	0.601	0.508	0.467
5	6.947	0.237	0.040	0.218	0.828
6	6.103	0.259	0.432	0.785	0.693
7	6.407	0.013	0.865	0.367	0.519
8	6.395	0.145	0.239	0.604	0.743
9	5.561	0.298	0.247	0.959	0.564
10	7.907	0.264	0.082	0.337	0.794
11	7.232	0.117	0.758	0.819	0.888
12	6.962	0.204	0.799	0.207	0.458
13	7.910	0.219	0.180	0.099	0.192
14	5.081	0.247	0.540	0.244	0.202
15	7.293	0.089	0.532	0.476	0.228
16	5.217	0.177	0.519	0.132	0.816
17	7.730	0.053	0.922	0.402	0.915
18	5.573	0.349	0.191	0.279	0.269
19	6.422	0.530	0.093	0.825	0.238
20	7.816	0.149	0.058	0.853	0.374
21	5.561	0.247	0.673	0.961	0.839
22	5.933	0.085	0.739	0.083	0.873
23	5.462	0.068	0.800	0.878	0.403
24	6.413	0.235	0.741	0.371	0.083
25	6.385	0.120	0.883	0.485	0.944
26	6.317	0.308	0.102	0.126	0.592
27	5.774	0.089	0.134	0.375	0.846
28	7.610	0.228	0.089	0.106	0.634
29	7.169	0.101	0.187	0.592	0.136
30	6.728	0.113	0.303	0.089	0.167
31	6.967	0.154	0.777	0.348	0.876
32	5.573	0.259	0.077	0.800	0.021
33	6.479	0.227	0.044	0.853	0.939
34	5.186	0.212	0.495	0.506	0.888
35	7.259	0.773	0.001	0.171	0.653
36	5.999	0.344	0.165	0.755	0.144
37	6.488	0.211	0.703	0.677	0.854
38	5.569	0.441	0.168	0.220	0.839
39	6.191	0.111	0.755	0.677	0.109
40	6.257	0.140	0.530	0.095	0.943
41	5.225	0.182	0.082	0.446	0.872
42	7.733	0.173	0.917	0.005	0.013

Continued on next page

Index	$M_{\text{design}}$	X1	X2	X3	X4
43	7.376	0.490	0.158	0.948	0.652
44	6.869	0.037	0.885	0.907	0.713
45	7.502	0.008	0.206	0.505	0.034
46	6.929	0.093	0.623	0.985	0.141
47	6.341	0.082	0.998	0.806	0.439
48	5.993	0.051	0.301	0.357	0.668
49	5.623	0.064	0.568	0.581	0.095
50	5.831	0.155	0.733	0.805	0.275
51	7.589	0.198	0.639	0.392	0.582
52	5.735	0.388	0.069	0.162	0.544
53	7.468	0.101	0.395	0.728	0.541
54	5.921	0.097	0.939	0.575	0.953
55	6.677	0.052	0.266	0.943	0.669
56	7.100	0.422	0.082	0.431	0.353
57	7.541	0.499	0.131	0.867	0.203
58	5.099	0.147	0.869	0.607	0.299
59	7.079	0.214	0.804	0.550	0.378
60	7.055	0.199	0.247	0.641	0.659
61	7.787	0.448	0.112	0.161	0.826
62	6.866	0.320	0.343	0.065	0.205
64	7.748	0.052	0.359	0.119	0.347
65	5.078	0.234	0.290	0.356	0.467
66	5.645	0.035	0.221	0.159	0.011
67	5.087	0.121	0.179	0.693	0.613
68	7.697	0.067	0.405	0.139	0.903
69	7.634	0.169	0.230	0.457	0.523
70	5.411	0.149	0.833	0.357	0.725
71	7.973	0.041	0.029	0.667	0.985
72	6.866	0.384	0.261	0.324	0.465
73	6.353	0.587	0.063	0.747	0.615
74	6.419	0.157	0.147	0.049	0.145
75	6.551	0.357	0.385	0.151	0.507
76	7.241	0.055	0.737	0.021	0.815
77	5.237	0.597	0.045	0.869	0.577
78	6.851	0.185	0.593	0.033	0.769
79	6.548	0.244	0.305	0.331	0.807
80	7.331	0.507	0.095	0.473	0.887
81	5.318	0.193	0.718	0.831	0.162
82	7.295	0.017	0.662	0.869	0.628
83	5.891	0.057	0.995	0.939	0.077
84	5.951	0.269	0.515	0.553	0.263
85	6.077	0.319	0.099	0.343	0.609
86	6.035	0.115	0.916	0.456	0.139
87	5.435	0.338	0.347	0.635	0.779
88	6.065	0.175	0.643	0.223	0.075

Continued on next page

Index	$M_{\text{design}}$	X1	X2	X3	X4
89	7.229	0.317	0.445	0.795	0.027
90	6.599	0.119	0.699	0.047	0.111
91	7.595	0.127	0.103	0.467	0.937
92	6.004	0.131	0.659	0.711	0.824
93	5.267	0.477	0.049	0.509	0.751
94	6.533	0.191	0.620	0.581	0.171
95	6.347	0.151	0.899	0.063	0.349
96	5.393	0.059	0.233	0.849	0.805
97	5.927	0.171	0.811	0.901	0.619
98	5.711	0.501	0.005	0.987	0.251
99	5.615	0.243	0.487	0.387	0.433
100	6.173	0.409	0.165	0.073	0.853

## Appendix C : Waverider Generator Example

```
1 from waverider_generator.generator import waverider as wr
2 from waverider_generator.cad_export import to_CAD
3
4 # M_design
5 M_design=5
6
7 # Shock angle beta
8 beta=15
9
10 # height h
11 height=1.876
12
13 # half width w
14 half_width=4.2
15
16 # parameters X1, X2, X3, X4
17 dp=[0.317,0.445,0.795,0.027]
18
19 # discretisation parameters
20 # number of osculating planes
21 n_planes=30
22 # number of points in streamwise direction in USC and flat region of
23 # SC
24 n_streamwise=30
25 # maximum integration distance for streamline tracing
26 delta_streamwise=0.05
27
28 # initialise the waverider instance
29 waverider=wr(M_inf=M_design,
30             beta=beta,
31             height=height,
32             width=half_width,
33             dp=dp,
34             n_upper_surface=10000,
35             n_shockwave=10000,
36             n_planes=n_planes,
37             n_streamwise=n_streamwise,
38             delta_streamwise=delta_streamwise)
39
40 # export cad, scale 1000 to get meters
41 to_CAD(waverider=waverider,sides='both',export=True,filename='
        waverider_example.step',scale=1000)
```

## Appendix D : CURES Approval Letter



21 May 2024

Dear Mr Nassif,

Reference: CURES/22180/2024

Project ID: 25461

Title: Flow Control for Hypersonic Vehicles

Thank you for your application to the Cranfield University Research Ethics System (CURES).

**We are pleased to inform you your CURES application, reference CURES/22180/2024 has been reviewed. You may now proceed with the research activities you have sought approval for.**

If you have any queries, please contact CURES Support.

We wish you every success with your project.

Regards,

CURES Team

Figure 40: CURES Approval Letter

## References

- [1] D. Küchemann. "Hypersonic aircraft and their aerodynamic problems". In: *Progress in Aerospace Sciences* 6 (Jan. 1965), pp. 271–353. ISSN: 03760421. DOI: 10.1016/0376-0421(65)90006-0.
- [2] World Economic Forum. *Meet the new generation of supersonic planes — World Economic Forum*. Oct. 2022. URL: <https://www.weforum.org/agenda/2022/10/supersonic-flight-sustainable-aviation/>.
- [3] Boom Supersonic. *Boom - Sustainability*. URL: <https://boomsupersonic.com/sustainability>.
- [4] Maya Belkovska. *Destinus: Innovating Zero-Emission Hypersonic Travel for a Sustainable Future*. July 2024. URL: <https://netzerocompare.com/services/destinus>.
- [5] Gustavo Alonso et al. "Investigations on the distribution of air transport traffic and CO<sub>2</sub> emissions within the European Union". In: *Journal of Air Transport Management* 36 (2014), pp. 85–93.
- [6] Talal Yusaf et al. "Sustainable Aviation—Hydrogen Is the Future". In: *Sustainability* 14.1 (Jan. 2022), p. 548. ISSN: 2071-1050. DOI: 10.3390/su14010548.
- [7] National Aeronautics and Space Administration. *What is Drag?* URL: <https://www1.grc.nasa.gov/beginners-guide-to-aeronautics/what-is-drag/>.
- [8] Robert T Jones. *Theory of wing-body drag at supersonic speeds*. Tech. rep. 1956.
- [9] ALLEN E. PUCKETT. "Supersonic Wave Drag of Thin Airfoils". In: *Journal of the Aeronautical Sciences* 13.9 (Sept. 1946), pp. 475–484. ISSN: 1936-9956. DOI: 10.2514/8.11425.
- [10] John D Anderson Jr. "APPLIED HYPERSONIC AERODYNAMICS: HYPERSONIC WAVERIDERS". In: *Fundamentals of Aerodynamics*. 6th ed. New York: McGraw-Hill Education, Mar. 2016. Chap. 14.9, pp. 908–921.
- [11] T. R. F. Nonweiler. "Aerodynamic Problems of Manned Space Vehicles". In: *The Journal of the Royal Aeronautical Society* 63.585 (Sept. 1959), pp. 521–528. ISSN: 0368-3931. DOI: 10.1017/S0368393100071662.
- [12] Dietrich Küchemann. *The Aerodynamic Design of Aircraft*. Reston, Virginia: American Institute of Aeronautics and Astronautics, Inc., Sept. 2012. ISBN: 978-1-60086-922-8. DOI: 10.2514/4.869228.
- [13] JOHN ANDERSON JR and Mark Lewis. "Hypersonic waveriders-Where do we stand?" In: *31st Aerospace Sciences Meeting*. 1993, p. 399.
- [14] John D. Anderson. *Hypersonic and High-Temperature Gas Dynamics, Third Edition*. Reston, VA: American Institute of Aeronautics and Astronautics, Inc., Mar. 2019. ISBN: 978-1-62410-514-2. DOI: 10.2514/4.105142.
- [15] Frederick Ferguson, Mookesh Dhanasar, and Isaiah M. Blankson. "Waverider Design and Analysis". In: *20th AIAA International Space Planes and Hypersonic Systems and Technologies Conference*. Reston, Virginia: American Institute of Aeronautics and Astronautics, July 2015. ISBN: 978-1-62410-320-9. DOI: 10.2514/6.2015-3508.
- [16] Jiwon Son, Chankyu Son, and Kwanjung Yee. "A Novel Direct Optimization Framework for Hypersonic Waverider Inverse Design Methods". In: *Aerospace* 9.7 (June 2022), p. 348. ISSN: 2226-4310. DOI: 10.3390/aerospace9070348.
- [17] Helle M Sayler. *Hypersonic weapons: Background and issues for Congress*. Congressional Research Service USA, 2019.

- [18] Steven Walker et al. “The DARPA/AF falcon program: The hypersonic technology vehicle# 2 (HTV-2) flight demonstration phase”. In: *15th AIAA International Space Planes and Hypersonic Systems and Technologies Conference*. 2008, p. 2539.
- [19] Amritansh Pratap Singh, Vini Choudhary, and Devender Sharma. “Design and development of hypersonic aerial vehicles”. In: *Advances in Interdisciplinary Engineering: Select Proceedings of FLAME 2020*. 2021, pp. 457–467.
- [20] Xiaogang Zheng et al. “Multiple Osculating Cones’ Waverider Design Method for Ruled Shock Surfaces”. In: *AIAA Journal* 58.2 (Feb. 2020), pp. 854–866. ISSN: 0001-1452. DOI: 10.2514/1.J058640.
- [21] Charles R McClinton. “High speed/hypersonic aircraft propulsion technology development”. In: *Advances on propulsion technology for high-speed aircraft* 1 (2007), pp. 1–32.
- [22] US Air Force. *X-51A Waverider*. URL: <https://www.af.mil/News/Photos/igphoto/2000360693/>.
- [23] David Neyland. *Hypersonic Technology Vehicle HTV-2 reentry (artist's impression)*. URL: [http://web.archive.org/web/20101226085818/http://www.ifpacfletcherconference.com/2010/powerpoint/David\\_Neyland.ppt](http://web.archive.org/web/20101226085818/http://www.ifpacfletcherconference.com/2010/powerpoint/David_Neyland.ppt).
- [24] Feng Ding et al. “An overview of research on waverider design methodology”. In: *Acta Astronautica* 140 (Nov. 2017), pp. 190–205. ISSN: 00945765. DOI: 10.1016/j.actaastro.2017.08.027.
- [25] Zhen-tao Zhao et al. “An overview of research on wide-speed range waverider configuration”. In: *Progress in Aerospace Sciences* 113 (Feb. 2020), p. 100606. ISSN: 03760421. DOI: 10.1016/j.paerosci.2020.100606.
- [26] M. A. Zubin and N. A. Ostapenko. “Experimental investigation of some singularities of the supersonic flow around V-shaped wings”. In: *Fluid Dynamics* 10.4 (1976), pp. 647–652. ISSN: 0015-4628. DOI: 10.1007/BF01026712.
- [27] M. A. Zubin and N. A. Ostapenko. “The flow structure near the windward side of V-shaped wings with an attached shock wave on the leading edges”. In: *Fluid Dynamics* 21.1 (1986), pp. 104–112. ISSN: 0015-4628. DOI: 10.1007/BF01051109.
- [28] N. A. Ostapenko. “Aerodynamic characteristics of V-shaped wings with shock waves detached from leading edges at hypersonic speeds”. In: *Fluid Dynamics* 28.4 (July 1993), pp. 545–552. ISSN: 0015-4628. DOI: 10.1007/BF01342691.
- [29] I. I. Mazhul and R. D. Rakhcimov. “Hypersonic Power-Law Shaped Waveriders in Off-Design Regimes”. In: *Journal of Aircraft* 41.4 (July 2004), pp. 839–845. ISSN: 0021-8669. DOI: 10.2514/1.386.
- [30] J. G. Jones et al. “A method for designing lifting configurations for high supersonic speeds, using axisymmetric flow fields”. In: *Ingenieur-Archiv* 37.1 (1968), pp. 56–72. ISSN: 0020-1154. DOI: 10.1007/BF00532683.
- [31] Kevin G Bowcutt, Digeo Capriotti, and John D Anderson. “Viscous optimized hypersonic waveriders”. In: *25th AIAA Aerospace Sciences Meeting*. Reston, Virginia: American Institute of Aeronautics and Astronautics, Mar. 1987. DOI: 10.2514/6.1987-272.
- [32] M. RASMUSSEN. “Lifting-body configurations derived from supersonic flows past inclined circular and elliptic cones”. In: *5th Atmospheric Flight Mechanics Conference for Future Space Systems*. Reston, Virginia: American Institute of Aeronautics and Astronautics, Aug. 1979. DOI: 10.2514/6.1979-1665.

- [33] Maurice L. Rasmussen. "Waverider Configurations Derived from Inclined Circular and Elliptic Cones". In: *Journal of Spacecraft and Rockets* 17.6 (Nov. 1980), pp. 537–545. ISSN: 0022-4650. DOI: 10.2514/3.57771.
- [34] M.L. Rasmussen, M.C. Jischke, and D.C. Daniel. "Experimental Forces and Moments on Cone-Derived Waveriders for  $M = 3$  to 5". In: *Journal of Spacecraft and Rockets* 19.6 (Nov. 1982), pp. 592–598. ISSN: 0022-4650. DOI: 10.2514/3.62306.
- [35] Sheam-Chyun Lin and Yu-Shan Luo. "Optimization of waverider configurations generated from inclined circular and elliptic cones". In: *International Aerospace Planes and Hypersonics Technologies*. Reston, Virginia: American Institute of Aeronautics and Astronautics, Apr. 1995. DOI: 10.2514/6.1995-6089.
- [36] Kai Cui and GuoWei Yang. "The effect of conical flowfields on the performance of waveriders at Mach 6". In: *Chinese Science Bulletin* 52.1 (Jan. 2007), pp. 57–64. ISSN: 1001-6538. DOI: 10.1007/s11434-007-0026-2.
- [37] Naruhisa Takashima and Mark J. Lewis. "Wedge-cone waverider configuration for engine-airframe interaction". In: *Journal of Aircraft* 32.5 (Sept. 1995), pp. 1142–1144. ISSN: 0021-8669. DOI: 10.2514/3.46848.
- [38] Helmut Sobieczky, F Dougherty, and Kevin Jones. "Hypersonic Waverider Design from Given Shock Waves". In: May 1990.
- [39] Patrick Rodi. "The Osculating Flowfield Method of Waverider Geometry Generation". In: *43rd AIAA Aerospace Sciences Meeting and Exhibit*. Reston, Virginia: American Institute of Aeronautics and Astronautics, Jan. 2005. ISBN: 978-1-62410-064-2. DOI: 10.2514/6.2005-511.
- [40] Patrick Rodi. "Preliminary Ramjet/Scramjet Integration with Vehicles Using Osculating Flowfield Waverider Forebodies". In: *30th AIAA Applied Aerodynamics Conference*. Reston, Virginia: American Institute of Aeronautics and Astronautics, June 2012. ISBN: 978-1-62410-185-4. DOI: 10.2514/6.2012-3223.
- [41] Marie-Laure Chauffour and Mark Lewis. "Corrected Waverider Design for Inlet Applications". In: *40th AIAA/ASME/SAE/ASEE Joint Propulsion Conference and Exhibit*. Reston, Virginia: American Institute of Aeronautics and Astronautics, July 2004. ISBN: 978-1-62410-037-6. DOI: 10.2514/6.2004-3405.
- [42] Jinghui Guo et al. "Parametric study on the heat transfer of a blunt body with counterflowing jets in hypersonic flows". In: *International Journal of Heat and Mass Transfer* 121 (June 2018), pp. 84–96. ISSN: 00179310. DOI: 10.1016/j.ijheatmasstransfer.2017.12.115.
- [43] W. A. Engblom and D. B. Goldstein. "Nose-tip surface heat reduction mechanism". In: *Journal of Thermophysics and Heat Transfer* 10.4 (Oct. 1996), pp. 598–606. ISSN: 0887-8722. DOI: 10.2514/3.835.
- [44] Dante D'Orazio. *DARPA's HTV-2 aircraft test flight failed due to heat stresses at Mach 20*. Apr. 2012. URL: <https://www.theverge.com/2012/4/22/2967089/darpa-htv-2-results-mach-20>.
- [45] W. A. Engblom et al. "Fluid Dynamics of Hypersonic Forward-Facing Cavity Flow". In: *Journal of Spacecraft and Rockets* 34.4 (July 1997), pp. 437–444. ISSN: 0022-4650. DOI: 10.2514/2.3255.
- [46] Wei Huang et al. "Drag and heat reduction mechanism in the combinational opposing jet and acoustic cavity concept for hypersonic vehicles". In: *Aerospace Science and Technology* 42 (Apr. 2015), pp. 407–414. ISSN: 12709638. DOI: 10.1016/j.ast.2015.01.029.

- [47] Wei Huang et al. "Heat flux reduction mechanism induced by a combinational opposing jet and cavity concept in supersonic flows". In: *Acta Astronautica* 121 (Apr. 2016), pp. 164–171. ISSN: 00945765. DOI: [10.1016/j.actaastro.2016.01.008](https://doi.org/10.1016/j.actaastro.2016.01.008).
- [48] R. Kalimuthu, R. C. Mehta, and E. Rathakrishnan. "Drag Reduction for Spike Attached to Blunt-Nosed Body at Mach 6". In: *Journal of Spacecraft and Rockets* 47.1 (Jan. 2010), pp. 219–222. ISSN: 0022-4650. DOI: [10.2514/1.46023](https://doi.org/10.2514/1.46023).
- [49] Wei Huang et al. "Drag and heat flux reduction mechanism of blunted cone with aerodisks". In: *Acta Astronautica* 138 (Sept. 2017), pp. 168–175. ISSN: 00945765. DOI: [10.1016/j.actaastro.2017.05.040](https://doi.org/10.1016/j.actaastro.2017.05.040).
- [50] Xi-wan Sun et al. "Multiobjective Design Optimization of Hypersonic Combinational Novel Cavity and Opposing Jet Concept". In: *Journal of Spacecraft and Rockets* 54.3 (May 2017), pp. 662–671. ISSN: 0022-4650. DOI: [10.2514/1.A33801](https://doi.org/10.2514/1.A33801).
- [51] Xiaoqing Chen et al. "Multi-Object Optimization of Waverider Generated from Conical Flow and Osculating Cone". In: *46th AIAA Aerospace Sciences Meeting and Exhibit*. Reston, Virginia: American Institute of Aeronautics and Astronautics, Jan. 2008. ISBN: 978-1-62410-128-1. DOI: [10.2514/6.2008-131](https://doi.org/10.2514/6.2008-131).
- [52] DANIEL STEVENS. "Practical considerations in waverider applications". In: *Guidance, Navigation and Control Conference*. Reston, Virginia: American Institute of Aeronautics and Astronautics, Aug. 1992. DOI: [10.2514/6.1992-4247](https://doi.org/10.2514/6.1992-4247).
- [53] T. Eggers, H. Sobieczky, and K. Center. "Design of advanced waveriders with high aerodynamic efficiency". In: *5th International Aerospace Planes and Hypersonics Technologies Conference*. Reston, Virginia: American Institute of Aeronautics and Astronautics, Nov. 1993. DOI: [10.2514/6.1993-5141](https://doi.org/10.2514/6.1993-5141).
- [54] FaMin Wang, HaiHe Ding, and MaiFang Lei. "Aerodynamic characteristics research on wide-speed range waverider configuration". In: *Science in China Series E: Technological Sciences* 52.10 (Oct. 2009), pp. 2903–2910. ISSN: 1006-9321. DOI: [10.1007/s11431-009-0258-2](https://doi.org/10.1007/s11431-009-0258-2).
- [55] ShiBin Li et al. "Design and aerodynamic investigation of a parallel vehicle on a wide-speed range". In: *Science China Information Sciences* 57.12 (Dec. 2014), pp. 1–10. ISSN: 1674-733X. DOI: [10.1007/s11432-014-5225-2](https://doi.org/10.1007/s11432-014-5225-2).
- [56] Jun Liu et al. "Novel osculating flowfield methodology for wide-speed range waverider vehicles across variable Mach number". In: *Acta Astronautica* 162 (Sept. 2019), pp. 160–167. ISSN: 00945765. DOI: [10.1016/j.actaastro.2019.05.056](https://doi.org/10.1016/j.actaastro.2019.05.056).
- [57] Patrick Rodi. "Vortex Lift Waverider Configurations". In: *50th AIAA Aerospace Sciences Meeting including the New Horizons Forum and Aerospace Exposition*. Reston, Virginia: American Institute of Aeronautics and Astronautics, Jan. 2012. ISBN: 978-1-60086-936-5. DOI: [10.2514/6.2012-1238](https://doi.org/10.2514/6.2012-1238).
- [58] Feng Qu et al. "Aerodynamic shape optimization of the vortex-shock integrated waverider over a wide speed range". In: *Aerospace Science and Technology* 143 (Dec. 2023), p. 108696. ISSN: 12709638. DOI: [10.1016/j.ast.2023.108696](https://doi.org/10.1016/j.ast.2023.108696).
- [59] Chuanzhen Liu et al. "Research on the design of double swept waverider". In: *21st AIAA International Space Planes and Hypersonics Technologies Conference*. Reston, Virginia: American Institute of Aeronautics and Astronautics, Mar. 2017. ISBN: 978-1-62410-463-3. DOI: [10.2514/6.2017-2140](https://doi.org/10.2514/6.2017-2140).
- [60] Michael V Cook. *Flight Dynamics Principles*. 2nd ed. Elsevier, 2007. ISBN: 9780080982427. DOI: [10.1016/C2010-0-65889-5](https://doi.org/10.1016/C2010-0-65889-5).

- [61] Tamas Bykerk, Dries Verstraete, and Johan Steelant. “Low speed longitudinal aerodynamic, static stability and performance analysis of a hypersonic waverider”. In: *Aerospace Science and Technology* 96 (Jan. 2020), p. 105531. ISSN: 12709638. DOI: [10.1016/j.ast.2019.105531](https://doi.org/10.1016/j.ast.2019.105531).
- [62] Tamas Bykerk, Dries Verstraete, and Johan Steelant. “Low speed lateral-directional aerodynamic and static stability analysis of a hypersonic waverider”. In: *Aerospace Science and Technology* 98 (Mar. 2020), p. 105709. ISSN: 12709638. DOI: [10.1016/j.ast.2020.105709](https://doi.org/10.1016/j.ast.2020.105709).
- [63] Tamas Bykerk, Dries Verstraete, and Johan Steelant. “Low speed longitudinal dynamic stability analysis of a hypersonic waverider using unsteady Reynolds averaged Navier Stokes forced oscillation simulations”. In: *Aerospace Science and Technology* 103 (Aug. 2020), p. 105883. ISSN: 12709638. DOI: [10.1016/j.ast.2020.105883](https://doi.org/10.1016/j.ast.2020.105883).
- [64] Tamas Bykerk, Dries Verstraete, and Johan Steelant. “Low speed lateral-directional dynamic stability analysis of a hypersonic waverider using unsteady Reynolds averaged Navier Stokes forced oscillation simulations”. In: *Aerospace Science and Technology* 106 (Nov. 2020), p. 106228. ISSN: 12709638. DOI: [10.1016/j.ast.2020.106228](https://doi.org/10.1016/j.ast.2020.106228).
- [65] Wen Liu et al. “Parametric Study on Lateral–Directional Stability of Hypersonic Waverider”. In: *AIAA Journal* (June 2021), pp. 1–18. ISSN: 0001-1452. DOI: [10.2514/1.J059904](https://doi.org/10.2514/1.J059904).
- [66] Christopher Tarpley and Mark J. Lewis. “Stability derivatives for a hypersonic caret-wing waverider”. In: *Journal of Aircraft* 32.4 (July 1995), pp. 795–803. ISSN: 0021-8669. DOI: [10.2514/3.46793](https://doi.org/10.2514/3.46793).
- [67] Nicole Viola et al. “Aerodynamic Characterization of Hypersonic Transportation Systems and Its Impact on Mission Analysis”. In: *Energies* 14.12 (June 2021), p. 3580. ISSN: 1996-1073. DOI: [10.3390/en14123580](https://doi.org/10.3390/en14123580).
- [68] Chris Bliamis, Constantinos Menelaou, and Kyros Yakinthos. “Implementation of various-fidelity methods for viscous effects modeling on the design of a waverider”. In: *Aerospace Science and Technology* 133 (Feb. 2023), p. 108141. ISSN: 12709638. DOI: [10.1016/j.ast.2023.108141](https://doi.org/10.1016/j.ast.2023.108141).
- [69] Alberto Simon Felix. “Adjoint-Based Shape Optimisation of Hypersonic Vehicles”. PhD thesis. Cranfield: Cranfield University, 2023.
- [70] Marc Famada Vizcaino. “Aerodynamic shape optimisation of hypersonic waveriders using CFD and adjoint-based method”. PhD thesis. Cranfield: Cranfield University, 2023.
- [71] Jesse R. Maxwell. “Efficient Design of Viscous Waveriders with CFD Verification and Off-Design Performance Analysis”. In: *53rd AIAA/SAE/ASEE Joint Propulsion Conference*. Reston, Virginia: American Institute of Aeronautics and Astronautics, July 2017. ISBN: 978-1-62410-511-1. DOI: [10.2514/6.2017-4879](https://doi.org/10.2514/6.2017-4879).
- [72] Feng Ding et al. “Comparison between novel waverider generated from flow past a pointed von Karman ogive and conventional cone-derived waverider”. In: *Proceedings of the Institution of Mechanical Engineers, Part G: Journal of Aerospace Engineering* 229.14 (Dec. 2015), pp. 2620–2633. ISSN: 0954-4100. DOI: [10.1177/0954410015581404](https://doi.org/10.1177/0954410015581404).
- [73] Feng Ding et al. “Boundary-layer viscous correction method for hypersonic forebody/inlet integration”. In: *Acta Astronautica* 189 (Dec. 2021), pp. 638–657. ISSN: 00945765. DOI: [10.1016/j.actaastro.2021.09.018](https://doi.org/10.1016/j.actaastro.2021.09.018).

- [74] David C Wilcox. *Turbulence Modeling for CFD*. Third. La Cañada Flintridge: DCW Industries, Nov. 2006, pp. 16–17.
- [75] Daniel J. Poole, Christian B. Allen, and Thomas Rendall. “Comparison of Local and Global Constrained Aerodynamic Shape Optimization”. In: *32nd AIAA Applied Aerodynamics Conference*. Reston, Virginia: American Institute of Aeronautics and Astronautics, June 2014. ISBN: 978-1-62410-288-2. DOI: [10.2514/6.2014-3223](https://doi.org/10.2514/6.2014-3223).
- [76] Daniel J. Poole, Christian B. Allen, and Thomas C. S. Rendall. “Metric-Based Mathematical Derivation of Efficient Airfoil Design Variables”. In: *AIAA Journal* 53.5 (May 2015), pp. 1349–1361. ISSN: 0001-1452. DOI: [10.2514/1.J053427](https://doi.org/10.2514/1.J053427).
- [77] Antony Jameson. “Aerodynamic design via control theory”. In: *Journal of Scientific Computing* 3.3 (Sept. 1988), pp. 233–260. ISSN: 0885-7474. DOI: [10.1007/BF01061285](https://doi.org/10.1007/BF01061285).
- [78] Naoto Morita, Takeshi Tsuchiya, and Hideyuki Taguchi. “MDO of Hypersonic Waverider with Trajectory-Aero-Structure Coupling”. In: *23rd AIAA International Space Planes and Hypersonic Systems and Technologies Conference*. Reston, Virginia: American Institute of Aeronautics and Astronautics, Mar. 2020. ISBN: 978-1-62410-600-2. DOI: [10.2514/6.2020-2402](https://doi.org/10.2514/6.2020-2402).
- [79] Wen Liu et al. “Design and Optimization Method for Hypersonic Quasi-Waverider”. In: *AIAA Journal* 58.5 (May 2020), pp. 2132–2146. ISSN: 0001-1452. DOI: [10.2514/1.J059087](https://doi.org/10.2514/1.J059087).
- [80] Patrick E. Rodi. “Waverider Vehicle Optimization with Volumetric Constraints for Sonic Boom”. In: *2018 AIAA Aerospace Sciences Meeting*. Reston, Virginia: American Institute of Aeronautics and Astronautics, Jan. 2018. ISBN: 978-1-62410-524-1. DOI: [10.2514/6.2018-0551](https://doi.org/10.2514/6.2018-0551).
- [81] Kevin G. Bowcutt. “Multidisciplinary Optimization of Airbreathing Hypersonic Vehicles”. In: *Journal of Propulsion and Power* 17.6 (Nov. 2001), pp. 1184–1190. ISSN: 0748-4658. DOI: [10.2514/2.5893](https://doi.org/10.2514/2.5893).
- [82] Siemens Digital Industries Software. *Simcenter STAR-CCM+ 2402 (19.02.009-R8)*. 2024.
- [83] John D Anderson. “CHAPTER 4 : Oblique Shock and Expansion Waves”. In: *Modern Compressible Flow : With Historical Perspective*. 3rd ed. New York: McGraw-Hill, July 2002. Chap. 4, pp. 136–137.
- [84] Geoffrey Ingram Taylor and J W MacColl. “The air pressure on a cone moving at high speeds”. In: *Proceedings of the Royal Society of London. Series A, Containing Papers of a Mathematical and Physical Character* 139.838 (Feb. 1933), pp. 278–297. ISSN: 0950-1207. DOI: [10.1098/rspa.1933.0017](https://doi.org/10.1098/rspa.1933.0017).
- [85] Jade Nassif. *Waverider Generator 2.0.1*. June 2024. URL: [https://github.com/jade5638/waverider\\_generator](https://github.com/jade5638/waverider_generator).
- [86] David Cowden and James Cook. *cadquery 2.4.0*. Jan. 2024. URL: <https://pypi.org/project/cadquery/>.
- [87] Claude-Louis Navier. “Sur les lois des mouvements des fluides, en ayant égard à l’adhésion des molécules”. In: *Annales de Chimie et de Physique* 19 (1821), pp. 244–266.
- [88] D G Fletcher. “Fundamentals of hypersonic flow-aerothermodynamics”. In: *Critical Technologies for Hypersonic Vehicle Development (Von Karman Inst. for Fluid Dynamics, Rhode-St-Genese, 2005)* (2004), pp. 1–3.

- [89] Peter G Cross and Michael R West. “Simulation of hypersonic flowfields using Star-CCM+”. In: *China Lake, CA, USA: Naval Air Warfare Center Weapons Division* (2019).
- [90] Roop N Gupta et al. *Calculations and curve fits of thermodynamic and transport properties for equilibrium air to 30000 K*. Tech. rep. 1991.
- [91] Meng-Sing Liou. “A Sequel to AUSM: AUSM+”. In: *Journal of Computational Physics* 129.2 (Dec. 1996), pp. 364–382. ISSN: 00219991. DOI: 10.1006/jcph.1996.0256.
- [92] P.L Roe. “Approximate Riemann solvers, parameter vectors, and difference schemes”. In: *Journal of Computational Physics* 43.2 (Oct. 1981), pp. 357–372. ISSN: 00219991. DOI: 10.1016/0021-9991(81)90128-5.
- [93] Hadi Vafadar Moradi and Mostafa Hosseinalipour. “On the Performance of AUSM Based Schemes in Hypersonic Flow with Equilibrium Gas Effects”. In: *14th AIAA/AHI Space Planes and Hypersonic Systems and Technologies Conference*. Reston, Virginia: American Institute of Aeronautics and Astronautics, Nov. 2006. ISBN: 978-1-62410-050-5. DOI: 10.2514/6.2006-7962.
- [94] J. A. Meijerink and H. A. van der Vorst. “An Iterative Solution Method for Linear Systems of Which the Coefficient Matrix is a Symmetric M-Matrix”. In: *Mathematics of Computation* 31.137 (Jan. 1977), p. 148. ISSN: 00255718. DOI: 10.2307/2005786.
- [95] V. VENKATAKRISHNAN. “On the accuracy of limiters and convergence to steady state solutions”. In: *31st Aerospace Sciences Meeting*. Reston, Virigina: American Institute of Aeronautics and Astronautics, Jan. 1993. DOI: 10.2514/6.1993-880.
- [96] Philip L Roe. “Some contributions to the modelling of discontinuous flows”. In: *Large-scale computations in fluid mechanics* (1985), pp. 163–193.
- [97] Rony Keppens et al. *MPI-AMRVAC 3.1 - Slope Limiters*. Nov. 2022. URL: [https://amrvac.org/md\\_doc\\_limiter.html](https://amrvac.org/md_doc_limiter.html).
- [98] Tom-Robin Teschner. *CFD Toolbox (Chrome Extension)*. Cranfield, 2023.
- [99] ScienceDirect. *Schlieren Method*. URL: <https://www.sciencedirect.com/topics/engineering/schlieren-method#:~:text=Schlieren%20are%20refractive%20index%20or,first%20derivative%20of%20the%20density..>
- [100] P Saves et al. “SMT 2.0: A Surrogate Modeling Toolbox with a focus on Hierarchical and Mixed Variables Gaussian Processes”. In: *Advances in Engineering Software* 188 (2024), p. 103571. DOI: <https://doi.org/10.1016/j.advengsoft.2023.103571>.
- [101] M. D. McKay, R. J. Beckman, and W. J. Conover. “A Comparison of Three Methods for Selecting Values of Input Variables in the Analysis of Output from a Computer Code”. In: *Technometrics* 21.2 (May 1979), p. 239. ISSN: 00401706. DOI: 10.2307/1268522.
- [102] Chun-Qing Li and Wei Yang. “Essential reliability methods”. In: *Time-Dependent Reliability Theory and Its Applications*. Elsevier, 2023, pp. 51–119. DOI: 10.1016/B978-0-323-85882-3.00006-4.
- [103] Fabian Pedregosa et al. “Scikit-learn: Machine Learning in Python”. In: *Journal of Machine Learning Research* 12.85 (2011), pp. 2825–2830. URL: <http://jmlr.org/papers/v12/pedregosa11a.html>.
- [104] Thomas J. Santner, Brian J. Williams, and William I. Notz. *The Design and Analysis of Computer Experiments*. New York, NY: Springer New York, 2018. ISBN: 978-1-4939-8845-7. DOI: 10.1007/978-1-4939-8847-1.

- [105] B. Gaspar, A.P. Teixeira, and C. Guedes Soares. “Adaptive surrogate model with active refinement combining Kriging and a trust region method”. In: *Reliability Engineering & System Safety* 165 (Sept. 2017), pp. 277–291. ISSN: 09518320. DOI: [10.1016/j.ress.2017.03.035](https://doi.org/10.1016/j.ress.2017.03.035).
- [106] Zhihui Li and Xinqian Zheng. “Review of design optimization methods for turbomachinery aerodynamics”. In: *Progress in Aerospace Sciences* 93 (Aug. 2017), pp. 1–23. ISSN: 03760421. DOI: [10.1016/j.paerosci.2017.05.003](https://doi.org/10.1016/j.paerosci.2017.05.003).
- [107] John H Holland. *Adaptation in natural and artificial systems: an introductory analysis with applications to biology, control, and artificial intelligence*. MIT press, 1992.
- [108] Ahmed Fawzy Gad. “Pygad: An intuitive genetic algorithm python library”. In: *Multimedia Tools and Applications* (2023), pp. 1–14. DOI: <https://doi.org/10.48550/arXiv.2106.06158>.
- [109] K. Deb et al. “A fast and elitist multiobjective genetic algorithm: NSGA-II”. In: *IEEE Transactions on Evolutionary Computation* 6.2 (Apr. 2002), pp. 182–197. ISSN: 1089778X. DOI: [10.1109/4235.996017](https://doi.org/10.1109/4235.996017).
- [110] Xin-She Yang. “Multi-Objective Optimization”. In: *Nature-Inspired Optimization Algorithms*. Elsevier, 2014. Chap. 14, pp. 197–211. DOI: [10.1016/B978-0-12-416743-8.00014-2](https://doi.org/10.1016/B978-0-12-416743-8.00014-2).
- [111] Leo Breiman. “Random Forests”. In: *Machine Learning* 45.1 (2001), pp. 5–32. ISSN: 08856125. DOI: [10.1023/A:1010933404324](https://doi.org/10.1023/A:1010933404324).
- [112] Chuanzhen Liu et al. “Experimental Investigation on Off-Design Performances of Double-Swept Waverider”. In: *AIAA Journal* 61.4 (Apr. 2023), pp. 1596–1607. ISSN: 0001-1452. DOI: [10.2514/1.J062254](https://doi.org/10.2514/1.J062254).
- [113] Noubel Hugo and Viviana Lago. “Experimental Analysis of Waverider Lift-to-Drag Ratio Measurements in Rarefied and Supersonic Regime”. In: *Hypersonic Vehicles*. Ed. by Giuseppe Pezzella and Antonio Viviani. Rijeka: IntechOpen, 2021. Chap. 3. DOI: [10.5772/intechopen.100328](https://doi.org/10.5772/intechopen.100328). URL: <https://doi.org/10.5772/intechopen.100328>.
- [114] John D Anderson. “HISTORICAL NOTE : THE ILLUSIVE CENTER OF PREDICTION”. In: *Fundamentals of Aerodynamics*. 6th ed. McGraw-Hill Education, Aug. 2016, pp. 89–93.
- [115] Michael V Cook. “Static Equilibrium and Trim”. In: *Flight Dynamics Principles : A Linear Systems Approach to Aircraft Stability and Control*. 3rd ed. Butterworth-Heinemann, 2013. Chap. 3, pp. 33–34. ISBN: 9780080982427. DOI: [10.1016/C2010-0-65889-5](https://doi.org/10.1016/C2010-0-65889-5).
- [116] Cornell University. *Chapter 3: Static Longitudinal Stability and Control*. URL: <https://courses.cit.cornell.edu/mae5070/StaticLongitudinal.pdf>.